Higher-Order-Mode-based Beam Phase and Beam Position Measurements in Superconducting Accelerating Cavities at the European XFEL

A thesis submitted to The University of Manchester for the degree of

Doctor of Philosophy

in the Faculty of Science and Engineering

2017

Liangliang Shi

School of Physics and Astronomy

Content

Total word count: *34890*

List of Figures

List of Tables

Abstract

Instrumentation of higher order modes (HOMs) excited in accelerating cavities for beam phase and position inference provides a noninvasive and economical beam diagnostic. The principles and techniques for this purpose are investigated for TESLA (TeV Energy Superconducting Linear Accelerator) cavities at the injector part of the newly built European XFEL and at FLASH, two free electron laser facilities based on the TESLA technology.

I have designed and instrumented unconventional beam phase monitors based on monopole modes in TESLA cavities and demonstrated a routine resolution of 0.1° with a broadband setup. The best resolution achieved with this system is 0.03°. The resolution is largely limited by the signal power. In order to aid the monitor design and study its performance, I have employed a coupled circuit model which indicates that the resolution can be further improved by optimizing the SNR (signal to noise ratio) and sampling frequency. This is the first type of monitor that is able to probe online the beam phase directly w.r.t. the accelerating field in individual accelerating cavities. The system can be used for long term RF drifts monitoring and also be used to decouple the phase jitter and drift sources in the injector part of a linac. Therefore the system can provide valuable information for the low level RF system.

Beam position monitoring based on dipole modes in TESLA cavities at FLASH was demonstrated for the first time to work stably over several months with below 5 μm resolution. The improvement is attributed to a focused campaign on various signal and analysis techniques. These techniques can be transferred with little effort to the similar system, now under design for the European XFEL. As a preparation for the beam position monitor for the third harmonic cavities at the E-XFEL, I have measured and characterized the HOM spectra for single and coupled cavities. In particular there existed no such measurements for eight coupled cavities. These measurements pave the way for the instrumentation of 3.9 GHz cavities and show that the modes are well damped to the required limit.

Declaration

No portion of the work referred to in this thesis has been submitted in support of an application for another degree or qualification of this or any other university or other institute of learning.

Liangliang Shi

School of Physics and Astronomy

The University of Manchester

Oxford Road

Manchester M13 9PL

United Kingdom

March 2017

Copyright

[1] This excludes material already printed in academic journals, for which the copyright belongs to said journal and publisher.

The Author

The author started the journey of physics in Lund University, Sweden in 2010 with a major in optics and experimental particle physics, which ended up with a Master of Science degree. During the master project, the author was involved in the development of a readout system for gaseous detector TPC (Time Projection Chamber) for the International Linear Collider project. In 2012, the author had a chance to visit DESY to test the data acquisition system with electron beams under the AIDA collaboration. After the master study, the author joined the accelerator group at the University of Manchester in 2013 to embark on a PhD degree under the EuCARD^2 collaboration. At the same time, the author joined the MDI (Machine Diagnostic and Instrumentation) group at DESY in Hamburg, Germany.

Acknowledgements

Firstly, I would like to thank my supervisors, Prof. Roger M. Jones and Dr. Nicoleta Baboi, for their continuous support and skilful guidance in the field of accelerator physics, for their patience, motivation throughout my research and writing of this thesis. I deeply appreciate the help of Dr. Nicoleta Baboi for her comprehensive and helpful tips in almost every respect when I moved to Hamburg. Without my supervisors' excellent tutorship, I would by no means have grasped the accelerator physics to such a degree and bring the project to the current stage. I could not have imagined having a better advisor and mentor for my study.

Besides my advisors, I thank all excellent colleagues I met during my stay at DESY, especially Bastian Lorbeer, Dirk Lipka, Christian Schmidt, Thomas Wamsat, Alexey Sulimov, Paolo Pierini etc. I also thank Kay Wittenburg, Dirk Noelle and Elmar Vogel for their support and coordination in many respects for my measurements. I thank Alexandr Ignatenko for many tips of how to live better in Hamburg. I learned a lot from the MEW (Manchester Electrodynamics and Wakefields) weekly group meeting where new stimulating ideas always interweave with each other and spark off new ideas. I particularly thank Aaron Farricker and Nirav Joshi for their proofreading of my thesis. I also extend my thanks to collaborators within the WP12 under EuCARD^2. These include Nathan Eddy from Fermilab, Thomas Flisgen from University of Rostock and Samer Bou Habib from Warsaw University of Technology.

I acknowledge my financial support from DESY, the European XFEL, EuCARD^2, The University of Manchester and Cockcroft Institute. During my PhD study, I received support for two accelerator schools (JAS13 and Eighth International Accelerator School for Linear Colliders), three workshops (ICFA Mini Workshop on Higher Order Modes in Superconducting Cavities 2014 and 2016, 5th Topical Workshop on Beam Diagnostics), and two international conferences (IBIC14 and IPAC16). My research

benefits a lot from these. I also got acquainted with many amazing people at these events. Without this precious and immeasurable support it would not have been possible to conduct this research. I thank PIER graduate school for various social and career events held at DESY.

Finally, I would like to express my thanks to my family. My father ignited my interests in nature and instilled basic knowledge of math and physics when I was a kid, while my mother always taught me to be an upright man. Both of them make me live in a warm family. Much joy was added during my childhood because of my lovely younger sister. Last but not least, my life entered a new chapter with the birth of my daughter, Emily, the most precious gift for me ever. With my wife and her company, I felt not alone during the long and dark nights to complete my thesis writing. No words can describe my gratitude for my wife, Hong, for her love, company and spiritual support.

Chapter 1 - Introduction

FEL (Free Electron Laser) facilities are gaining popularity worldwide and this is driven by various disciplines and industrial applications over the decades. These unconventional lasers can provide unique ultra-short light pulses with high intensity, high spatial and temporal coherence, and spectral purity, which are required by various experiments. FLASH [1] (Free Electron Laser in Hamburg) and the E-XFEL [2] (European X-Ray Free Electron Laser) are examples of such facilities that are able to produce soft and hard X-ray beams respectively. These photon beams are generated by ultra-relativistic[2] electron beams accelerated by a linear accelerator, also known as linac. In order to generate high-quality photon beams, stringent requirements on the quality of the electron beams are imposed. Therefore, beam diagnostics systems are indispensable. Beam diagnostics and instrumentation itself is a wide and quite interdisciplinary field.

The objective of this thesis is to investigate novel types of beam phase and position monitoring based on electron beam excited higher order modes in SRF (Superconducting Radio Frequency) accelerating cavities at the E-XFEL. These monitors are distinguished from conventional monitors with the same functionalities in that the latter are normally based on specially designed beam 'pickup' (electrode or cavity etc.) components. The main motivation of the project is to develop high-performance monitors using existing accelerating cavities of the linac. In this sense, the functionalities of accelerating cavities are two-fold: 1. beam acceleration; 2. beam diagnostics based on the higher order modes excited in the same cavities. Therefore the beam diagnostics techniques investigated here are non-invasive to the beam. It should be pointed out that along the linac there are also places where there is no space for conventional diagnostics components and the monitors developed here find their application thereof.

[2] The velocity is very close to the speed of light c.

When a bunch of electrons traverses a cavity, it excites an electromagnetic field called wakefield. This can seriously degrade the electron beam quality if left unchecked [3] and can cause BBU (Beam Breakup) [4] in the worst case. The wakefield can be decomposed into a multipole expansion of modes. Only those with a significant impact on the beam are of interests, and hence a relatively small number of modes can be used to characterize the beam. The modes with higher resonant frequencies than the mode that is used for acceleration are generally referred to as HOMs (Higher Order Modes). In order to avoid their damaging effects, these HOMs generally have to be damped or detuned [3]. On the other hand, the damped HOMs can be used to infer the status of electron beam. The main content of the thesis deals with investigation and development of beam diagnostic tools based on these damped HOMs from SRF accelerating cavities for the E-XFEL.

One main part of this thesis is on beam phase monitoring which is of vital importance for FEL facilities. Generally speaking, in order to make the electron beam participate in the FEL process efficiently, high quality electron beam is required. The beam quality is largely determined by the RF system and beam optics. Therefore exquisite manipulation of the RF field inside cavities is required. For example, both FLASH and the E-XFEL require a stability in the amplitude and phase of RF field within 0.01% and 0.01° respectively [2].

Klystrons are used to provide power to the cavities in ten MWs range. At FLASH, one klystron feeds 16 SRF cavities while the number is increased to 32 at the E-XFEL. The accelerating RF field needs to be precisely controlled in terms of amplitude and phase as mentioned. Standard diagnostic techniques ascertain the beam phase relative to the RF field by inference in a transient excitation of the electron beam. This thesis focuses on determining the phase based on beam-induced HOMs or HOMBPhM (Higher Order Modes based Beam Phase Monitor) in short. The monitor, for the first time, enables us to make an online direct measurement of the beam phase w.r.t. the accelerating RF field. Extensive studies have been carried out to investigate the principle and optimize the performance. Measurements with a

broadband setup at FLASH and the E-XFEL are complemented by simulations. Various effects on the final monitor resolution have been quantified.

Another part of this thesis is concerned with monitoring the beam position based on HOMs in SRF accelerating cavities, or HOMBPM (Higher Order Modes based Beam Position Monitor). A large number of conventional BPMs (Beam Position Monitors) are installed to monitor and control the beam orbit along the accelerator so that its performance is optimized. These monitors are based on different techniques but all of them rely on the coupling between the electron beam and specially designed 'pickups' [5]. The HOMBPMs can be used to monitor the beam position inside each accelerating cavity where other types of BPMs cannot provide directly.

HOMBPMs have been developed for both 1.3 and 3.9 GHz cavities at FLASH in the past [6], [7]. Since the SRF cavities and HOM couplers have already been developed, these monitors only require associated electronics and algorithms to infer the beam position. In this sense, they are economical. However, HOMBPMs at FLASH can only work for a short time after calibration. This issue has triggered a study on the stability of the system. Efforts were made to understand both the physics and technical issues. I also focused on the development of HOMBPMs for the E-XFEL. The electronics designed for 1.3 GHz cavities are based on a direct sampling technique [8] and this is in contrast with the classical down-conversion scheme based on a local oscillator. The HOMBPM and HOMBPhM are integrated in the same electronics in order to make the system compact and economical at the E-XFEL.

The HOMBPMs for the 3.9 GHz cavities employ a band of modes, in contrary to a single mode for the 1.3 GHz cavities. This is due to the difficulty in filtering a single mode as it will be shown in Chapter 4. When several cavities are coupled together, the dipole spectra get more complicated. For the E-XFEL, eight 3.9 GHz cavities are coupled together in a cryomodule as compared to four at FLASH.

Therefore, extensive measurements and simulations [9] of the HOM spectra have been carried out for both single and coupled cavities.

Independent of the instability issues mentioned above, the HOMBPM system can be used as a power meter to align the electron beam inside the cavities in order to minimise the transverse momentum kicks to the beam caused by wakefields. By identifying the beam position inside each cavity with minimal dipole power, the relative cavity misalignments inside a module can also be deduced. These functionalities add extra value to the HOMBPM system.

In the following sections of this chapter, I first briefly outline the components of a linac-based FEL facility. The E-XFEL and FLASH, where my experiments were carried out, are introduced. In the last section, an overview of HOM-based beam diagnostic systems is presented.

1.1. Linac-based SASE Free Electron Lasers

In a linac-based FEL, electron beams travel in a straight line along the accelerating structures. Compared with the circular accelerators, they do not suffer from energy loss due to synchrotron radiation, and the longitudinal emittance is thus not limited by the radiation process. This fact is essential for the lasing process [10]. The driving force behind the development of light sources is the optimisation of their brilliance (or spectral brightness), a figure of merit for many experiments. For a linac-based FEL, the brilliance is many orders of magnitudes higher than for synchrotron radiation sources.

A linac-based FEL facility generally consists of three main parts (see Figure 1.1): a particle source which provides free electrons, a linac which accelerates the electrons by converting energy from a klystron into electron beam energy, and an undulator section which transfers the energy from the energetic electrons to photons beams. It is very difficult to directly obtain from the source the high electron beam peak

current (kA) required for the FEL process therefore bunch compression schemes are implemented.

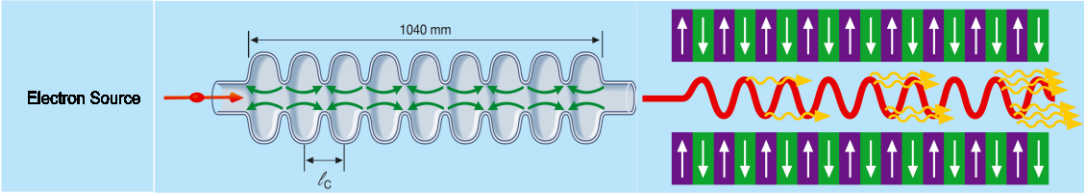

Figure 1.1 Main components of a linac-based FEL: the electron source, accelerating structures, and undulators. (Courtesy of DESY)

- **Electron source** – It provides free electrons that are to be accelerated in the linac. The electrons are normally obtained through the photoelectric effect. Laser pulses are illuminated onto a piece of metal and electrons are emitted. The pulses arrive in a periodic manner so that electron bunches are emitted periodically.
- **Accelerating structures** – They accelerate the electrons and occupy the main part of a linac to provide acceleration of electrons. They are usually fed with RF power by klystrons. The RF technology is widely used for acceleration due to its maturity during 1940s [11]. The RF cavities are either normal conducting or superconducting. Superconducting cavities have the advantage that they have low wall losses and therefore provide higher energy efficiency, at the expenses of high cost and complicated cryogenic system.
- **Undulator** – After exiting the accelerating section, the electrons are steered into an array of permanent magnets called undulators, with alternating poles with fixed period. The electrons propagate along a sinusoidal path and radiate in a narrow cone in the forward direction. The radiated wavelength is governed by the following equation [12]:

$$\lambda = \frac{\lambda_u}{2\gamma^2}\left(1 + \frac{K^2}{2}\right), \text{with } \gamma = \frac{E}{m_e c^2} \text{ and } K = \frac{eB_u\lambda_u}{2\pi m_e c}, \quad 1.1$$

where λ is the emitted photon wavelength, λ_u the period of the permanent magnets, γ the Lorentz factor, K the undulator parameter, E the energy of the electrons, m_e the rest mass of an electron, c the speed of light in vacuum and B_u the peak magnetic field on the undulator axis.

The powerful X-rays are generated in a SASE (Self-Amplified Spontaneous Emission) process. The initially emitted photons travel slightly faster than the electrons in the undulator. A resonant condition is met when the photon is ahead of the electrons by a wavelength λ after one undulator period λ_u. Depending on the phase between the electrons and the emitted radiation field, some of electrons are accelerated and others decelerated. The net effect is that the electron bunch starts to form mirco-bunches. Within each micro-bunch, all the electrons radiate coherently and the output power is proportional to the square of the number of electrons. The details of the process can be found in [12].

From equation 1.1, it is clear that one can vary the photon wavelength by changing the energy of electrons that enter the undulator. This property is generally referred to as tunability. The fact also indicates that any energy spread in the electron beam causes the X-ray impurity. Therefore there is an additional accelerating section at both FLASH and the E-XFEL to minimize the energy spread.

Besides the backbone components mentioned above, other components are required in order to achieve the desired figures of merit mentioned at the beginning. These components include, but are not limited to, magnets for beam focusing, steering and compressing, instrumentation for beam diagnostics etc.

1.2. The E-XFEL and FLASH

The E-XFEL and FLASH are linac-based FEL facilities that are able to deliver high quality X-ray beams for photon experiments. These X-rays benefit a wide range of researches spanning physics, chemistry, material science, biology, and nanotechnology.

The backbone structure of each facility follows what I have described in section 1.1, namely electron source, accelerating structures, and undulators. Both the E-XFEL and FLASH are based on the niobium TESLA cavities [13], working at 1.3 GHz to provide acceleration to the electron beam. These cavities will be detailed in Chapter 2.

1.2.1. The European XFEL (E-XFEL)

The E-XFEL starting from DESY campus is hosted in the north-west of Hamburg and Schenefeld. It is a SASE-FEL facility, which achieves laser amplification and saturation within a single passage of the electron bunches through long undulator sections.

The facility aims at generating extremely brilliant, ultra-short pulses with spatial coherence, within the hard X-ray range. The wavelength of X-rays in this range has the potential to explore tiny structures at atomic scales e.g. the structure of important molecules [2]. The high photon intensity can be used to create extreme conditions e.g. intense X-ray flashes can be used to create extreme pressures and temperatures. The ultra-short pulses enable researchers to record various processes that happen on a femtosecond time scale. For example, the film of how a molecule forms and separates can deepen our understanding of the catalysis, which can lead to optimization of production mechanisms and new products. In the field of biology, flashes of X-rays allow researcher to investigate the 3D structure of biomolecules, cell constituents and viruses.

In order to generate X-ray beams with the figures of merit required by various experiments, four operating points in the electron energy are fixed: 17.5 GeV, 14 GeV, 12 GeV, and 8.5 GeV [14]. The bunch charge varies from 20 pC to 1 nC. The peak current required is approximately 5 kA and the normalized RMS emittance is between 0.3 and 1 mm·mrad depending on the bunch charge [14]. Some of the main parameters of electron and photon beams are summarized in Table 1-1.

Table 1-1 Electron and photon beam parameters at the E-XFEL [15]

Electron Beam		**Photon Beam**	
Energy (GeV)	17.5, 14, 12, 8.5	Wavelength (nm)	> 0.1
Bunch charge (nC)	0.02-1	Average single pulse energy (μJ)	10-500
Bunches / train	1-2700	FWHM pulse duration (fs)	100
Bunch spacing (μs)	0.2 (4.5 MHz)	Peak power (GW)	> 20
Repetition rate (Hz)	10	Peak brilliance [Photons/(s·mrad^2·mm^2·0.1%BW)]	5×10^{33}
Energy spread (MeV)	< 1		

The schematic layout of the E-XFEL is shown in Figure 1.2.

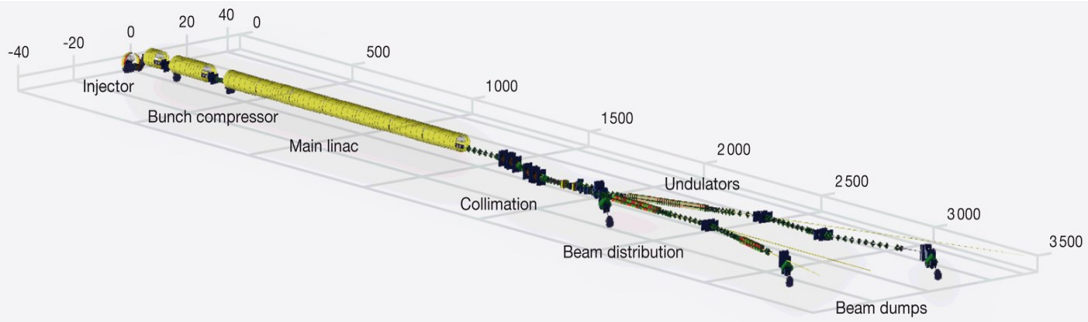

Figure 1.2 Layout of the E-XFEL (not to scale). The injector, the main linac, and undulators are shown. Three bunch compressors are installed. After the main linac, the electron beam is distributed to three undulator sections and then three dumps. Diagnostics components are not shown. The length of the main linac and the full facility is approximately 1.7 and 3.4 kilometres respectively. (Courtesy of the E-XFEL)

The injector which started commissioning in December 2015 hosts, in addition to the photoelectric gun, one standard superconducting 1.3 GHz module, one

superconducting 3.9 GHz module [16], each with eight cavities, and a diagnostic section. The 3.9 GHz module is used to linearize the energy chirp induced by the first accelerating module in the longitudinal phase space [17]. The whole injector is 45 meters long.

The linac contains 96 cryomodules with eight TESLA 1.3 GHz cavities inside. Each cavity is designed to provide accelerating gradients above 23.6 MV/m. Three-hundred-meter long variable gap undulator sections are connected to the end of the main linac, where X-rays are produced by the SASE process.

The E-XFEL operates in the pulsed mode with 10 Hz repetition rate of 0.6 milliseconds pulse duration. Each pulse contains up to 2700 electron bunches. In order to achieve the wavelength of hard X-rays, the required energy of electrons is approximately 17.5 GeV.

1.2.2. FLASH

FLASH, the world's first soft X-ray FEL, was originally a test facility for the TESLA linear collider project [18] for which the TESLA technology was developed. It produces soft X-rays and delivers beam to the photon science user community since 2005[3]. The facility has two undulator beamlines [1] and provides two experimental halls each with up to six photon beamlines for different experiments. In addition, FLASH serves as a pilot facility for the E-XFEL project, a test bed for the research on linear collider related superconducting accelerator technology and novel plasma acceleration. Many scientific disciplines benefit from this powerful soft X-ray source.

The schematic layout of FLASH is shown in Figure 1.3. The first undulator beam line, FLASH1, started operation in 2004, and succeeded in the first lasing in the SASE mode at a wavelength of 32 nm. A second beam line, FLASH2, achieved the first lasing in August 2014.

[3] In February 2000, the first lasing was observed at 109 nm and the facility was called TTF1 then.

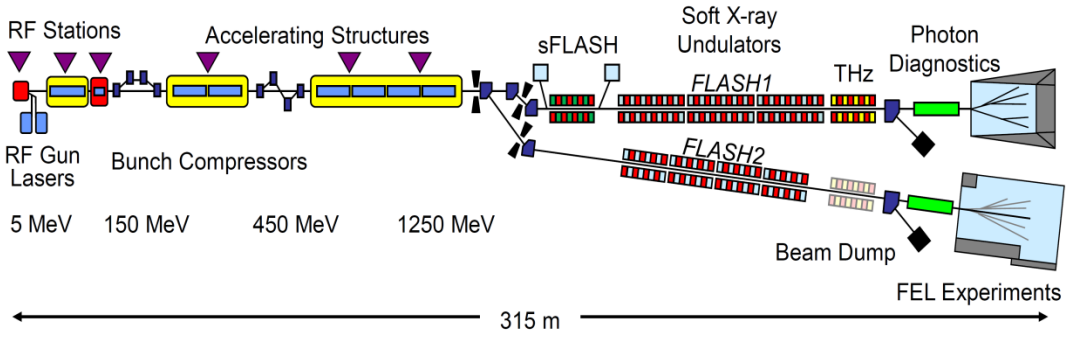

Figure 1.3 Layout of FLASH (not to scale) with FLASH1 and FLASH2 undulator beamlines. Magnets, diagnostic and other components are not shown. (Courtesy of DESY)

The electron bunches are produced in a laser driven photon gun. There are seven accelerating modules, each of them consisting of eight TESLA cavities working at 1.3 GHz. There is also one 3.9 GHz module with four cavities to linearize the energy chirp that is induced by the first accelerating module in the longitudinal phase space [19]. The injector is capable of producing up 800 bunches per pulse. The pulse repetition rate is 10 Hz. Two stages of bunch compressing are used at electron energies around 150 and 450 MeV respectively in order to achieve the peak currents of a few kA required by the SASE process. The energy of the electrons can be varied from 350 MeV to 1.25 GeV. The photon radiation is produced in a 27-m-long undulator with fixed gap and 30-m-long undulator with variable gap at FLASH1 and FLASH2 respectively. The typical charge of a bunch is between 0.08 nC and 1 nC [1]. The main parameters of FLASH are summarized in Table 1-2.

Both the E-XFEL and FLASH are based on the TESLA cavities for electron beam acceleration. As we will see later, when the electron beam is being accelerated, it also excites higher order modes. These modes are harmful to the beam quality therefore they need to be damped. These higher order modes can also be used for beam diagnostic.

Table 1-2 Electron and photon beam parameters at FLASH [20]

Electron Beam		Photon Beam	
Energy (MeV)	350-1250	Wavelength (nm)	4-90
Bunch charge (nC)	0.02-1.2	Average single pulse energy (μJ)	1-600
Bunches / train	1-800	FWHM pulse duration (fs)	< 30-200
Bunch spacing (μs)	1-25	Peak Power (GW)	1-5
Repetition rate (Hz)	10	Peak Brilliance [Photons/(s·mrad^2·mm^2·0.1%BW)]	10^{28}-10^{31}
Energy spread (MeV)	< 1		

1.3. HOM-based Beam Diagnostics for the E-XFEL and FLASH

Higher order modes are generally unwanted from beam dynamics point of view since they dilute the beam quality. They are therefore damped by the specially designed HOM couplers. These modes are therefore available at the HOM coupler ports and transmitted via RF cables from the tunnel to diagnostic racks. These signals serve as the basis for the beam diagnostic system I report in this thesis.

As it will be discussed in Chapter 5, based on the higher order monopoles in SRF cavities, I investigated a monitor which can deliver the beam phase relative to the accelerating mode. The proof-of-principle measurements were mentioned in [6]. This monitor is, for the first time, able to measure the beam phase relative to the RF field directly and for each electron bunch. The monitors are currently being developed for 1.3 GHz cavities. Measurements have been carried out both at FLASH and the E-XFEL.

Based on dipole modes, HOMBPMs have been developed in the past for both 1.3 and 3.9 GHz cavities at FLASH. For these monitors, the calibration issues are mainly investigated as it will be discussed in Chapter 6. HOM electronics for the E-XFEL 1.3 GHz cavities are currently being developed in collaboration with the Warsaw University of Technology (WUT). HOMBPM and HOMBPhM are

integrated in the same electronics [8]. The electronics is based on a technique called direct sampling.

The HOMBPM electronics for the 3.9 GHz cavities is under development for the E-XFEL [21]. Compared with the 1.3 GHz cavity case, these monitors are more complicated in terms of dipole spectra used for beam position extraction. The complication is due to the fact that for 3.9 GHz cavities most of the dipole modes are above the cut-off of the beam pipe and therefore the cavities are coupled with each other. The coupling of cavities makes the dipole spectra dense. In addition, at the E-XFEL there are eight cavities as compared to four at FLASH. Therefore extensive measurements of the HOM spectra have been carried out in the E-XFEL 3.9 GHz cavities. The HOMBPM system will use a band of dipole spectra for beam position extraction similar to the system at FLASH [7].

In order to process the RF signal from HOM couplers, normally three schemes of signal processing are used: 1. Down convert the RF signal into an IF (Intermediate Frequency) signal and then sample it with an ADC (Analog to Digital Converter). The samples can be processed for example with matured DSP (Digital Signal Processor) techniques. 2. The RF signal is sampled directly with a fast ADC. The samples are then processed with a processor. 3. Up convert the RF signal to the optical range so that all the processing can be performed with matured optical techniques. The HOM-based beam phase and position monitors developed for FLASH and the E-XFEL are based on schemes 1 and 2.

In summary, the main advantage of the accelerating cavity based beam monitors is the low costs. These monitors find their applications when there is a constraint of space for other beam monitors as it is the case inside the cryomodules. Also, the HOMBPM can be used for beam alignment in order to minimise the transverse momentum kick due to wakefields. The relative misalignment of cavities inside a cryomodule can also be deduced based on instrumented dipole modes [22]. Last but not least, the beam diagnostics presented here is non-invasive to the beam. These monitors will be valuable tools for beam diagnostics both at FLASH and the

E-XFEL. My contributions mainly lie in three parts: 1. the beam phase measurements for 1.3 GHz cavities. With the experimental setup and simulation tools developed by me, the performance of such a monitor is investigated. 2. The beam position measurements for the 1.3 GHz cavities. For the first time, I proved that such a system can be used as beam position monitors with μm resolution over several months period at FLASH. A set of beam position prediction algorithms developed can be used to the similar system at the E-XFEL. 3. The beam position measurements at the 3.9 GHz cavities. This portion of work is mainly focused on the measurements and characterization of the HOM spectra of each single cavity and the string of eight coupled cavities. Previously no measurements existed for eight coupled cavities and no simulations had been performed for a string of eight cavities because of the complexity of the structure.

The thesis is organized in the following way:

In chapter **two**, the figures of merit for an RF cavity and the concept of superconductivity are introduced first. The concepts of wakefields and impedance are presented there. These provide the theoretical basis for the HOM-based beam monitors. The working principle of these monitors will then become clear.

In chapter **three**, a single chain circuit model focused on one band of higher order modes is introduced. It is developed to simulate the beam-excited HOMs for 1.3 GHz SRF cavities and to facilitate the development of the HOM-based beam phase monitors.

In chapter **four**, the measurements and characterization of spectra for both 1.3 and 3.9 GHz cavities are shown for the E-XFEL and FLASH. The spectra measured are essential to gain insight into the HOM behaviour in single and coupled cavities.

In chapter **five**, the HOM-based beam phase monitor is described based on both simulations and experiments. Measurements were made with a broadband setup and the results are compared with simulations.

In chapter **six**, the HOM-based beam position monitors are described. The focus here is curing drifts in the calibration over time. The influence of the beam trajectory angle with respect to the cavity axis is investigated as well.

Chapter **seven** summarizes the thesis. Future prospects for these novel HOM-based monitors development are also discussed.

Chapter 2 - Wakefields and Impedances in SRF Cavities

Most of the linac of an FEL facility is occupied by accelerating cavities. These provide energy to the electron beam through RF fields. In this chapter the SRF accelerating technology used for acceleration at FLASH and the E-XFEL will be introduced, as well as the main figures of merit used to characterize these cavities. These figures of merit are equally applicable to NC (Normal Conducting) accelerating structures. TESLA and the third harmonic cavities, which are used by both FLASH and the E-XFEL, will be used to illustrate the discussion in section 2.1. These cavities form a large part of the hardware that are used for beam phase and position measurements as it will be detailed in Chapters 5 and 6 respectively. In section 2.2, the concepts of wakefield, HOM, wake potential, and impedance are introduced.

2.1. Superconducting Radio Frequency Cavities

In the context of accelerator physics or RF engineering, a cavity is a hollow space bounded with metal. The geometry and size of a cavity determines the field profiles and frequencies of the resonances that can be excited. Cavities with metal walls made of superconducting material are referred to as superconducting cavities.

2.1.1. Superconductivity

The discovery of superconductivity in 1911 by H. Onnes [23] led to the development of its technological use in many fields, including particle accelerators. Superconductors are used mainly for accelerating cavities and magnets with the goal to reduce the power consumption. For an accelerating cavity, the maximum accelerating gradient is limited by the critical magnetic field. Taking the niobium TESLA cavity as an example, the critical magnetic field is approximately 200-240 mT [13] and this implies a maximum accelerating gradient of approximately 50-60 MV/m [13], [24]. However, the typical accelerating gradient for TESLA cavities in operation is significantly lower as it is ~25 MV/m. High gradient, no more than 50 MV/m, has been achieved for single cell re-entrant and

low loss cavities [25], [26]. The maximum gradient achieved for a nine cell cavity (for International Linear Collider) is approximately 40 MV/m [27].

In contrast to the DC case, losses are caused by the RF field, which can penetrate into the surface layer of the superconductor and induce oscillations of the electrons that are not bounded to the Cooper pairs [24]. The number of these unpaired electrons depends on the temperature. Therefore, in order to minimize it, extremely low temperatures - in the vicinity of the absolute zero temperature - are required. The surface resistance, $R_s(T,\omega) = R_{BCS}(T,\omega) + R_i$, does not vanish at $T = 0\ K$, but has a temperature-independent residual resistance R_i. The temperature-dependent part, $R_{BCS}(T)$, can be written as [24]:

$$R_{BCS}(T,\omega) \propto \frac{\omega^2}{T} e^{\left(-\frac{1.76T_c}{T}\right)}, \qquad 2.1$$

where T_c is the critical temperature of the superconductor and ω is the angular frequency. For cavities made of niobium, R_s is in the range of tens of nΩ at 2 K for a 1.3 GHz field.

There is also another contribution to the surface resistance, which is due to the trapped DC magnetic field resulting from insufficient shielding of external DC magnetic field [28]. At 1.3 GHz the surface resistance amounts to 3.5 nΩ/μT for niobium. Taking the magnetic field at the earth surface into account, the surface resistance is up to several tens of nΩ, therefore the quality factor, as it will be discussed in section 2.1.3, drops by one order of magnitude. Consequently, a better cavity performance can be obtained by shielding the cavity from external magnetic fields [13].

2.1.2. Electromagnetic modes in a cavity

The electromagnetic field can be expanded in terms of modes in an enclosed cavity by Condon method [29]. Each mode has a distinct frequency (in the case of

non-degeneracy) and a field distribution. For a cylindrically symmetric cavity, the time-harmonic electric and magnetic fields $\boldsymbol{E}$ and $\boldsymbol{B}$ can be written in cylindrical coordinates (r, θ, z) in terms of phasors:

$$\boldsymbol{E}(r,\theta,z,t) = \widetilde{\boldsymbol{E}}(r,\theta,z)e^{-j\omega t}\,, \tag{2.2}$$

$$\boldsymbol{B}(r,\theta,z,t) = \widetilde{\boldsymbol{B}}(r,\theta,z)e^{-j\omega t}\,. \tag{2.3}$$

Provided the cavity is axially symmetric, $\widetilde{\boldsymbol{E}}(r,\theta,z)$ and $\widetilde{\boldsymbol{B}}(r,\theta,z)$ can be expanded as:

$$\begin{aligned}\widetilde{\boldsymbol{E}}(r,\theta,z) &= \sum_{m=0}^{\infty} \overline{\boldsymbol{E}}^{(m)} \\ &= \sum_{m=0}^{\infty} \Big(E_r^{(m)}(r,z)\cos(m\theta)\,\boldsymbol{e_r} + E_\theta^{(m)}(r,z)\sin(m\theta)\,\boldsymbol{e_\theta} \\ &\qquad + E_z^{(m)}(r,z)\cos(m\theta)\,\boldsymbol{e_z}\Big),\end{aligned} \tag{2.4}$$

$$\begin{aligned}\widetilde{\boldsymbol{B}}(r,\theta,z) &= \sum_{m=0}^{\infty} \overline{\boldsymbol{B}}^{(m)} \\ &= \sum_{m=0}^{\infty} \Big(B_r^{(m)}(r,z)\sin(m\theta)\,\boldsymbol{e_r} + B_\theta^{(m)}(r,z)\cos(m\theta)\,\boldsymbol{e_\theta} \\ &\qquad + B_z^{(m)}(r,z)\sin(m\theta)\,\boldsymbol{e_z}\Big),\end{aligned} \tag{2.5}$$

where $m = 0, 1, 2, \ldots$, corresponds to the monopole, dipole, quadrupole modes, etc., $\boldsymbol{e_r}$, $\boldsymbol{e_\theta}$, and $\boldsymbol{e_z}$ are the unit vectors in the r, θ and z direction respectively. These modes correspond to one polarization, while the other polarization is obtained by rotating the (r, θ) plane by $\frac{\pi}{2m}$.

2.1.3. Figures of merit of a cavity

Due to the finite resistance, a cavity consumes power whether normal conducting or superconducting. However, the power consumption is of course much lower for the

latter. For mode m , the time averaged stored energy $U^{(m)}$ within a cavity volume V consists of the energy stored in the electric field and in the magnetic field:

$$U^{(m)} = \frac{1}{4}\left(\varepsilon_0 \int_V \left|\bar{\boldsymbol{E}}^{(m)}\right|^2 dV + \mu_0 \int_V \left|\bar{\boldsymbol{H}}^{(m)}\right|^2 dV\right). \quad 2.6$$

Since the time averaged energy in the electric field equals that in the magnetic field, the total energy is given by:

$$U^{(m)} = \frac{1}{2}\varepsilon_0 \int_V \left|\bar{\boldsymbol{E}}^{(m)}\right|^2 dV = \frac{1}{2}\mu_0 \int_V \left|\bar{\boldsymbol{H}}^{(m)}\right|^2 dV. \quad 2.7$$

The average dissipated power $P_{sur}^{(m)}$ due to the surface resistance R_s is given by the integral of the square of the amplitude of magnetic field $\bar{\boldsymbol{H}}^{(m)}$ over the interior cavity surface[4] S:

$$P_{sur}^{(m)} = \frac{1}{2}R_s \int_S \left|\bar{\boldsymbol{H}}^{(m)}\right|^2 dS. \quad 2.8$$

The **unloaded quality factor** of mode m is defined to quantify the power dissipated in the cavity walls as:

$$Q_0^{(m)} = \frac{\omega_r U^{(m)}}{P_{sur}^{(m)}}, \quad 2.9$$

[4] Here I have assumed that the surface resistance does not vary over the cavity surface.

where ω_r is the angular frequency of mode m. By taking into account the power loss through couplers and beam pipes, $P_{ext}^{(m)}$, the **external quality factor**, $Q_{ext}^{(m)}$, can be defined as:

$$Q_{ext}^{(m)} = \frac{\omega U^{(m)}}{P_{ext}^{(m)}}. \tag{2.10}$$

The **loaded quality factor** $Q_L^{(m)}$ can be defined by considering both the power loss to the walls and the power loss due to the external coupling as:

$$Q_L^{(m)} = \frac{\omega U^{(m)}}{P_{ext}^{(m)} + P_{sur}^{(m)}}. \tag{2.11}$$

$Q_L^{(m)}$ is related to the external and unloaded quality factors by:

$$\frac{1}{Q_L^{(m)}} = \frac{1}{Q_{ext}^{(m)}} + \frac{1}{Q_0^{(m)}}. \tag{2.12}$$

The **shunt impedance** R_{sh} is defined as the ratio between the longitudinal voltage of mode m, $V_{\parallel}^{(m)}$, and the dissipated power $P_{sur}^{(m)}$:

$$R_{sh}^{(m)} = \frac{\left|V_{\parallel}^{(m)}\right|^2}{P_{sur}^{(m)}} = \frac{\left|V_{\parallel}^{(m)}\right|^2 Q_0^{(m)}}{\omega U^{(m)}}. \tag{2.13}$$

The longitudinal voltage $V_{\parallel}^{(m)}$ at a radial offset r is defined as the magnitude of the line integral of the electric field seen by an ultra-relativistic particle in the z direction:

$$V_{\parallel}^{(m)}(r) = \left| \int E_z^{(m)}(r,z) \cos(m\theta)\, e^{-i(kz-\phi)} dz \right|, \qquad 2.14$$

where $k = \omega_r / c$ is the wave number and ϕ an arbitrary phase.

By normalizing the shunt impedance to $Q_0^{(m)}$, a new parameter called R/Q (R over Q), $\left(\frac{R}{Q}\right)^{(m)}$, is defined as:

$$\left(\frac{R}{Q}\right)^{(m)} = \frac{1}{r^{2m}} \frac{\left|V_{\parallel}^{(m)}(r)\right|^2}{2\omega_r U^{(m)}}. \qquad 2.15$$

A factor of 1/2 is added due to the conversion from peak to RMS voltage. Since $V_{\parallel}^{(m)}(r) \propto r^m$ [30], the voltage squared is normalized with r^{2m}. For monopole modes, R/Q has the unit of $[\Omega]$, while a dipole mode $[\Omega \cdot cm^{-2}$ or $\Omega \cdot m^{-2}]$.

The shunt impedance R_{sh} should be large for the accelerating mode so that the dissipated power is minimized. The R/Q determines the level of mode excitation by a beam travelling through the cavity. The higher R/Q, which is only dependent on the cavity shape, the stronger the beam-cavity interaction is. The R/Q needs to be small for HOMs because these tend to dilute the beam quality [3].

2.1.4. TESLA and third harmonic cavities

There are two types of accelerating cavities installed in FLASH and the E-XFEL: TESLA and third harmonic cavities. The acceleration is solely provided by the

TESLA cavities working at 1.3 GHz [13]. The third harmonic cavities can be regarded as a scaled down version of the TESLA cavity as shown in Figure 2.1. The iris size and the beam pipe diameter are not directly scaled by one-third, but they are larger in order to increase the damping of the HOMs. These have further consequence on the HOM spectrum as it will be shown in Chapter 4.

Both the TESLA and third harmonic cavities are made of niobium and have nine cells. The mid-cell length is synchronized with the half period of the accelerating mode, while the end cells have slightly different shape to have equal field amplitudes and prevent the trapping of HOMs [13] with higher R/Q. Each cavity has a fundamental power coupler to input the RF power from a klystron and a field probe to detect the accelerating field for calibration and control used in the LLRF system as it will be discussed in Chapter 5. Two additional couplers are installed to damp the beam-excited HOMs [13]. The whole cavity is cooled to below 2 K with superfluid helium to operate in the superconducting state.

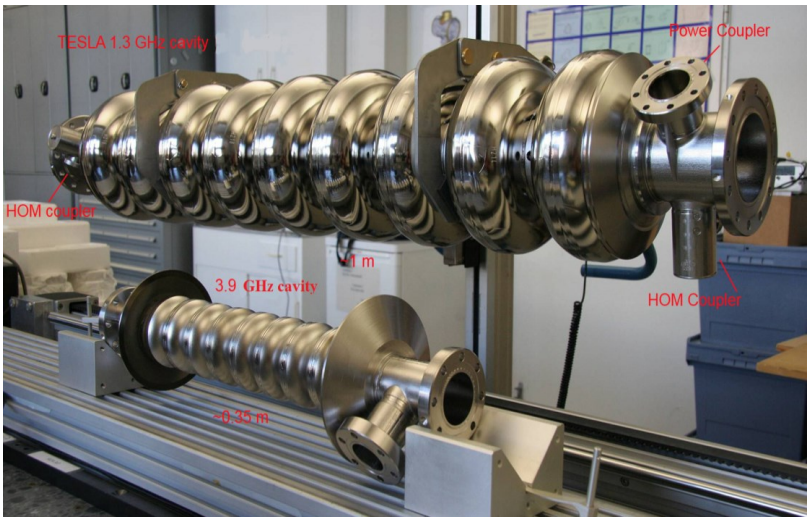

Figure 2.1 Picture of a nine cell niobium superconducting TESLA cavity and a third harmonic cavity. They are 1 meter and 0.35 meters long respectively. Both are equipped with two HOM couplers, one fundamental power coupler and one RF field pickup. (Courtesy of DESY)

The parametric description of the half-cell can be found in [13] for the TESLA cavity and in [31] for the third harmonic cavity. The parametric contour of the TESLA cavity is reproduced in Figure 2.2. The associated parameters are summarized in Table 2-1. The two end cells have slightly different geometry.

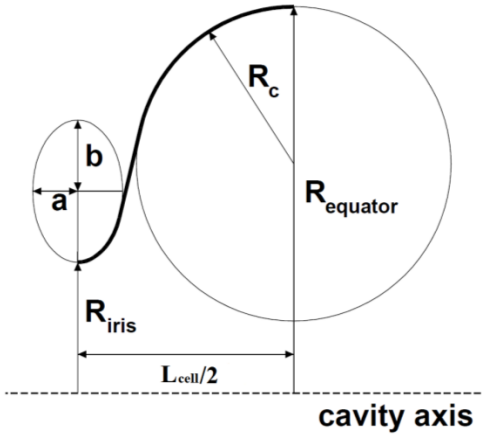

Figure 2.2 Parametric contour of a half-cell of the TESLA cavity

Table 2-1 TESLA half-cell shape parameters (all dimensions in mm)

	Midcup	Endcup 1	Endcup 2
Equator radius $R_{equator}$	103.3	103.3	103.3
Iris radius R_{iris}	35	39	39
Radius of circular arc R_c	42.0	40.3	42
Horizontal half axis a	12	10	9
Vertical half axis b	19	13.5	12.8
Half-cell length L_{cell}	57.5	56.0	57.0

A schematic drawing of a TESLA cavity is shown in Figure 2.3.

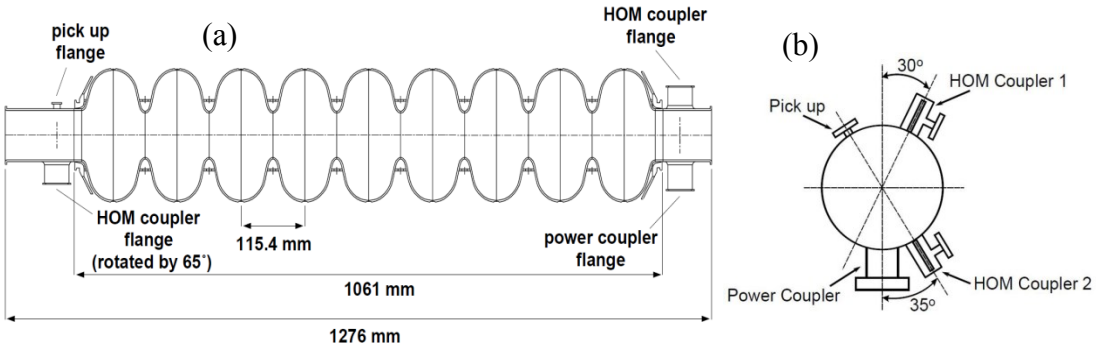

Figure 2.3 (a) Drawing of the TESLA cavity with one power coupler, one pickup probe and two HOM couplers. (b) The two HOM couplers span an angle of 115°. By convention, the HOM coupler close to the power coupler is called HOM coupler 1 or HOM1 and the other HOM2. (Courtesy of DESY)

The accelerating gradient of TESLA cavity is designed to be 23.6 MV/m with a unloaded quality factor 10^{10} [32]. The R/Q for the fundamental mode is 518 Ω [13]. Eight cavities, and two quadrupole magnets are placed in a cryomodule [32]. The E-XFEL contains 97 such cryomodules while FLASH has seven.

In contrast, a third harmonic cavity works with a fundamental frequency of 3.9 GHz. The designed accelerating gradient is 14 MV/m [33]. The R/Q for the fundamental mode is 375 Ω. Eight cavities are organized in a special cryomodule which is used for linearization of the longitudinal phase space of the electron beam [16] at the E-XFEL.

2.2. Wakefields and Impedances

Wakefields are a consequence of the beam-cavity interaction. They can be described as a summation of HOMs in time domain. Equivalently, these fields can also be described in frequency domain by the impedances.

2.2.1. Wakefields

When a bunch of relativistic electrons traverses a cavity, it excites wakefields. These fields can exert forces on the bunch itself and on the following bunches. Therefore one can distinguish between short-range and long-range wakefields. These wakefields can be calculated based on the wake functions from a point charge (or delta function charge distribution) by convolution with the bunch charge distribution [34].

To illustrate the wakefields some of the main aspects will be investigated. Figure 2.4 shows a leading charge q_1 with cylindrical coordinates (r_1, θ_1, z_1) traveling in the $\boldsymbol{e_z}$ direction, followed by a trailing charge q_2 with coordinates (r_2, θ_2, z_2) at a distance s behind q_1. The Lorentz force experienced by q_2 due to the fields generated by the leading charge $q_1$can be calculated as in equation 2.16:

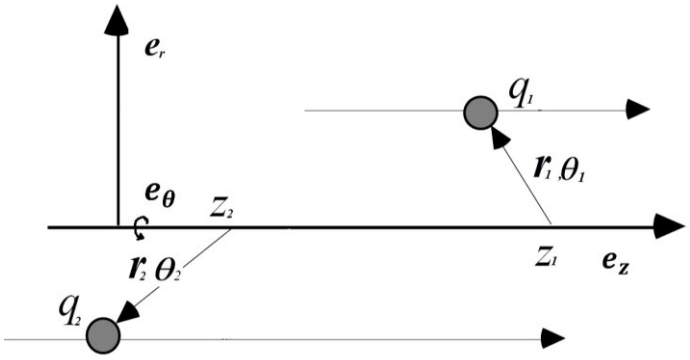

Figure 2.4 A point charge q_1 (leading charge) with coordinates (r_1, θ_1, z_1) and a trailing charge q_2 with coordinates (r_2, θ_2, z_2) travel at speed of light c along the e_z axis. The accelerating structure is considered to be cylindrical symmetric around this axis. The distance between the two charges is $s = z_1 - z_2$ [35].

$$\boldsymbol{F} = \frac{d\boldsymbol{p}}{dt} = q_2(\boldsymbol{E} + c\boldsymbol{e_z} \times \boldsymbol{B}). \tag{2.16}$$

The **wake potential** is defined as the integral of the Lorentz force experienced by a unit of trailing charge q_2 along the length L of the structure due to a unit of leading charge q_1:

$$\boldsymbol{W}(r_1, \theta_1, r_2, \theta_2, s) = \frac{1}{q_1 q_2}\int_0^L \boldsymbol{F} dz = \frac{1}{q_1}\int_0^L dz(\boldsymbol{E} + c\boldsymbol{e_z} \times \boldsymbol{B})_{t=(z+s)/c}. \tag{2.17}$$

For ultra-relativistic charges, causality (no signal can travel faster than the speed of light) requires that the wake potential is 0 for $s < 0$ (q_2 ahead of q_1). The wake potential can be decomposed into a longitudinal part $\boldsymbol{W}_\parallel$ (along $\boldsymbol{e_z}$ direction) and a transverse part $\boldsymbol{W}_\perp$ (in the $\mathbf{r}$-$\boldsymbol{\theta}$ plane). The two components are related by the Panofsky-Wenzel theorem [36]:

$$\frac{\partial}{\partial s}\boldsymbol{W}_\perp(r_1, \theta_1, r_2, \theta_2, s) = -\boldsymbol{\nabla}_\perp \boldsymbol{W}_\parallel(r_1, \theta_1, r_2, \theta_2, s)\,. \tag{2.18}$$

Equation 2.18 indicates that the transverse wake potential can be calculated by integration of the transverse gradient of the longitudinal wake potential. It should be noted that the theorem applies to a cavity with arbitrary geometry and it does not require cylindrical symmetry.

Provided that the cavity exhibits cylindrical symmetry, the longitudinal and transverse wake potentials can be written as a multipole expansion [30]:

$$\boldsymbol{W}_{\parallel}(r_1, \theta_1, r_2, \theta_2, s) = \sum_{m=0}^{\infty} r_1^m \, r_2^m W_{\parallel}^{(m)}(s) \cos(m\theta_1 - m\theta_2) \, \boldsymbol{e_z}, \tag{2.19}$$

$$\begin{aligned} \boldsymbol{W}_{\perp}(r_1, \theta_1, r_2, \theta_2, s) \\ = \sum_{m=1}^{\infty} m r_1^m \, r_2^{m-1} W_{\perp}^{(m)}(s) [\cos(m\theta_1 - m\theta_2) \boldsymbol{e_r} \\ + \sin(m\theta_1 - m\theta_2) \, \boldsymbol{e_\theta}], \end{aligned} \tag{2.20}$$

where $W_{\parallel}^{(m)}(s)$ and $W_{\perp}^{(m)}(s)$ are the m-pole longitudinal and transverse wake potential respectively. They are related by:

$$W_{\perp}^{(m)}(s) = -\int_{-\infty}^{s} ds' \, W_{\parallel}^{(m)}(s'), \text{ for } m > 0. \tag{2.21}$$

The consequence of equation 2.20 is that there is no transverse monopole wake potential. The dipole wake potential does not depend on the offset of the test charge q_2, but is proportional to the offset $r_1$of the leading charge q_1.

The longitudinal and transverse m-pole wake potentials can be written as a sum of m-pole modes [4]:

$$W_{\parallel}^{(m)}(s) = -\sum_{n} \omega_{mn} \left(\frac{R}{Q}\right)^{(mn)} \cos\left(\frac{\omega_{mn} s}{c}\right) H(s), \quad 2.22$$

$$W_{\perp}^{(m)}(s) = c \sum_{n} \left(\frac{R}{Q}\right)^{(mn)} \sin\left(\frac{\omega_{mn} s}{c}\right) H(s), m > 0, \quad 2.23$$

where $\left(\frac{R}{Q}\right)^{(mn)}$ and ω_{mn} are the R/Q and angular frequency of the n^{th} m-pole mode respectively. $H(s)$ is the Heaviside step function (derived in Appendix C):

$$H(s) = \begin{cases} 1 & s > 0\,, \\ \frac{1}{2} & s = 0\,, \\ 0 & s < 0\,. \end{cases} \quad 2.24$$

In a well-designed linac the beam travels with a small offset as compared to the radius of the beam pipe. In this case, the longitudinal wake potential is dominated by monopole modes, and the transverse one by dipole modes [35]. Therefore, for small beam offsets one can approximate:

$$\boldsymbol{W}_{\parallel} \cong -\sum_{n} \omega_{0n} \left(\frac{R}{Q}\right)^{(0n)} \cos\left(\frac{\omega_{0n} s}{c}\right) H(s) \boldsymbol{e_z}, \tag{2.25}$$

$$\boldsymbol{W}_{\perp} \cong r_1 c \sum_{n} \left(\frac{R}{Q}\right)^{(1n)} \sin\left(\frac{\omega_{1n} s}{c}\right) H(s) \left[\cos(\theta_1 - \theta_2)\boldsymbol{e_r} + \sin(\theta_1 - \theta_2)\, \boldsymbol{e_\theta}\right]. \tag{2.26}$$

For small beam offsets, the longitudinal wake potential is approximately independent of the beam offset of the leading bunch, while the transverse wake potential has an approximately linear dependence of the beam offset of the leading bunch. Also, the monopole mode has no azimuthal dependence on the transverse position. This feature of monopole modes enables the measurements of the beam phase with respect to the accelerating RF field inside the cavity. The details will be discussed in Chapter 5. For dipole modes, the linear dependence on the beam offset allows us to measure the beam position, which is the topic of Chapter 6.

2.2.2. Impedances

The wake potential can be calculated in time domain as in section 2.2.1. It can also be equivalently expressed in frequency domain, with the help of the Fourier transform.

The longitudinal and transverse impedances can be defined by the Fourier transform of the longitudinal and transverse wake functions respectively as:

$$Z_{\parallel}(r_1,\theta_1,r_2,\theta_2,\omega) = \int_{-\infty}^{\infty} dt\,[\boldsymbol{W}_{\parallel}(r_1,\theta_1,r_2,\theta_2,s)e^{-j\omega t}]_{t=(z+s)/c}\,, \tag{2.27}$$

$$Z_{\perp}(r_1,\theta_1,r_2,\theta_2,\omega) = j\int_{-\infty}^{\infty} dt\,[\boldsymbol{W}_{\perp}(r_1,\theta_1,r_2,\theta_2,s)e^{-j\omega t}]_{t=(z+s)/c}\,. \tag{2.28}$$

The impedance $Z_{\parallel}$, in general, is a complex quantity and can be decomposed into a real part Z_r and an imaginary part Z_i:

$$Z_{\parallel}(r_1,\theta_1,r_2,\theta_2,\omega) = Z_r(r_1,\theta_1,r_2,\theta_2,\omega) + jZ_i(r_1,\theta_1,r_2,\theta_2,\omega)\,. \tag{2.29}$$

$Z_r(\omega)$ and $Z_i(\omega)$ are even and odd functions of ω respectively.

$$\int_{-\infty}^{\infty} Z_r(r_1,\theta_1,r_2,\theta_2,\omega)\cos(\omega t)\,d\omega = \int_{-\infty}^{\infty} Z_i(r_1,\theta_1,r_2,\theta_2,\omega)\sin(\omega t)\,d\omega. \tag{2.30}$$

The transverse and longitudinal impedances are related by equation 2.31 following from the Panofsky-Wenzel theorem described in section 2.2.1:

$$Z_{\perp}(r_1,\theta_1,r_2,\theta_2,\omega) = \frac{c}{\omega}\nabla_{\perp}Z_{\parallel}(r_1,\theta_1,r_2,\theta_2,\omega)\,. \tag{2.31}$$

In summary, metallic cavities based on superconducting technology can be used to accelerate electron beams. The figures of merit of a RF cavity are generally used to

compare different cavity designs in accelerator physics. The accelerating gradient of a cavity is designed to be as high as possible to reduce the linac's length. The maximum achievable accelerating gradient is limited by the surface magnetic field for superconducting cavities.

The sum of beam-excited HOMs in an accelerating cavity constitutes the wakefield. The eigenmodes can be found by using computer codes like CST [37] based on finite element method. Wakefields can be also directly probed by beam-based experimental setups such as ASSET [38] or be measured by a bench-top wire measurement [39]. When the beam travels close to the cavity axis, monopole and dipole modes dominate the longitudinal and transverse wakefields respectively. Under such an approximation, longitudinal wakefields have no dependence on the offset of the excitation bunch (leading bunch), while transverse wakefields depend linearly on it.

Each mode as described in section 2.1.2 can be indexed as either TM_{mnp} or TE_{mnp} according to the field variation in all three dimensions (θ, r, z): m (m = 0, 1, 2, 3, …) is the number of full period variations in θ of the field components. The subscript n ($n = 1, 2, 3, ...$) is the number of zeros of the axial field component in the radial direction in the range $0 < r \leq R_c$ where R_c is the cell radius. The subscript p ($p = 0, 1, 2, 3, ...$) is the number of half period variations in $\boldsymbol{e_z}$ of the fields [11]. These modes are grouped into different passbands and obey the dispersion relation of an infinite periodic structure. The field distribution of these modes can be measured with a bead pulling technique [24].

In the next chapter, a circuit model is used to study the modes from the TM_{010} and TM_{011} bands of the TESLA cavity. A single mode can be studied by a resonant circuit. A chain of coupled resonant circuits can be used to represent a band of modes. The mode excitation by a beam is then simulated with this coupled circuit model.

Chapter 3 - A Circuit Model of Higher Order Modes in the Cavity

RLC[5] circuits are widely used in filter synthesis [40] and various other applications. RF cavities driven by a beam or klystron can also make use of these circuits through carefully designed models [41], [42]. The intrinsic properties of the cavities such as their eigenmodes can be calculated as well [43], [44].

The coupled circuit model was originally applied to multi-cell accelerating cavities by D. Nagle, E. Knapp and B. Knapp [43]. The circuit model is focused on a particular band of modes. For a monopole band, in general a single chain of coupled circuit is sufficient [45], while for dipole bands, two chains of coupled RLC circuits are required to represent two coupled bands (Appendix D). Therefore the computation is time and computer memory efficient. The advantage is evident when the structure is highly complicated [46].

The coupled circuit model is presented in section 3.1. The dispersion curve can be obtained from an infinite periodic coupled circuit. The infinite circuit is then truncated to find the mode frequencies and their distribution. In section 3.2, the truncated circuit is driven with beam. The HOM response can be studied thereof. The model is used to aid the HOMBPhM development in Chapter 5.

3.1. Single Chain Circuit Model

Each cell, in principle, can support an infinite number of modes. These modes can be represented by simple RLC circuits. When cells are coupled together, each mode from the single cell is split into a number of normal modes depending on the number of coupled cells. The coupling between the cells can be either inductive or capacitive [46].

[5] RLC represents Resistor, Inductor and Capacitor.

3.1.1. Infinite periodic coupled circuit

In order to obtain the dispersion relation of a monopole band, an infinite periodic coupled circuit is used. The model is shown in Figure 3.1. Each circuit unit n consists of two inductors $2L_n$, one capacitor C_n and one conductor G_n. A current source I_n is included to represent a beam excitation. Adjacent circuit units are coupled magnetically via the mutual inductances $M_{n-1,n}$ and $M_{n,n+1}$,

$$M_{n-1,n} = \kappa_{n-1,n}\sqrt{2L_{n-1} \times 2L_n},\ M_{n,n+1} = \kappa_{n,n+1}\sqrt{2L_n \times 2L_{n+1}}. \tag{3.1}$$

where $\kappa_{n-1,n}$ is a coupling constant between cells $n-1$ and n.

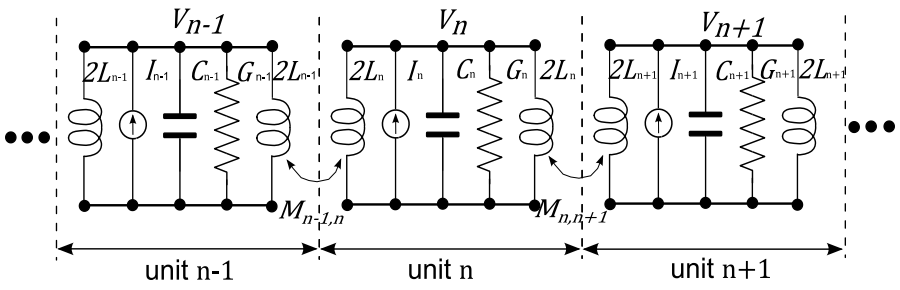

Figure 3.1 Chain of coupled parallel RLC circuits. The conductance G represents the losses in each cell. The circuit has an infinite number of identical units, each representing a cell in a multi-cell cavity.

The parameters L_n, C_n, and G_n are related to the parameters of a RF cavity by [41]:

$$\text{Inductance: } L_n = \frac{\left(\frac{R}{Q}\right)^{(n)}}{\omega_n}, \tag{3.2}$$

$$\text{Capacitance: } C_n = \frac{1}{\left(\frac{R}{Q}\right)^{(n)}\omega_n}, \tag{3.3}$$

$$\text{Conductance: } G_n = \frac{1}{\left(\frac{R}{Q}\right)^{(n)} Q_0^{(n)}}, \tag{3.4}$$

From equations 3.2 and 3.3, it is clear that:

$$\omega_n = \frac{1}{\sqrt{L_n C_n}}, \tag{3.5}$$

$$\left(\frac{R}{Q}\right)^{(n)} = \sqrt{\frac{L_n}{C_n}}. \tag{3.6}$$

The circuit can be analyzed based on Kirchhoff's law in the time domain or in the frequency domain. The dynamics of cell n are described by equation 3.7 as derived in [41]:

$$\frac{1}{\omega_n^2}\frac{d^2 v_n}{dt^2} + \frac{1}{Q_n}\frac{1}{\omega_n}\frac{dv_n}{dt} + v_n = \frac{1}{2}\kappa(v_{n-1} + v_{n+1}) + \frac{1}{\omega_n}\frac{di_n}{dt}, \tag{3.7}$$

where I assumed $\kappa_{n-1,n} = \kappa_{n,n+1} \equiv \kappa$, the v_n and i_n are given by,

$$v_n = \sqrt{C_n} V_n\,, \qquad i_n = \sqrt{L_n} I_n. \tag{3.8}$$

Imposing the condition $i_n = 0$ (no beam), Q_n is infinite (lossless), and the Floquet periodic condition [11] $v_n = v_{n-1}e^{j\phi}$, the analytic dispersion relation can be obtained:

$$\omega^2 = \omega_r^2(1 - \kappa\cos\phi), \tag{3.9}$$

where ω_r is the resonant frequency of a mode in a single cell, and ϕ the phase advance per cell. The coupling term κ can be obtained either from the fitting of data from single cell simulation or from the 0 and π mode of each band,

$$\omega_r = \sqrt{\frac{2\omega_0^2\omega_\pi^2}{\omega_0^2+\omega_\pi^2}} = \omega_{\frac{\pi}{2}}, \tag{3.10}$$

$$\kappa = \frac{\omega_\pi^2 - \omega_0^2}{\omega_0^2 + \omega_\pi^2}. \tag{3.11}$$

The fractional bandwidth is defined as,

$$\delta\omega \approx \omega_r\kappa. \tag{3.12}$$

A number of quantities can be calculated from the circuit model and are summarized in Figure 3.2. In a TESLA cavity, the TM011 band shows group velocity $v_g < 0$, while the TM010 and TE111 bands exhibit $v_g > 0$.

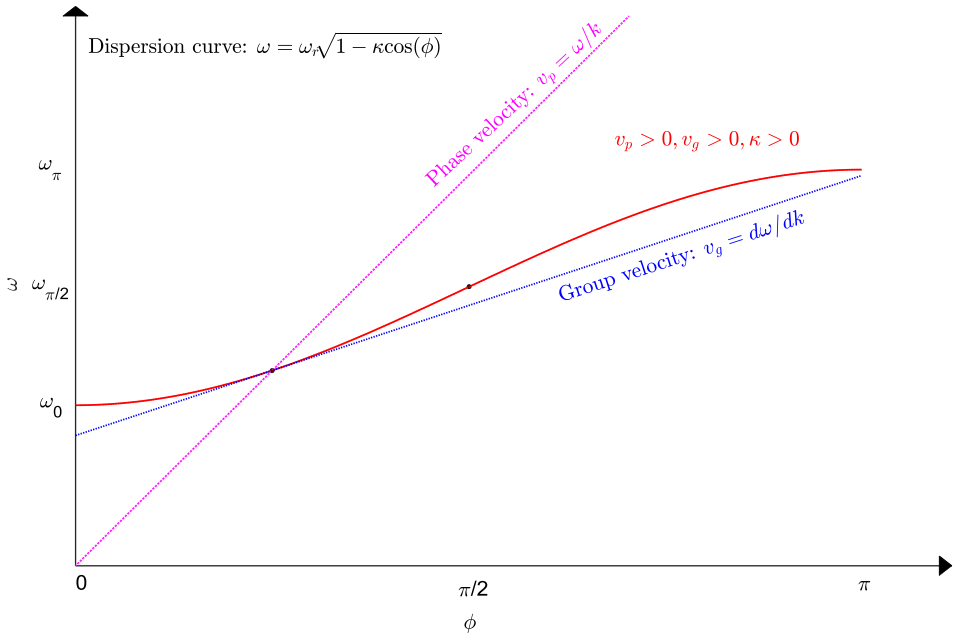

Figure 3.2 Dispersion curve for forward wave; the phase and group velocities can be calculated from the curve. The phase advance ϕ per cell equals the wave number k times the cell length L_{cell}.

3.1.2. Coupling from the nearest neighbour and beyond

If only the nearest neighbour coupling (coupling between unit n and $n-1$ or $n+1$) is considered, as depicted in Figure 3.1, the dispersion relation is given by equation 3.9. If the next nearest neighbour coupling (coupling between unit n and $n-2$ or $n+2$) is included, the dynamics of cell n can be extended as:

$$\frac{1}{\omega_n^2}\frac{d^2v_n}{dt^2} + v_n = \frac{1}{2}\kappa_1(v_{n-1} + v_{n+1}) + \frac{1}{2}\kappa_2(v_{n-2} + v_{n+2}) + \frac{1}{\omega_n}\frac{di_n}{dt}, \qquad 3.13$$

where κ_1 is the nearest coupling and κ_2 the next nearest neighbour coupling. The second term in equation 3.7 is negligible due to the small losses in SRF cavities. This equation can be extended in a straightforward manner if more coupling terms

are considered. If N coupling terms are taken into account, equation 3.13 can be extended to:

$$\frac{1}{\omega_n^2}\frac{d^2 v_n}{dt^2} + v_n = \frac{1}{2}\sum_{i=1}^{N} \kappa_i (v_{n-i} + v_{n+i}). \tag{3.14}$$

The dispersion relation again can be obtained by applying Floquet periodic condition as:

$$\omega^2 = \omega_r^2 \left(1 - \sum_{i=1}^{N} \kappa_i \cos(i\phi)\right). \tag{3.15}$$

3.1.3. Finite coupled circuit

The dispersion relation describes the eigenmode solution to an infinitely periodic structure. For a nine cell TESLA cavity, the infinite model has to be truncated by specifying the boundary conditions as it will be discussed in the next two sections. Equations 3.13 (for $n = 1 \ldots 9$) form a set of nine homogeneous differential equations that can be written in matrix form as:

$$\boldsymbol{H} \cdot \boldsymbol{v} = \omega^2 \boldsymbol{v}, \tag{3.16}$$

where $\boldsymbol{H}$ contains the information about the system, and $\boldsymbol{v}$ is its eigen vector. The angular frequency ω serves as the eigen values of the system. An example of matrix $\boldsymbol{H}$ for the case $N = 1$ is shown in equation 3.17. The coupling term κ_c represents the coupling strength to the beam pipes.

$$\boldsymbol{H} = \begin{bmatrix} 1+\kappa_c & \kappa_1/2 & \cdots & 0 & 0 \\ \kappa_1/2 & 1 & & 0 & 0 \\ \vdots & & \ddots & \vdots & \\ 0 & 0 & & 1 & \kappa_1/2 \\ 0 & 0 & \cdots & \kappa_1/2 & 1+\kappa_c \end{bmatrix}. \qquad 3.17$$

In the following subsections, the coupling strength κ_i will be obtained for the first and second monopole bands separately by fitting equation 3.15 to the eigenmodes of a TESLA cavity. With the coupling terms determined, the infinite circuit is then truncated to find nine eigenmodes in each monopole band supported by the nine cell cavity.

3.1.4. Circuit model for the 1st monopole band of the TESLA cavity

The first monopole band of the TESLA cavity contains the 1.3 GHz mode used for acceleration. In order to obtain the coupling strength, equation 3.15 is used to fit, in a least square sense, the first monopole band of a TESLA cavity, as shown in Figure 3.3 (a). The eigenmode frequencies and the associated phase advances of the TESLA cavity are cited from the TESLA cavity simulation reported in [35]. The simulation was computed with computational code MAFIA. Therefore later the eigenmode data from this report is referred to as MAFIA results or data for the convenience of discussion. The discrepancies between the fitting and MAFIA results are shown in Figure 3.3 (b).

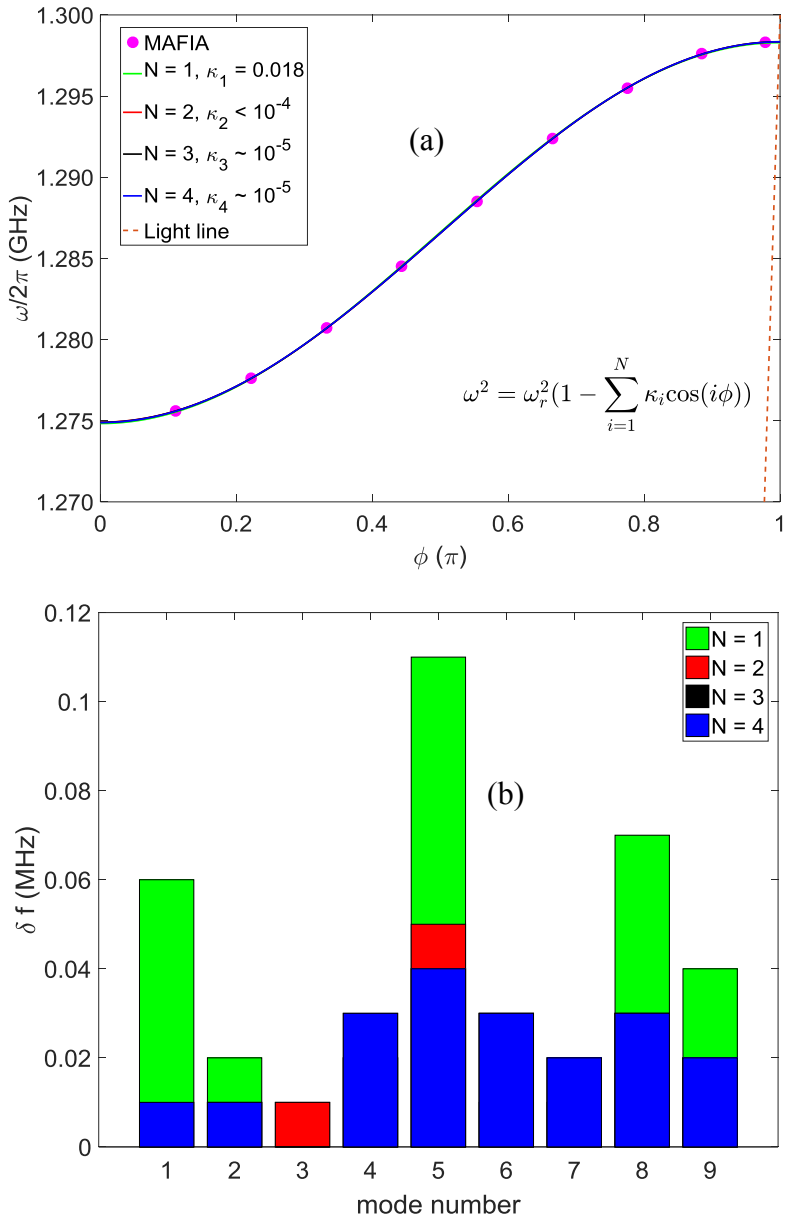

Figure 3.3 (a) Dispersion curve for the first monopole band. N indicates the number of coupling terms used in the calculation of the dispersion curve, e.g. $N = 1$ means the nearest neighbour coupling. MAFIA stands for the eigenmodes of a TESLA cavity that are cited from [35]. (b) The absolute difference of eigen frequencies calculated from the circuit model and the MAFIA simulation.

The nearest neighbour coupling strength $\kappa_1$is found to be 1.8 % (equation 3.11 also gives 1.8 % based on ω_π and ω_0) and the next nearest neighbour coupling κ_2 is below 0.01%. Therefore, it is sufficient to represent the first monopole band by using the nearest neighbour coupling to get absolute error below 0.1 MHz, which is within the precision of the results in [35].

Next, the infinite circuit is truncated to a nine-unit circuit with inclusion of additional coupling term κ_c to the beam pipe for the first and the ninth unit. The method of how to truncate the circuit model to obtain the desired π mode field flatness is descried in [24]. κ_c is found to be twice κ_1.

The eigen vectors of $\boldsymbol{H}$ in equation 3.16 represent the field distribution for each mode. The phase advance $\phi(z)$ per cell can be calculated as [35]:

$$\phi(z) = \cos^{-1}\left[\frac{E_z(r, z - L_{cell}) + E_z(r, z + L_{cell})}{2E_z(r, z)}\right], \qquad 3.18$$

where $E_z(r, z)$ is the electric field strength (components in an eigenvector) at position (r, z), L_{cell} is the length of a single cell. The field distribution obtained for each mode in the 1st monopole band is shown in Figure 3.4. For the TESLA cavity, a standing wave structure, the π mode (resonant at 1.3 GHz) in this TM010 band is used for electron beam acceleration [13] to get higher acceleration efficiency (higher shunt impedance) compared to other modes in the same band.

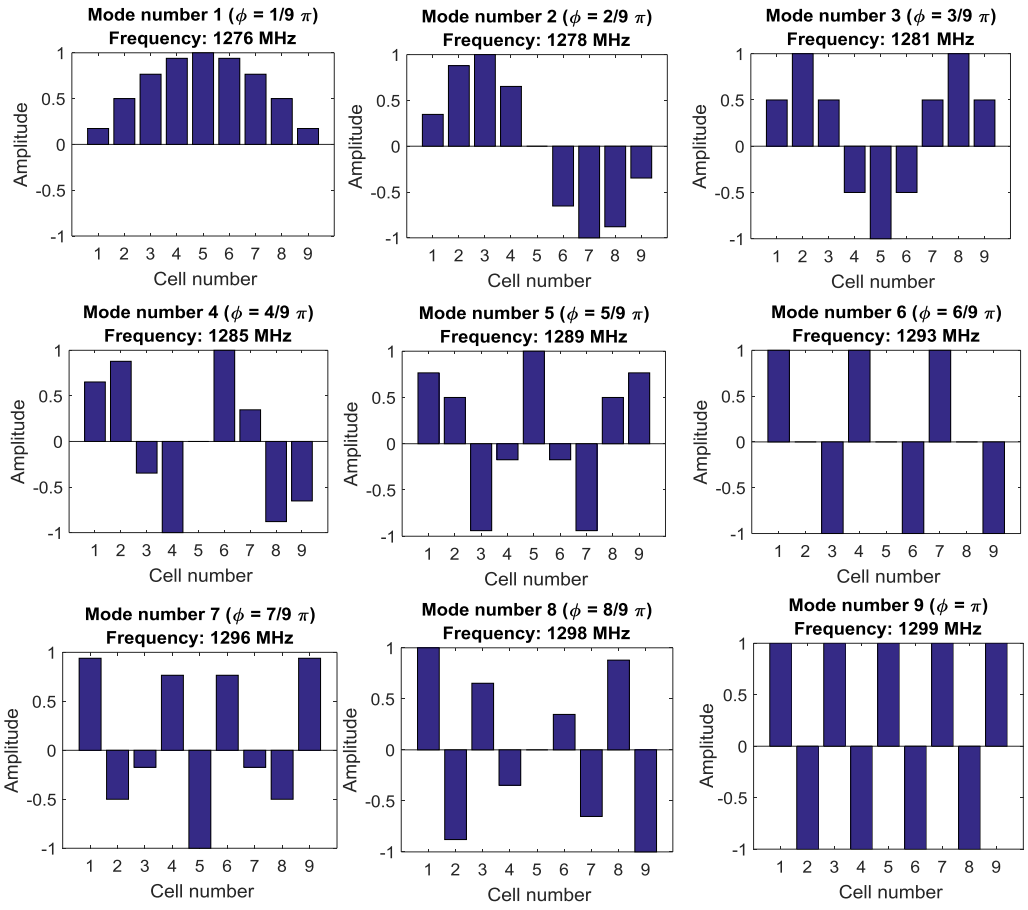

Figure 3.4 Field distributions of the 1st monopole band calculated by the circuit model; the eigen values and the eigen vectors in equation 3.16 correspond to the eigenmode frequencies and the field distributions respectively. The amplitudes are normalized with the maximum of the eigen vector value. ϕ is the phase advance per cell of each mode.

In summary, by fitting the analytic dispersion curve to the mode information from EM simulation, the inter-cell coupling constant for the fundamental band of the TESLA cavity is found to be κ_1 ~1.8 %. The additional coupling term introduced due to the beam pipe is found to be $2\kappa_1$. The bandwidth of the first monopole band is ~20 MHz. The narrow bandwidth indicates the weak coupling compared to the second monopole band as it will be shown in next section.

3.1.5. Circuit model for the 2nd monopole band

The methodology described in section 3.1.4 is applied for the 2nd monopole band to study these modes excited by beam in section 3.2 and to aid the beam phase monitor

design in Chapter 5. The dispersion curve and the frequency discrepancy are shown in Figure 3.5 (a) and (b) respectively.

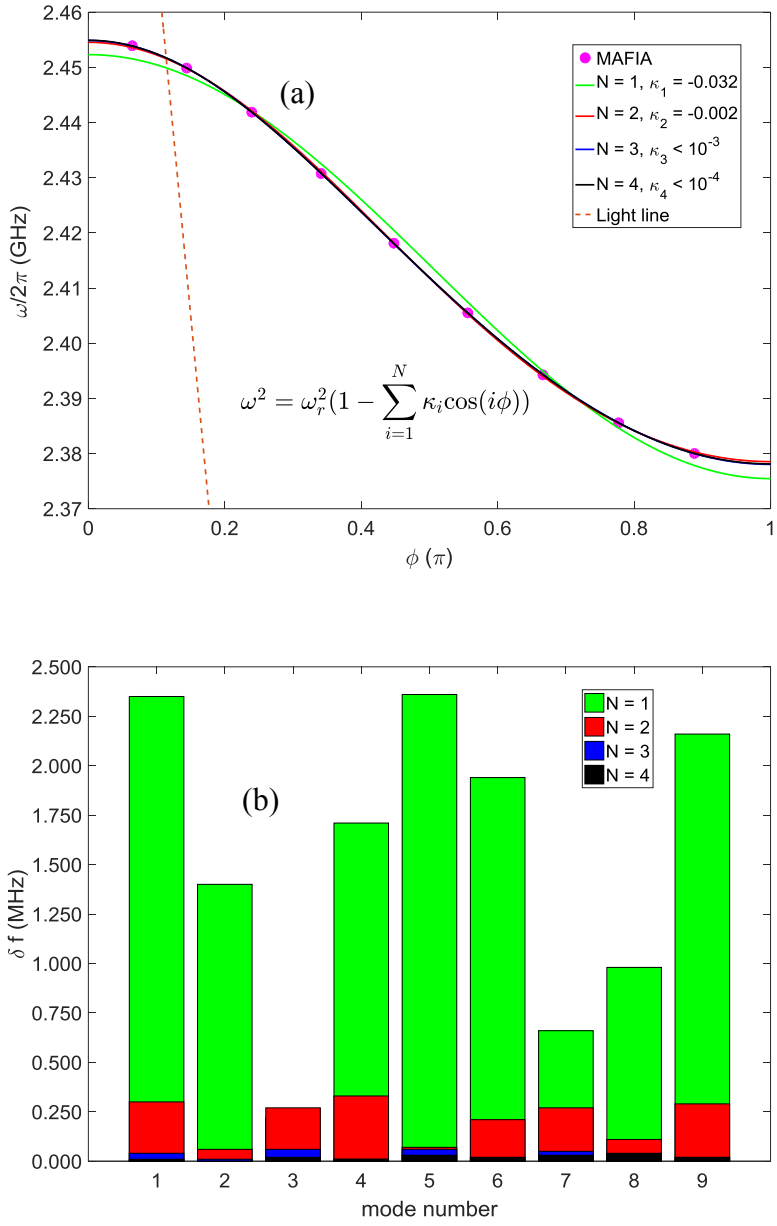

Figure 3.5 (a) The dispersion curve for the 2nd monopole band; *N* indicates the number of coupling terms used in the calculation of dispersion curve, e.g. $N = 1$ means the nearest neighbour coupling. MAFIA stands for the eigenmodes of a TESLA cavity that are cited from [35]. (b) The absolute difference of eigen frequencies calculated from the circuit model and the MAFIA simulation.

The nearest neighbour κ_1 and next nearest neighbour κ_2, are found to be -3% and -0.2% respectively. The coupling strength in this band is approximately 1% stronger

than that in the 1st monopole band. In order to get the frequency discrepancy close to 0.1 MHz, two coupling terms are required as show in Figure 3.5 (b).

The infinite circuit is truncated to nine circuit units with the inclusion of additional coupling terms to the beam pipes. The model is similar to the model for the first monopole band. Take unit 1 in the circuit as an example: in addition to the coupling to units 2 and 3, there are two coupling terms κ_{c1} and κ_{c2} to the beam pipe. These two coupling terms can be obtained in principle by scanning the parameter space. However, an analytic approach was adopted based on the coefficients of the characteristic polynomial of matrix $\boldsymbol{H}$ in equation 3.16 (see Appendix B). The eigenmode frequencies from the MAFIA simulation are used to construct the characteristic polynomial. The coupling terms κ_{c1} and κ_{c2} are found to be 1.4% and 0.03% respectively. This circuit model is referred to as tuned model later. By setting κ_{c1} and κ_{c2} to zero, an untuned model is obtained. With the tuned model, the eigenmode frequencies and the eigen vectors (field distributions) are obtained, as shown in Figure 3.6.

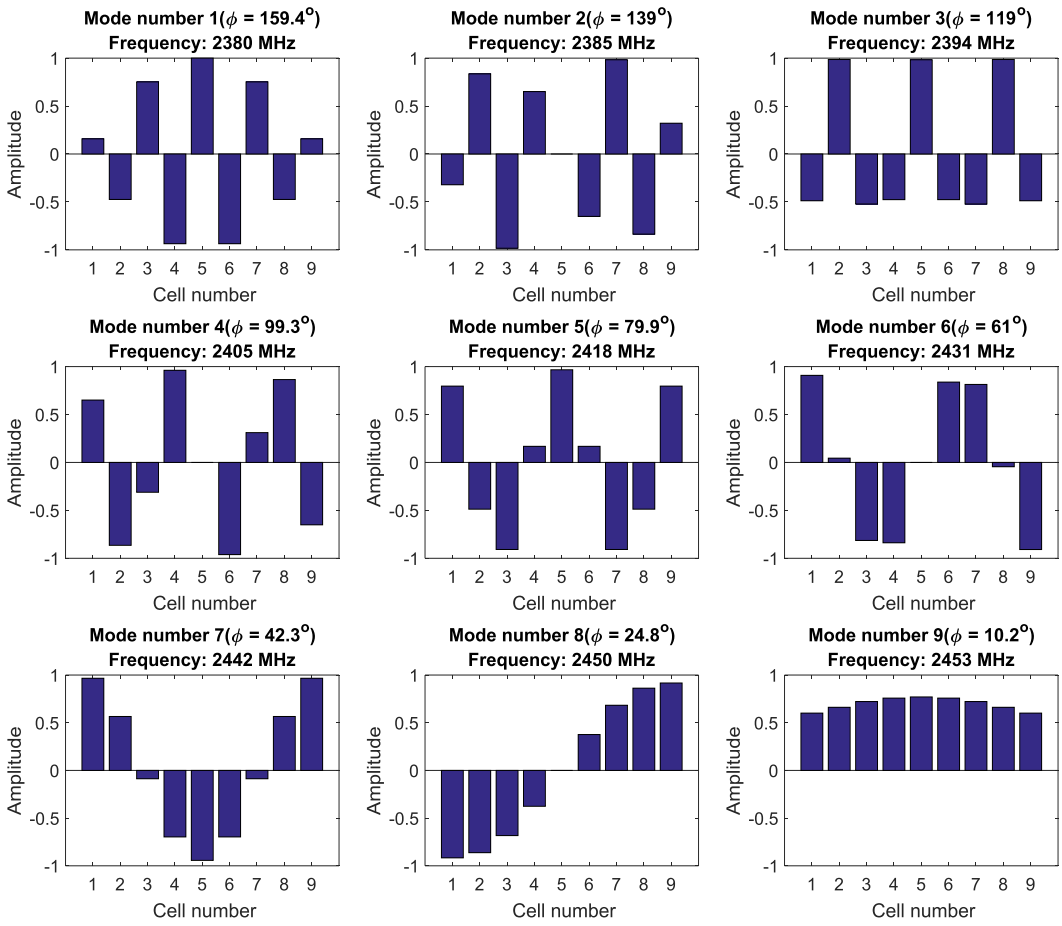

Figure 3.6 Field distributions of the 2nd monopole band from the tuned circuit model; the eigen values and the eigen vectors in equation 3.16 correspond to the eigenmode frequencies and the associated field distributions respectively. The amplitudes are normalized with the maximum of the eigen vector value.

The field distribution pattern is reversed as compared to the one in Figure 3.4. The mode frequency increases as the phase advance decreases, because of the negative group velocity.

The eigenmodes calculated from the tuned and the untuned circuits are shown in Figure 3.7. The discrepancies between the untuned model and MAFIA simulation are on average 4 MHz in frequency and 7° in phase advance. By tuning the model, the discrepancies decrease to 0.2 MHz and 0.8° respectively.

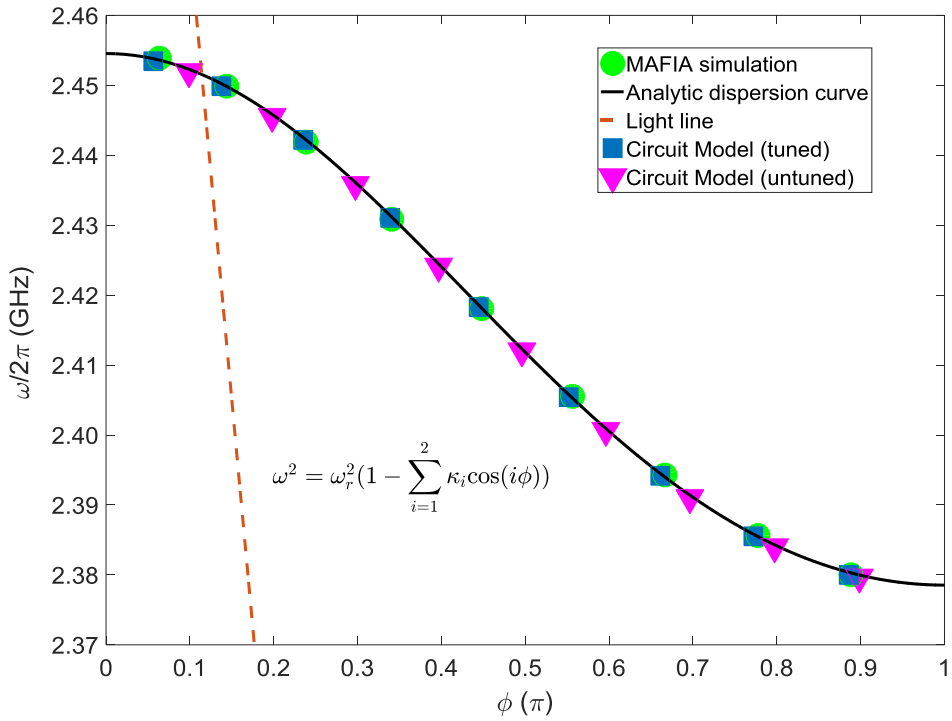

Figure 3.7 Dispersion curve for the 2nd monopole band and the eigenmodes from MAFIA and circuit model (tuned and untuned model). The tuning process here is essentially the way to find the numerical values of the unknown coupling terms.

In summary, by fitting the analytic dispersion curve, in a least square sense, to the mode information from EM simulation, two inter-cell coupling constants for the 2nd monopole band of the TESLA cavity are found to be -3% and -0.2% respectively. The additional coupling terms introduced due to the beam pipes are 1.4% and 0.03% respectively. The bandwidth is 79 MHz. After tuning, the circuit is ready to be driven by beam in order to investigate the beam phase determination, which will be discussed in Chapter 5

3.2. Beam-driven Circuit Model

The tuned circuit driven by beam is shown in Figure 3.8. There are nine circuit units coupled together magnetically by the mutual inductances M_1 and M_2. The circuit is driven by a set of Gaussian current pulses. The time delay t_0 between subsequent pulses corresponds to a half period of the 1.3 GHz accelerating mode in order to simulate the beam propagation. The coupled equation in unit n for the model is:

$$\frac{1}{\omega_r^2}\frac{d^2 v_n}{dt^2} + v_n = \frac{1}{2}\kappa_1(v_{n-1} + v_{n+1}) + \frac{1}{2}\kappa_2(v_{n-2} + v_{n+2}) + \frac{1}{\omega_r}\frac{di_n}{dt}, \qquad 3.19$$

where i_n represents a Gaussian beam current applied to the circuit unit n, and $i_n(t) = i_{n-1}(t - t_0)$. The tuned circuit model is constructed in Simulink®[6] and solved with a 5 ps step. The voltage signals at the first and ninth circuit units v_1 and v_9 are monitored. These signals will be used for the analysis of the beam phase in Chapter 5.

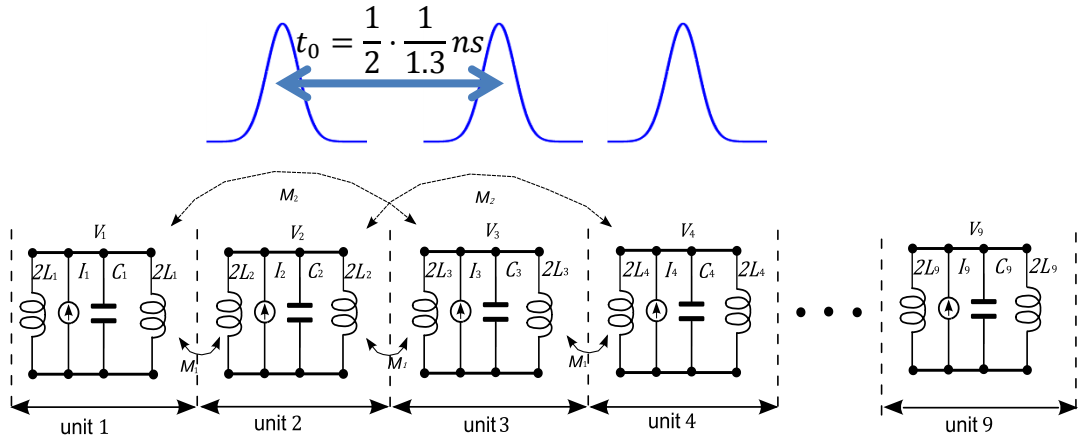

Figure 3.8 Nine unit circuit driven by a propagating Gaussian pulse I_n. The pulses are separated by t_0, which is equal to half period of the 1.3 GHz signal. Two magnetic coupling terms M_1 and M_2 are incorporated in the circuit.

In summary, the band of eigenmodes of an accelerating cavity can be modeled by a coupled circuit. The analytic dispersion relation of a coupled LC circuit can be found by setting Floquet periodic boundary condition. The coupling parameters associated with the dispersion curve can be obtained by fitting the circuit to EM simulations of a multi-cell cavity. In order to find the eigenmode solutions for a cavity, the infinite periodic circuit has to be truncated. This is accomplished by truncating the infinite circuit and introducing additional coupling terms. After the necessary parameters for the finite circuit model are determined, the model can be driven with beam. The voltage evolution over time in each cell can be studied

[6] The reason for choosing Simulink is that there are seamlessly integrated signal processing algorithms for visualization.

accordingly. The main motivation of the circuit model presented here is to aid the beam phase monitor development, as it will be presented in Chapter 5.

In next chapter, the eigenmode frequencies are measured for the TESLA and third harmonic cavities. The beam-excited mode frequencies are monitored over time to reveal their stability. The characterization of these modes is discussed.

Chapter 4 - HOM Spectra Measurements and Characterization

Knowledge of HOM spectra is important for HOMBPhM and HOMBPM design and optimization. Therefore it was important to measure these spectra and investigate their behaviour.

This chapter is arranged in the following way: the modal structure of an isolated TESLA cavity is presented in section 4.1. A statistical study of the HOMs was made to investigate the frequency variation from cavity to cavity for both FLASH and the E-XFEL. This is important to decide the electronics processing bandwidth. The frequency stability of beam-induced HOMs is of interest in itself and of particular importance for the long term operation of HOMBPM and HOMBPhM. Therefore the mode frequencies were monitored at FLASH over months. In section 4.2, the HOM spectra of the E-XFEL 3.9 GHz cavities are shown for both the single and coupled cavities.

4.1. HOM Spectra of TESLA Cavities

This section presents the transmission spectrum measured in a test cavity and a study of the stability of beam-excited spectra. The stability of the mode frequencies is of great importance because any shift in frequency will modulate the original signal (see Appendix B). The modes in a TESLA cavity are grouped into bands [35]. The focus is on the modes which are intended for beam diagnostics. More specifically, I report on the TM011, TE111, TM110 bands of the 1.3 GHz cavities [35].

4.1.1. Transmission spectra of a single cavity

To illustrate the HOM band structure of a TESLA cavity and for the convenience of later discussion, the transmission S_{21} (see Appendix E) of a test cavity was measured with a VNA (Vector Network Analyser) of type HP8720c with a frequency range from 50 MHz to 20 GHz. The transmission was measured from one antenna installed in one beam pipe to the other one at the other end as shown in

Figure 4.1. The cavity is filled with argon at 293 K. The frequency is scanned from 1600 MHz to 2600 MHz with a step of 2.5 kHz, which contains the TE111 (1st dipole band), TM110 (2nd dipole band) and TM011 (2nd monopole band) bands. The mode close to the light line[7], such as mode TE111-6, is strongly excited by beam and can be instrumented with high sensitivity.

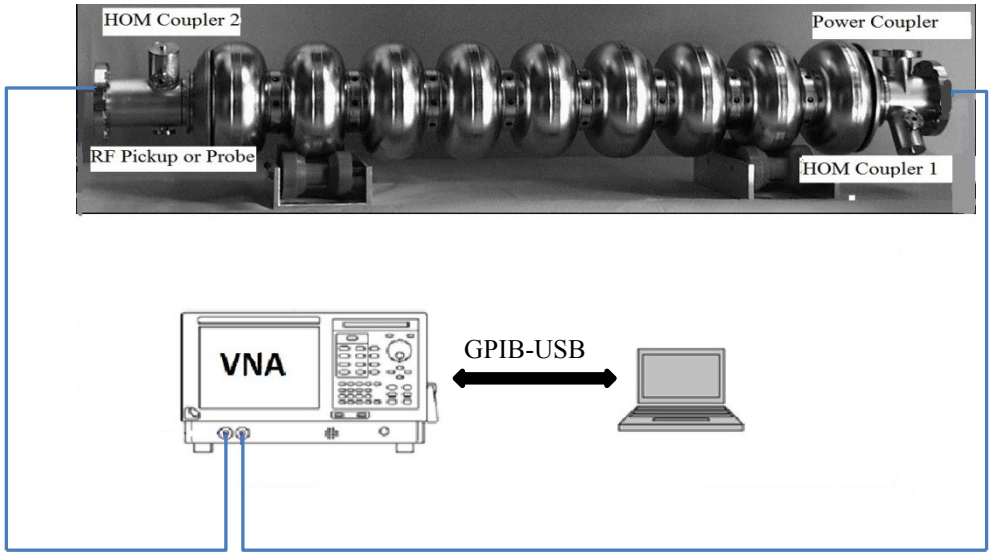

Figure 4.1 Measurement setup of a single 1.3 GHz cavity. The transmission S_{21} is measured between antennas installed in the two beam pipes. A VNA up to 20 GHz and a laptop running MATLAB are used for data acquisition.

[7] The phase velocity of the mode is equal to the speed of the light c and a straight line can be drawn as: $\omega(\phi) = \frac{c}{L_{cell}}\phi$, e.g. the line in Figure 3.5(a) and Figure 3.7. Therefore the mode is synchronized with the ultra-relativistic electron beam and is excited strongly.

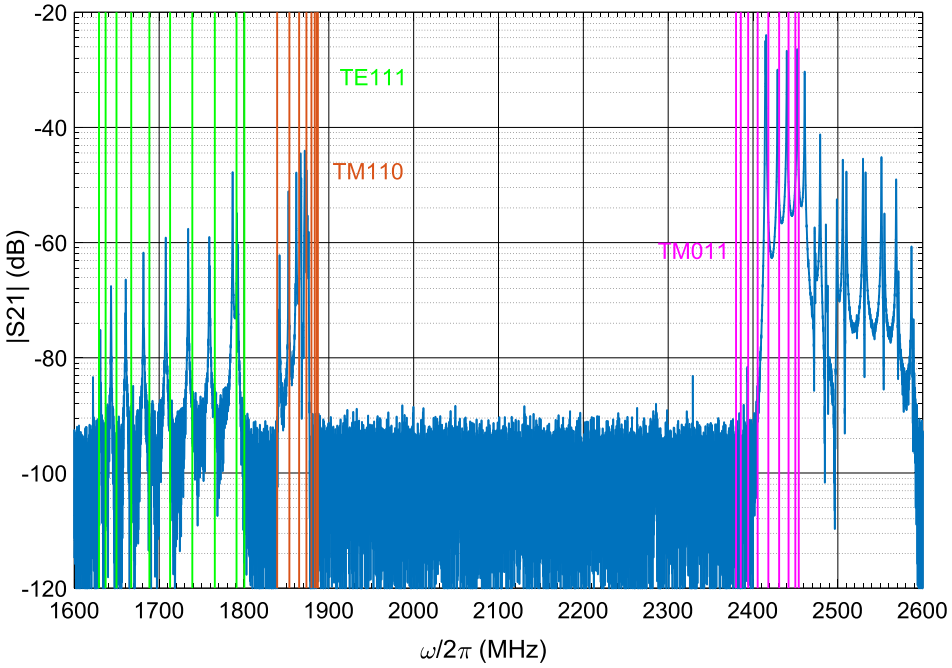

Figure 4.2 TE111, TM110 and TM011 bands of a TESLA cavity. The first two bands are dipole bands, and the last one is the first higher order monopole band. The coloured vertical lines correspond to the simulation result in [35].

These bands occupy the frequency ranges approximately from 1620 to 1800 MHz, 1830 to 1890 MHz, and 2380 to 2450 MHz respectively. The modes in each band are well separated and can be identified with the help of simulation, which makes the instrumentation of one particular mode feasible. In the TE111 band, modes 6 and 7 show larger R/Q relative to others and therefore have the potential of giving a high sensitivity when used for beam position monitoring. Mode TE111-6 (~1.7 GHz) has been chosen for beam position monitoring. Modes TM011-8 and TM011-9 in the second monopole band also show larger R/Q and are used for beam phase monitoring as it will be described in Chapter 5.

In order to ensure that the HOMs have been well damped, the external quality factors are extracted from the transmission spectra between the two HOM couplers when the cavities were tuned at 1.8 K. A summary of the external quality factors for the cavities in the 5th cryomodule in FLASH and the injector cryomodule in the E-XFEL [47], [48] are shown in Figure 4.3. All modes with higher R/Q, which can be detrimental to the beam, are damped below 10^5 as required [49].

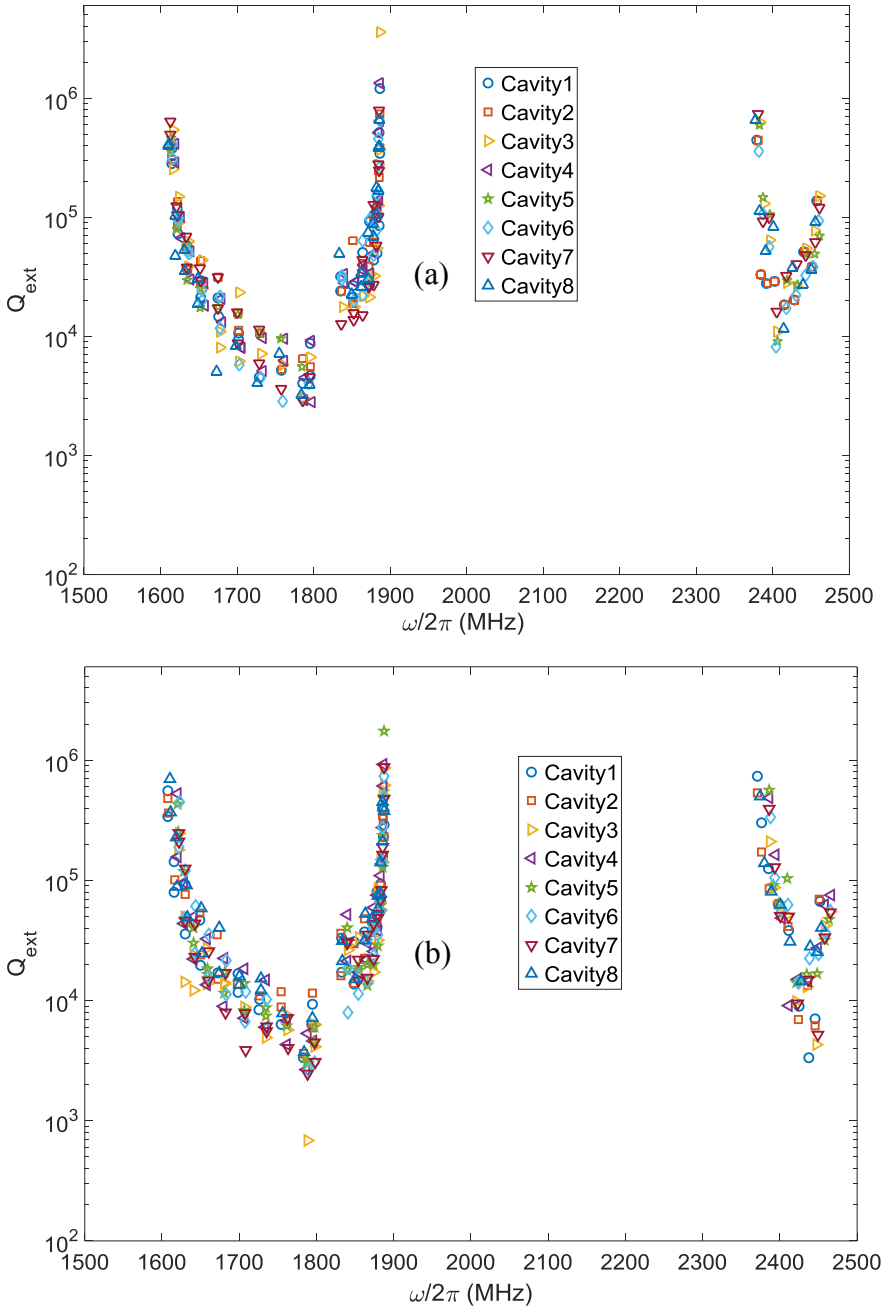

Figure 4.3 Quality factors of TE111, TM110 and TM011 modes for the 5th cryomodule in FLASH (a) and the injector cryomodule in the E-XFEL (b).

For each dipole mode, the two polarizations have different frequencies due to the influence of the couplers and the imperfection of the cavity itself. In this thesis, the polarization 1 is defined as the peak with lower frequency and the other peak as polarization 2. For the TE111-6 mode, the largest variations for polarizations 1 and 2 are 5 MHz and 7 MHz respectively among the cavities in the 5th cryomodule at FLASH and 10 MHz in injector module at the E-XFEL. The maximum difference

between the two polarizations is 0.3 MHz and the minimal is below 1 kHz for FLASH, while the maximum is 0.6 MHz and the minimum is 0.1 MHz for the E-XFEL. The difference between the average frequency of the TE111-6 mode at FLASH and the E-XFEL is ca. 4 MHz.

The maximum frequency variation from cavity to cavity for the TM011-8 mode is 5 MHz in the 5th cryomodule at FLASH and 14 MHz in the injector module at the E-XFEL. The variation for the TM011-9 mode is 5 MHz at FLASH and 15 MHz at the E-XFEL. The minimum and maximum mode frequencies are summarized in Table 4-1.

Table 4-1 Summary of frequency variations of the TE111-6, TM011-8 and TM011-9 modes. The data is from the cavity database [47], [48].

		TE111-6 Polarization 1	TE111-6 Polarization 2	TM011-8	TM011-9
FLASH	Min(MHz)	1700.719	1698.130	2449.731	2455.682
	Max(MHz)	1705.536	1705.536	2455.188	2461.127
E-XFEL	Min(MHz)	1698.015	1698.170	2445.412	2450.865
	Max(MHz)	1707.819	1708.475	2459.042	2459.042

The HOMBPM electronics for the 1.3 GHz cavities at FLASH has a narrow bandwidth of 20 MHz. The mode frequency variation is within the bandwidth of each HOMBPM channel. For the HOM electronics that is under development for the E-XFEL, the bandwidth will be approximately 150 MHz and 300 MHz for the TE111 and TM011 channel respectively, which are sufficiently wide to accommodate modes TE111-6 and TM011-8, 9.

4.1.2. Beam-excited HOM spectra

The beam-excited spectra were measured at the first cavity in the 6th cryomodule at FLASH with a Tektronix® spectrum analyser (RSA6114a) with a frequency range from 9 kHz to 14 GHz. The data was recorded at 1697.007 MHz with a frequency span of 1 MHz that contains the two polarizations of TE111-6 mode. The frequency

step is ca. 100 Hz. Modes TM011-7, 8, 9 were measured in the vicinity of 2452 MHz, with a frequency span of 30 MHz. The frequency step is 2.9 kHz. Figure 4.4 shows one example of beam-induced mode spectra. The frequencies of the polarizations 1 and 2 of TE111-6 are 1696.733 and 1697.006 MHz respectively. The difference between the two polarizations is 0.273 MHz. The frequencies of modes TM011-7, 8, 9 are 2439.135, 2449.736, 2456.964 MHz respectively. In Figure 4.4 (b), there are other peaks which might come from neighbouring cavities or may be just spurious modes. However, these peaks do not interfere with beam diagnostics and thus are not critical.

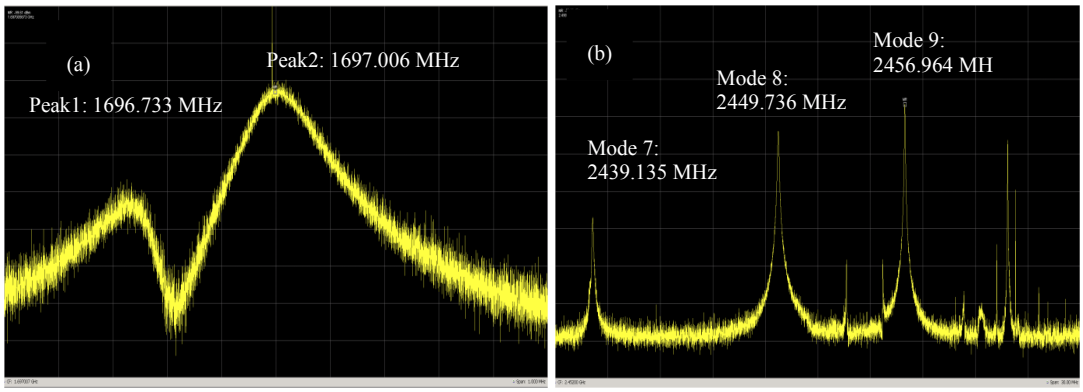

Figure 4.4 (a) The two polarizations of mode TE111-6 from the HOM coupler 1 of the 1st cavity of the 6th cryomodule at FLASH. The frequency difference between the two polarizations is 0.273 MHz. (b) Modes TM011-7, 8, 9 of the second monopole band.

Each HOM peak in the spectrum can be described by a Lorentzian function [50]. This is justified by considering a simple RLC circuit (see Appendix C). By using a global fitting technique from PeakFit®, it is possible to extract the mode frequencies and the quality factors based on equations 4.1 and 4.2:

$$y = \sum_i \frac{a_{0i}}{1 + \left(\frac{x - a_{1i}}{a_{2i}}\right)^2}, \qquad 4.1$$

where i is the peak index, a_{0i} the peak amplitude, a_{1i} the central frequency and a_{2i} the HWHM (Half Width at Half Maximum) of the peak. The quality factor is given by:

$$Q_i = \frac{a_{1i}}{2a_{2i}}. \qquad 4.2$$

The measurement was repeated several times within four months in order to investigate the stability of the dipole mode frequencies. The frequencies of the polarizations 1 and 2 in Figure 4.4 (a) are shown in Figure 4.5. Table 4-2 summaries the statistical information over time. The mean values of peaks 1 and 2 are 1696.710 and 1697.015 MHz respectively. Their standard deviations are 0.011 and 0.005 MHz respectively. The frequency variation will introduce amplitude modulations (see Appendix B). The implication of this will be discussed in Chapter 6. The measured signal strength for the TE111-6 was normally approximately -100 and -105 dBm for peaks 1 and 2 respectively with a beam charge of 0.5 nC, which is only several dBm above the noise floor (-110 dBm) of the system.

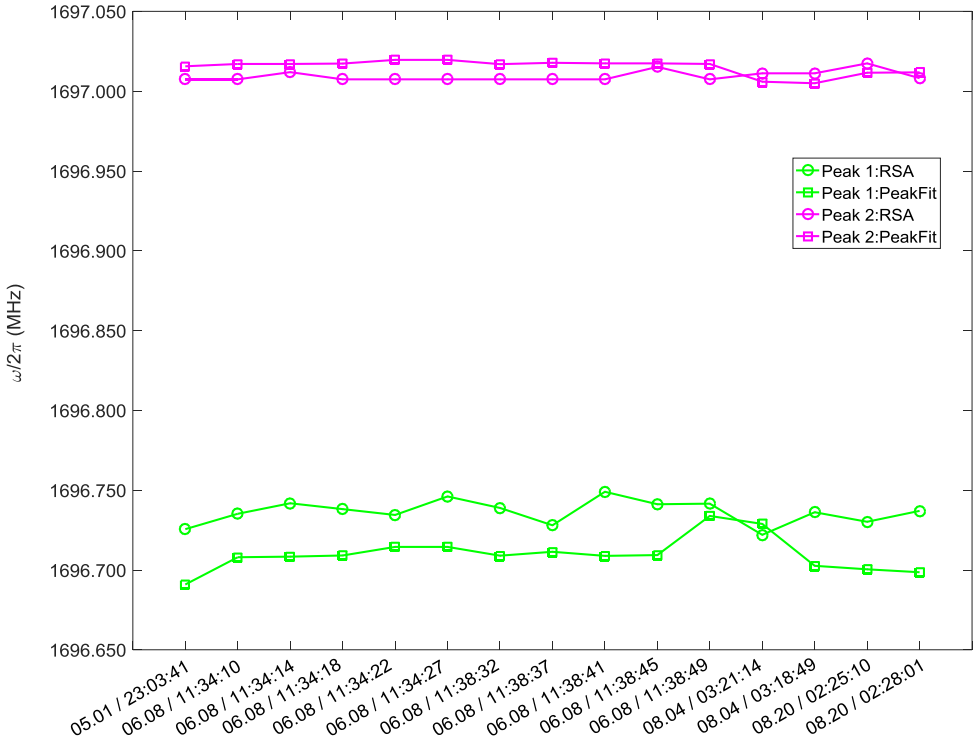

Figure 4.5 Frequency of the two polarizations of dipole mode TE111-6 over time measured from the HOM coupler 1 at the 1st cavity of the 6th cryomodule at FLASH. RSA refers to the measurement with a real time spectrum analyser. PeakFit indicates that the frequencies are obtained by fitting.

Table 4-2 Statistics of the TE111-6 frequency over time based on PeakFit results (see Figure 4.5).

Peak	Average Frequency (MHz)	Standard deviation (MHz)	Relative Error
1	1696.710	0.011	0.0006%
2	1697.015	0.005	0.0003%

The average quality factor obtained is approximately 20,000.

The frequency variation of modes TM011-7, 8, 9 is shown in Figure 4.6 and summarized in Table 4-3. The mean values of modes TM011-7, 8, 9 are 2439.132, 2449.737 and 2456.967 MHz respectively. The corresponding standard deviations are 0.002, 0.001 and 0.000 MHz respectively. As it will be shown in Chapter 5, the frequency variation in the range of kHz has very small impact on the resolution of beam phase determination. The measured signal strength for the modes TM011-8 or 9 was approximately –80 dBm for a beam charge of 0.5 nC, which is a few tens of dBm above the noise floor (-110 dBm) of the system.

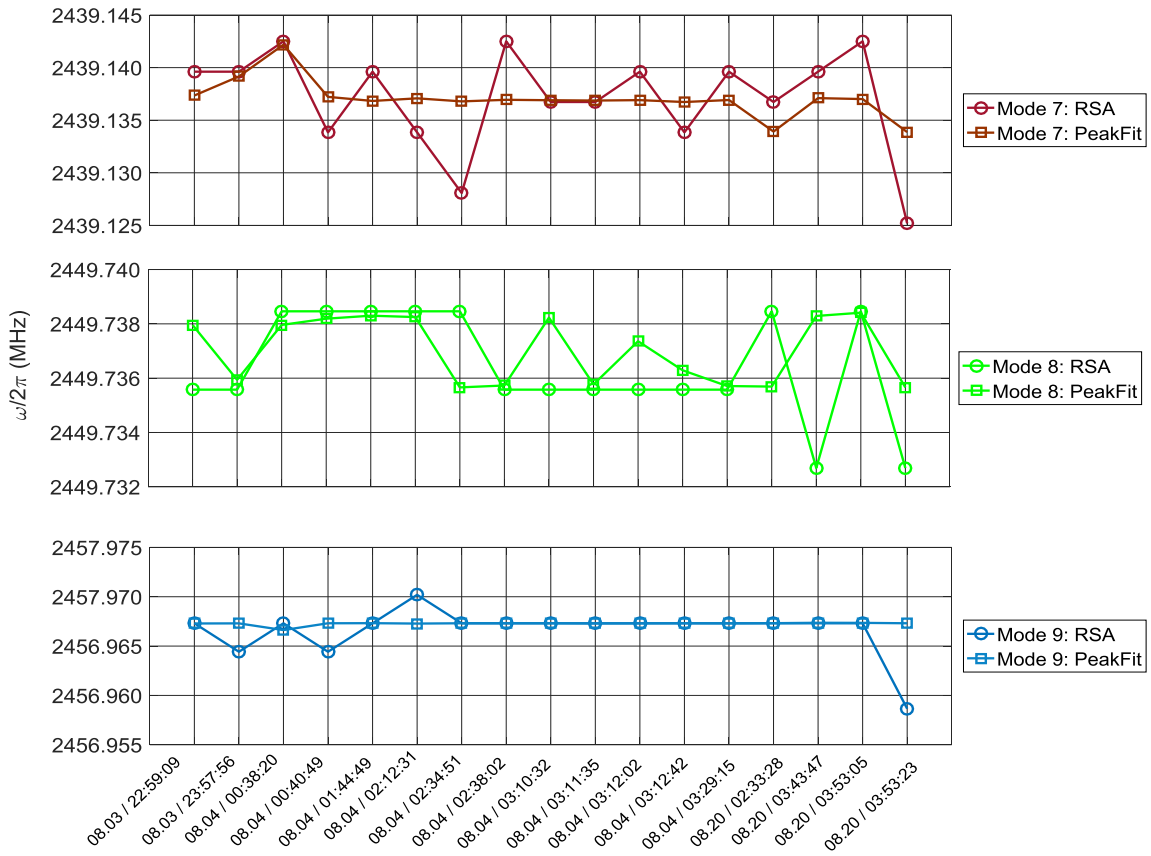

Figure 4.6 Frequencies of monopole modes TM011-7, 8, 9 over time at HOM coupler 1 of the 1st cavity in the 6th cryomodule at FLASH. RSA refers to the measurement done with a real time spectrum analyser. PeakFit indicates that the frequencies are obtained by fitting.

Table 4-3 Statistics of the TM011-7, 8, 9 frequencies over time based on PeakFit results (see Figure 4.6).

Mode	Average Frequency (MHz)	Standard deviation (MHz)	Relative Error
7	2439.132	0.002	0.00008%
8	2449.737	0.001	0.00004%
9	2456.967	0.000	0.00000%

Modes TM011-7, 8 show on average quality factors of approximately 25,000, while mode TM011-9 has 60,000.

In summary, the mode frequency variation was investigated from cavity to cavity in the 5th cryomodule at FLASH and in the injector module at the E-XFEL. The variations of frequencies are mainly due to the shape variation from cavity to cavity during the cavity fabrication and tuning process. The ten MHz variation from cavity to cavity of the mode TE111-6 is within the bandwidth of the HOM electronics[8]. The HOM electronics at the E-XFEL has sufficient bandwidth (hundred MHz) to accommodate these variations. For the same cavity, the frequencies of the beam-excited modes TE111-6 and TM011-7, 8, 9 showed a variation of a few kHz. This is because of the dynamic environment that the cavity is situated in and, the cavity shape being slightly deformed due to various processes (such as Lorentz force detuning, microphonic and the tuning forces applied to compensate the frequency change for the accelerating mode). As it will be shown in Chapters 5 and 6, these frequency variations have little impact on beam instrumentation.

4.2. HOM Spectra of Third Harmonic Cavities

As a preparation for the development of HOMBPMs for the third harmonic cavities at the E-XFEL, the HOM spectra were measured. There are eight 3.9 GHz cavities in the module (named AH1) at the E-XFEL compared to four at FLASH. Doubling the number of cavities complicates the higher order mode spectra significantly. Following the motivation of the HOMBPM for 3.9 GHz cavities at FLASH [7], the band of spectra that has the strongest beam position dependence needs to be identified. The HOM spectra for the FLASH third harmonic module are reported in [52]. The measurements for the E-XFEL 3.9 GHz cavities are summarized in [53].

Each cavity for the E-XFEL went through several tests after fabrication: measurement of the fundamental 3.9 GHz mode, tuning of the HOM couplers, vertical test etc.[54]. In the course of cavity tests, I have measured the S_{21} of single cavities and of the coupled cavities at 1.8 K and 293 K. These measurements serve as a database for the current HOMBPM development and its future use.

[8] The bandwidth of the electronics at FLASH is 20 MHz [51]

4.2.1. Single cavity measurements at 293 K

The measurement setup is similar to the one for the 1.3 GHz cavity (section 4.1.1). It contains three parts: the device under test, which is one single or several coupled cavities, a vector network analyser (VNA) and a laptop to control the instrument. A picture of the measurement setup for a single cavity is shown in Figure 4.7.

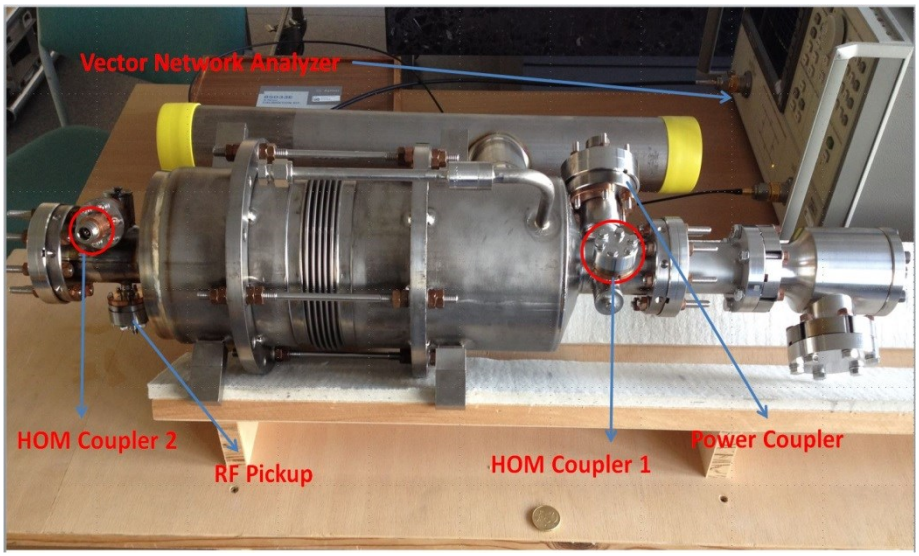

Figure 4.7 Measurement setup of a single 3.9 GHz cavity. The transmission S_{21} from one HOM coupler to the other is measured. A laptop running MATLAB is used for data acquisition. A VNA up to 20 GHz is used to perform the transmission measurements. The IF bandwidth for the VNA is chosen as 3 kHz for the 1st and the 2nd dipole band and 300 Hz for the 5th dipole band.

The transmission S_{21} from one HOM coupler to the other is measured. A laptop running MATLAB® is used for data acquisition. The measurements were carried out with a VNA (HP8720c) at a step of: 5 kHz for the first and second dipole bands and 500 Hz for the 5th dipole band. The IF bandwidth of the VNA is 3 kHz for the 1st and the 2nd dipole band and 300 Hz for the 5th dipole band.

The cavities installed in the AH1 module are named, in the beam direction, as follows: 3HZ010, 3HZ005, 3HZ012, 3HZ013, 3HZ008, 3HZ007, 3HZ004 and 3HZ011. All cavities have been measured at 293 K in vacuum state except 3HZ007. Only one cavity (3HZ010) was cooled to 1.8 K. The measured transmission spectra of cavity 3HZ010 at 1.8 K and at 293 K are compared in Figure 4.8. The vertical

dashed lines are the mode frequencies from a simulation of a single cavity without couplers [7].

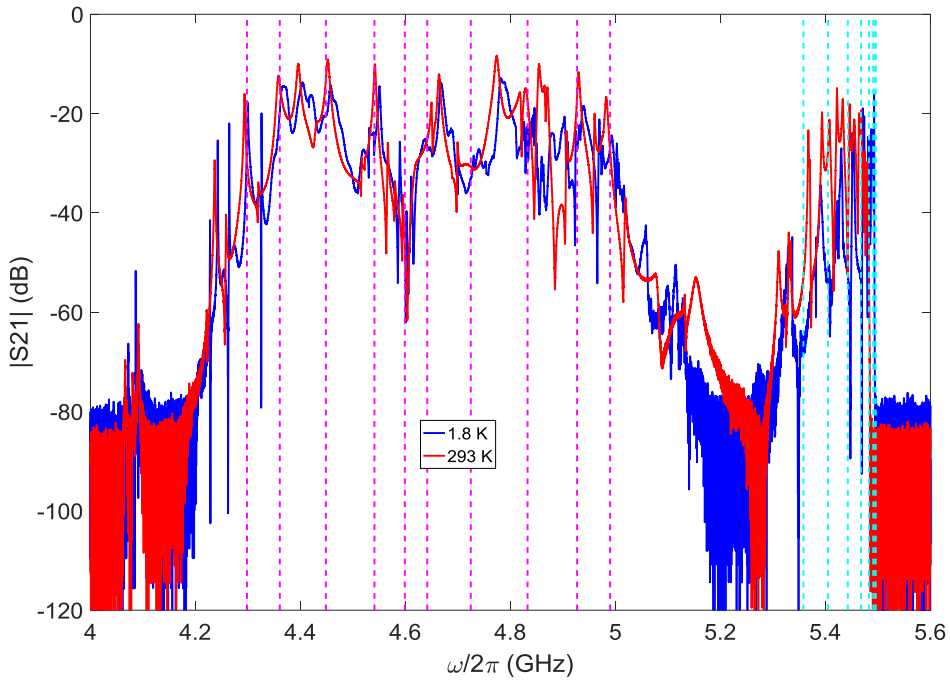

Figure 4.8 The 1st and 2nd dipole band of the cavity 3HZ010 at 1.8 K (blue), 293 K (red) in vacuum. The vertical dashed lines correspond to the modes in the 1st(magenta) and 2nd(cyan) dipole band from a simulation of single cavity [7].

The spectra of a single cavity are already more complicated than for the TESLA cavity. This is due to the fact that the iris radii are larger than one third of the iris radii for the TESLA cavity in order to better damp higher order modes. In principle, there are nine modes and eighteen peaks (two polarizations) in each band. However, as it can be observed in the spectra, there are more peaks present and it is difficult to identify the modes even with the help of simulations. Therefore a band of modes is used for beam position monitoring unlike the case for the 1.3 GHz cavities where only one mode is used.

The spectra measured for the tuned cavities at 293 K are shown in Figure 4.9. Two spare cavities (3HZ006 and 3HZ009) are also included. The spectra of the 1st and the 2nd dipole bands (Figure 4.9 (a)) of all cavities resemble each other except for cavity 3HZ010[9]. The second dipole band (~5.3 GHz to 5.5 GHz), used by the

[9] There was an issue with the fundamental power coupler, which was later fixed.

HOMBPM, is narrow, which makes the narrowband of electronics [55] (see Appendix F) feasible for beam position monitoring. The discrepancies in the spectra are mainly due to: 1. the geometry variation from cavity to cavity; 2. the different influence of the HOM and input couplers; 3. the different tuning of each cavity. The 5^{th} dipole band spectra for the various cavities are quite different from each other, as one can observe in Figure 4.9 (b). This is due to their higher sensitivity to the cavity geometry than for the 1^{st} and the 2^{nd} dipole bands.

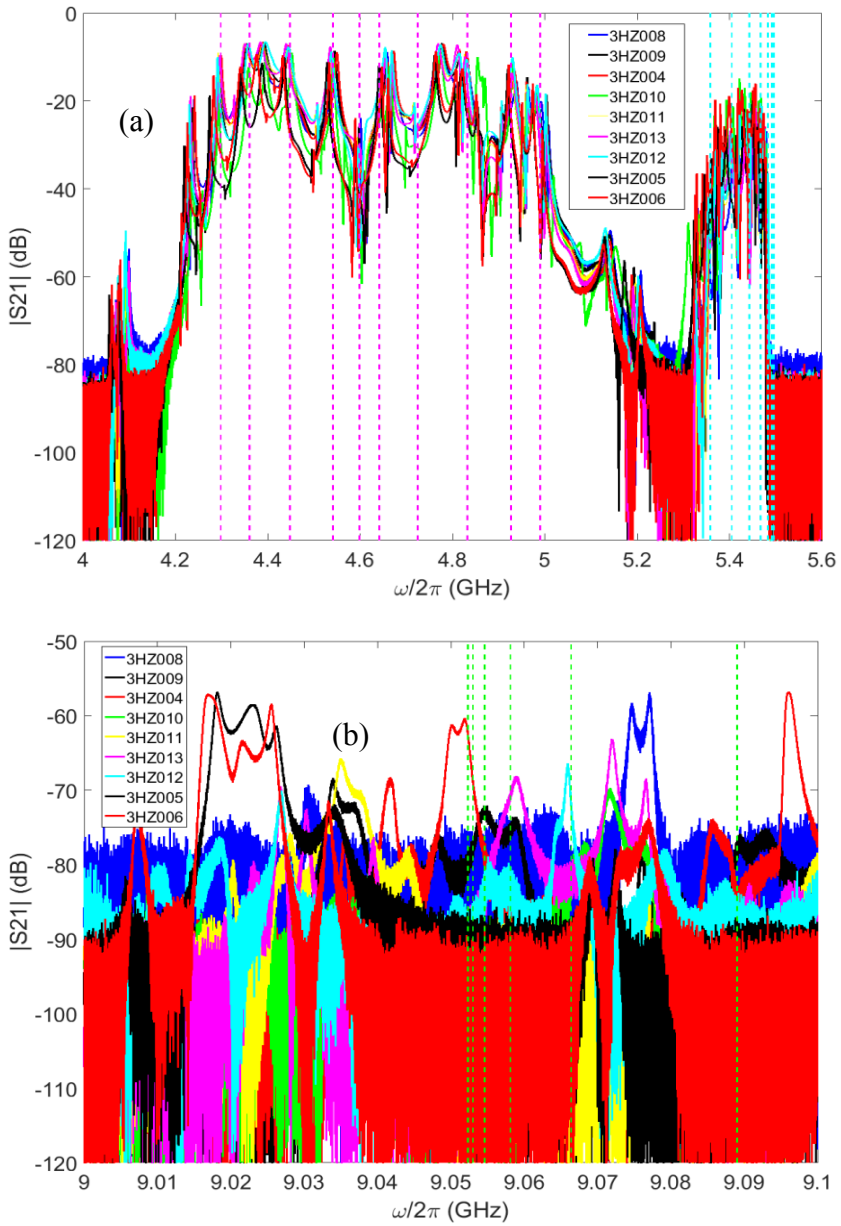

Figure 4.9 HOM spectra of 3.9 GHz cavities for the E-XFEL at 293 K. (a) The 1st and the 2nd dipole bands (b) The 5th dipole band. Note: cavities 3HZ006 and 3HZ009 are not used in the AH1 module. The vertical dashed lines correspond to modes in the 1st (magenta), 2nd (cyan) and 5th (green) dipole band from simulation of a single cavity [7].

Taking cavity 3HZ010 at 1.8 K as an example, the measured spectra and fitting results (based on equations 4.1 and 4.2) are shown in Figure 4.10. Each dipole band was fitted separately with the PeakFit program. Within each band, more than 18 peaks were found and it is difficult to account for their origin. It comes from the fact that these peaks tend to fit the shape of the spectrum which might give non-physical modes.

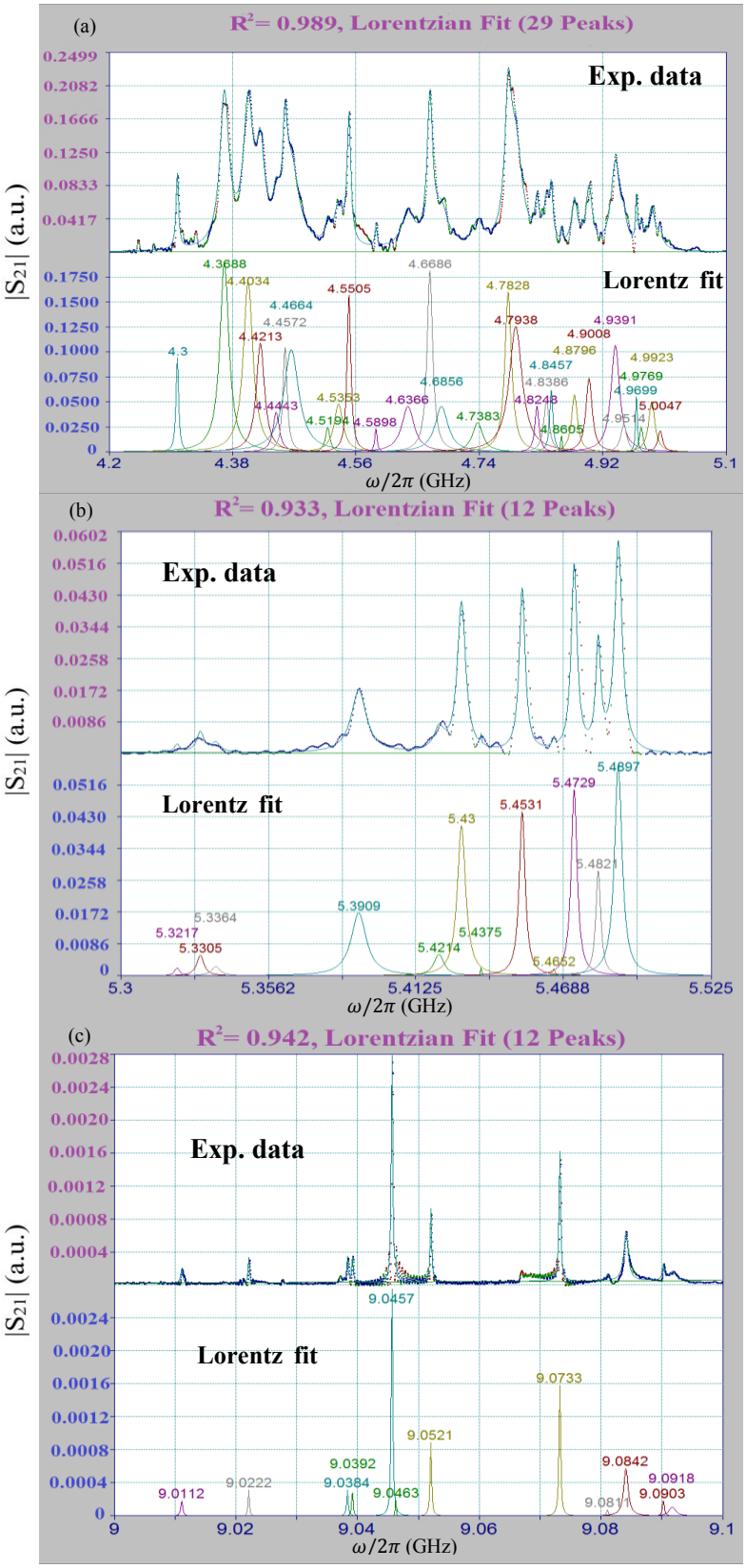

Figure 4.10 The 1st (a), 2nd (b) and 5th (c) dipole bands of cavity 3HZ010 at 1.8 K; Each plot shows the experimental data (exp. data) points and the peaks found by Lorentz fit.

The fitting results are summarized in Table 4-4. It can be observed that all the HOMs are damped to be below 30,000. The modes in the 5th dipole band present higher Q values due to the fact that they are trapped inside the cavity [52].

Table 4-4 Summary of peak frequencies and quality factors for cavity 3HZ010 obtained by fitting (see Figure 4.10).

1st dipole band		2nd dipole band		5th dipole band	
freq. (GHz)	Q	freq. (GHz)	Q	freq. (GHz)	Q
4.3001	4.80E+02	5.3216	1.06E+03	9.0112	1.24E+04
4.3688	1.37E+02	5.3305	7.90E+02	9.0222	1.77E+04
4.4033	1.32E+02	5.3364	6.35E+02	9.0384	1.49E+04
4.4213	1.53E+02	5.3908	3.84E+02	9.0392	1.81E+04
4.4443	2.00E+02	5.4214	5.75E+02	9.0457	1.63E+04
4.4572	3.07E+02	5.4300	7.10E+02	9.0463	2.89E+04
4.4664	8.40E+01	5.4374	7.50E+03	9.0521	1.53E+04
4.5194	2.92E+02	5.4531	1.01E+03	9.0733	1.38E+04
4.5353	1.45E+02	5.4651	2.06E+03	9.0812	1.47E+04
4.5505	3.46E+02	5.4729	1.01E+03	9.0842	5.15E+03
4.5898	6.00E+02	5.4820	1.23E+03	9.0903	1.34E+04
4.6367	1.08E+02	5.4897	7.85E+02	9.0918	3.40E+03
4.6686	2.40E+02				
4.6856	1.02E+02				
4.7384	1.31E+02				
4.7828	2.07E+02				
4.7938	1.04E+02				
4.8248	3.41E+02				
4.8386	2.54E+02				
4.8605	1.10E+03				
4.8796	2.35E+02				
4.9008	2.25E+02				
4.9391	1.63E+02				
4.9514	2.31E+02				
4.9699	8.95E+02				

The same analysis was performed for every cavity I have measured. The complete results can be found in [53].

4.2.2. Coupled cavities measurements at 293 K and 1.8 K

Transmission measurements were made at the string of eight cavities before it was placed into the cryomodule and after it was installed at the E-XFEL injector.

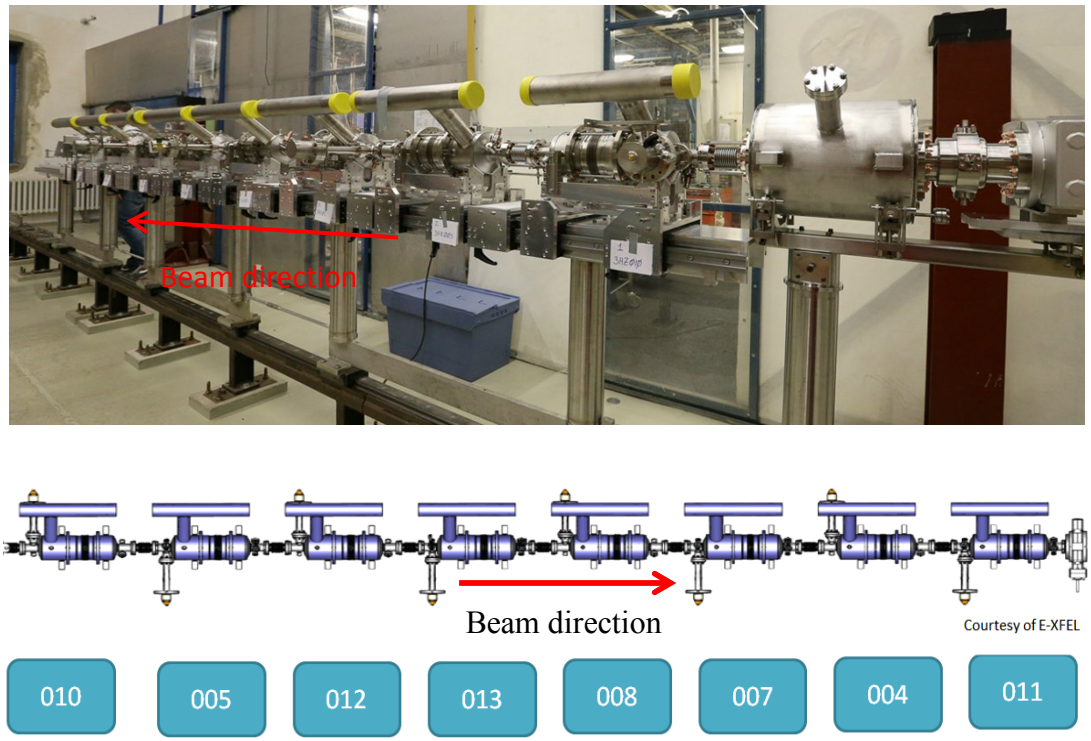

Figure 4.11 The string of coupled 3.9 GHz cavities before installation in the module. The cavities are filled with argon. The transmission spectra were measured from cavity 3HZ010 to 3HZ005, 3HZ012 and so on until 3HZ011.

Figure 4.11 shows the string of cavities ready to be installed into the cryomodule. The HOM coupler 1 and power coupler are always in the upstream with respect to the HOM coupler 2, which differs from the configuration at FLASH [7]. The other HOM couplers, the power coupler and RF pickup were left open. Measurements were performed from the HOM coupler 1 (upstream, in the beam direction) of the first cavity to the HOM coupler 2 of each cavity along the string of cavities. The 1st, 2nd and 5th dipole bands were measured.

Figure 4.12 shows a summary of the measurements at 293 K and in superconducting state. It can be observed that the spectrum gets more complicated due to the coupling between the cavities. In principle, each mode in a cavity splits into eight

modes if the string of cavities is viewed as a super-cavity structure. The bandpass structure becomes finer and finer as more cavities are coupled. In addition, there are also beam pipe modes and coupler modes as observed in simulations [56].

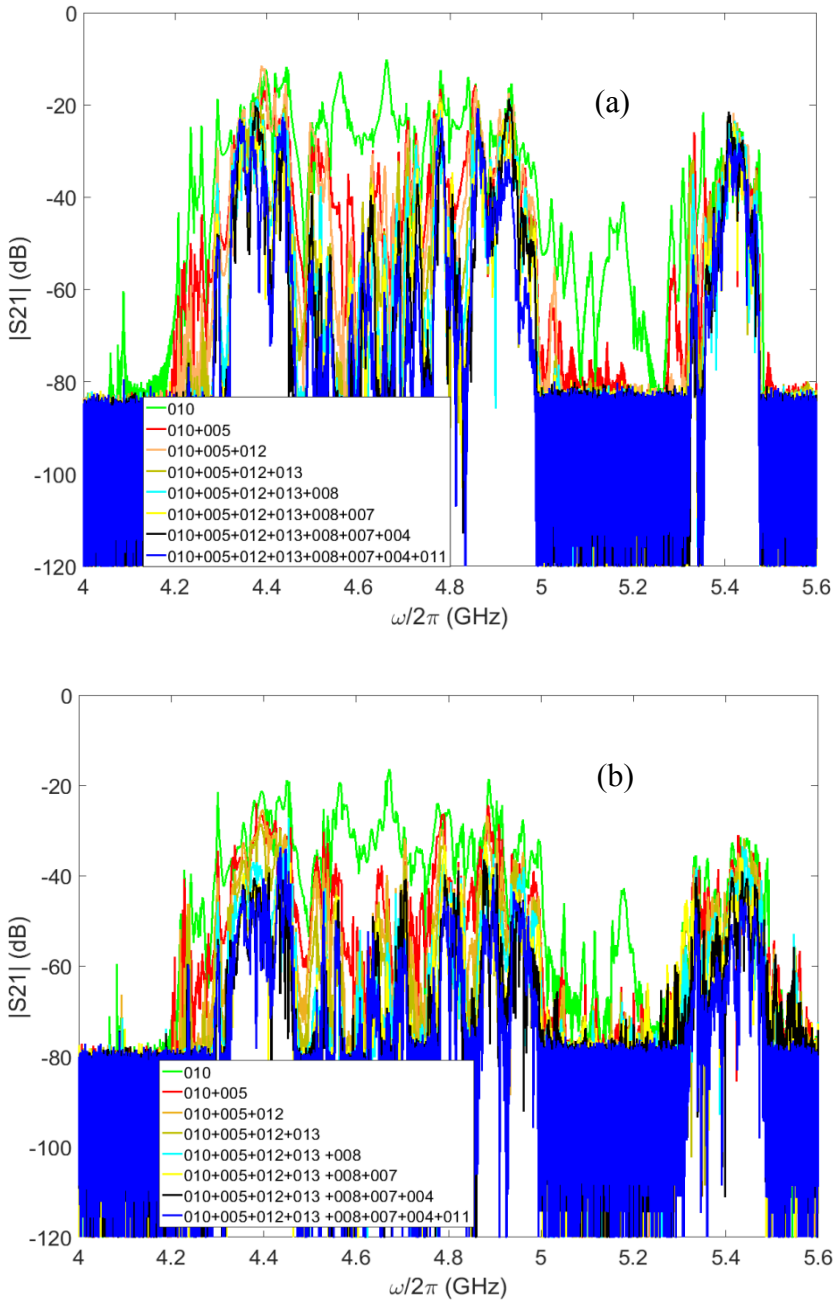

Figure 4.12 Transmission spectra for a string of cavities (a) at 293 K (b) at 1.8 K; Digits 010 means transmission through cavity 3HZ010 when it is coupled with other cavities. 010+005 means the transmission through cavity 3HZ010 and cavity 3HZ005 and so on.

The measurements were repeated after the third harmonic module was installed into the E-XFEL injector. The cryomodule was in superconducting state and the cavities were tuned. When the transmission was measured for a certain pair of HOM couplers, the rest of the HOM couplers were terminated with 50 Ω loads. By comparing Figure 4.12 (a) and (b), it is easily observed that the noise floor is several dB higher at 1.8 K than at 293 K. This is mostly due to the longer cables used. For comparison, the transmission from the first to the last cavity is shown in Figure 4.13 at 293 and 1.8 K. As the module is cooled, there is a shift of a few tens of MHz.

The transmitted power level at 1.8 K is approximately 20 dB less than at 293 K. This is due to the fact that the channels were terminated during the measurements at 1.8 K, while they were left open at 293 K in Figure 4.12 (a). The cavity wall losses at 293 K (normal conducting) also contribute to the difference.

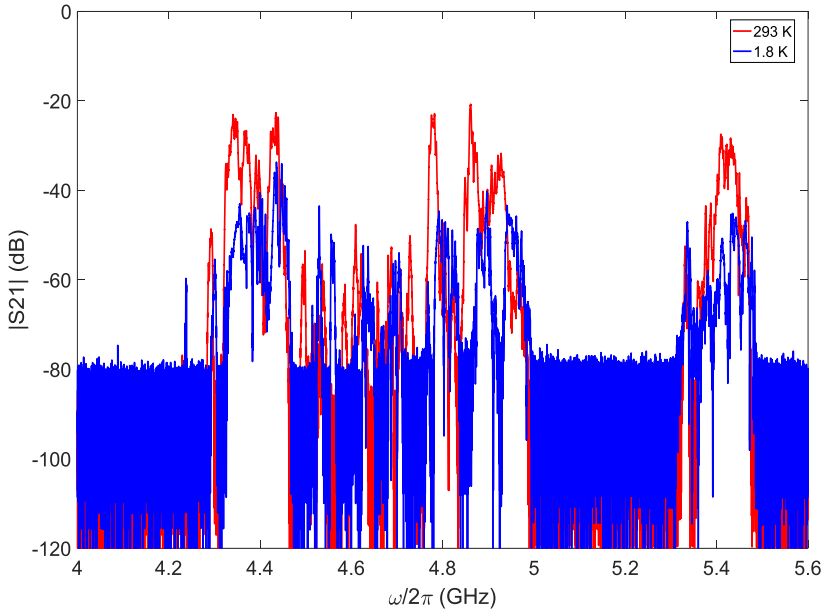

Figure 4.13 Comparison of full module transmission between 293 K (red) and 1.8 K (blue); as for the single cavity case, there is a few tens of MHz frequency shift. The transmitted power is approximately 20 dB less at 1.8 K than at 293 K.

The transmission measurements of 3.9 GHz cavities presented above, together with the experience at FLASH, provide the basis for the instrumentation of the HOMs at the E-XFEL. The results will facilitate future beam-based HOM electronics tests and its development.

In summary, one TESLA cavity was measured to reveal the HOM modal structure. The modes within the band used for beam instrumentation can be identified with the help of eigenmode simulations. The beam-induced spectra are monitored at FLASH to investigate the stability of the mode frequencies. The variation is within a few kHz over months.

HOM measurements have been carried out also for single and coupled 3.9 GHz cavities for the E-XFEL. The spectra become more complicated when more cavities are coupled together. The measurements were mainly made for the first and the second dipole bands. The frequency range of 9-9.1 GHz shows negligible transmission since the modes in this range are trapped in a cavity [57]. These measurements can be used as a reference for future tuning of the HOM electronics and also provide a reference for the beam-induced modes.

In next chapter, beam phase measurements based on the modes from the TM011 band of a TESLA cavity will be presented. The stability study of these modes provides a solid basis for the monitor development.

Chapter 5 - HOM-based Beam Phase Monitoring

The accelerating RF fields in the TESLA cavities must be controlled to a precise level as variations in the field can result in beam energy spread and arrival time jitter. This in turn can lead to a reduction in the quality of the photon beam. Both the amplitude and phase of the RF field have to be monitored and controlled. This chapter investigates a new type of beam phase determination technique based on beam-excited HOMs in the TESLA cavities, which differs from the standard scheme used by the LLRF (Low Level Radio Frequency) system [58] at the E-XFEL and FLASH. All the measurements in this chapter are made at the injector part of the E-XFEL unless otherwise specified.

The LLRF at the E-XFEL is briefly introduced in section 5.1. A simulation based on a coupled circuit is used to facilitate the development of HOM-based beam phase monitor in section 5.2. Phase measurements are presented in section 5.3. A summary and a brief description of the prototype electronics end the chapter.

5.1. Beam Phase Control for SRF Cavities

The RF fields along the 1.7 km linac of the E-XFEL must be controlled to a high precision in order to provide reproducible high quality photon beam pulses. At the E-XFEL and FLASH, the amplitude and the phase of the RF field are regulated by a sophisticated digital control system [2], [58], [59]. This locks the RF field of an accelerating cavity to the operating parameters. The stability of the amplitude and phase are required to be below 0.01% and 0.01° RMS respectively for both FLASH and the E-XFEL [59].

5.1.1. Introduction to the LLRF System at the E-XFEL

The linac of the E-XFEL consists of 768 superconducting TESLA 1.3 GHz cavities, grouped into 96 cryomodules, organized in 24 RF stations [60] over a length of ~ 1.7 km. Each RF station contains a 10 MW klystron which provides power to four cryomodules. Therefore the control of the beam phase is done via a vector sum [10]

of 32 cavities rather than the phase at each individual cavity [60]. The injector module is fed alone by one RF station. The control of the beam phase normally takes place at the low power level. The main components of the control system are detectors for RF field amplitude and phase, controller for feedback and feedforward, and actuators to control the incident wave to each cavity [58].

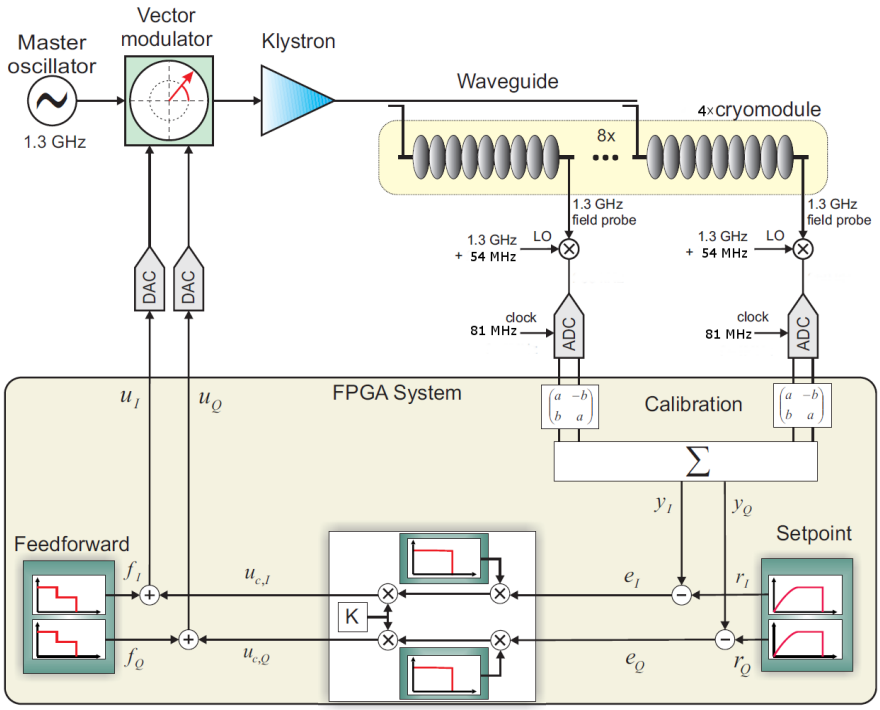

Figure 5.1 Schematic of LLRF control system [58]. It consists of a master oscillator, vector modulator, down converting and feedback units. (Courtesy of Christian Schmidt)

A schematic of the E-XFEL LLRF system is shown in Figure 5.1. A master oscillator provides timing signals. The vector modulator is then used to control the klystron. The output high power from the klystron is distributed into different cavities via a series of waveguides. The RF field in each cavity is detected by a field probe [13]. The down-converted signals from all cavities are digitized and summed to form the measured vector sum (y_I, y_Q). This sum is compared with the set operation values. The error between the set and the measured values is used as the controller input. The controller outputs are combined with the feedforward signal to

provide the drive inputs (u_I, u_Q) to the vector modulator. The whole system is implemented in a FPGA[10] chip.

Beam arrival monitor (BAM) and bunch compression monitor (BCM) are also employed to monitor the electron beam property to provide feedback information for accelerating field control. Particularly the beam timing from BAM is used for amplitude and the beam compression is used for phase control [61].

In addition to the regulation of RF field, the LLRF is also responsible for providing a highly stable RF reference along the tunnel. Other requirements on the system are due to its distributive and large scale nature [60].

5.1.2. Beam phase determination based on HOMs

In order to determine the beam phase, in principle, the beam-induced signal and the klystron signal have to be compared. For a TESLA cavity, the beam-excited accelerating mode (beam loading) is several orders of magnitude smaller than the one from the klystron. Therefore, a high dynamic range and resolution of the beam monitoring is required. Here I use a different approach which is able to measure the beam phase directly by comparing the beam-excited higher order modes and the accelerating mode. Normally, during accelerator operation, the power leakage through the HOM coupler of the 1.3 GHz mode and the power of the beam-excited mode in TM011 band are of the same order of magnitude. Therefore the requirement on the dynamic range can be easily met.

The proof of principle measurement of using HOMs for beam phase measurements was first mentioned in [6]. Each beam-induced mode carries the beam arrival information. By measuring the signal available at the HOM coupler, it is possible to convert the timing information into beam phase relative to the 1.3 GHz field. I use the following setup-independent procedure to determine the phase:

1. Decomposition of the signal

[10] Field-programmable gate array

The signal $x(t)$ from a HOM coupler contains the 1.3 GHz accelerating mode and the beam-excited HOMs. First the modes in the 2nd monopole band are filtered. The signal can be projected onto a sine term $x_{si}(t)$ and a cosine term $x_{ci}(t)$ according to:

$$x_{si}(t) = x(t)\sin(\omega_i t)\,, \tag{5.1}$$

$$x_{ci}(t) = x(t)\cos(\omega_i t)\,, \tag{5.2}$$

where ω_i is the angular frequency of each mode in the signal and has to be determined beforehand. The amplitude and phase of each mode i is carried by $x_{si}(t)$ and $x_{ci}(t)$. The method behind this is described in Appendix B. An example is shown in Figure 5.2 for $x(t)$, $x_{si}(t)$ and $x_{ci}(t)$, where $i = 0, 8, 9$. $i = 0$ is used for the fundamental 1.3 GHz mode, $i = 8$ and 9 the modes 8 and 9 in the TM011 band. The reason why only two modes are used will be discussed later.

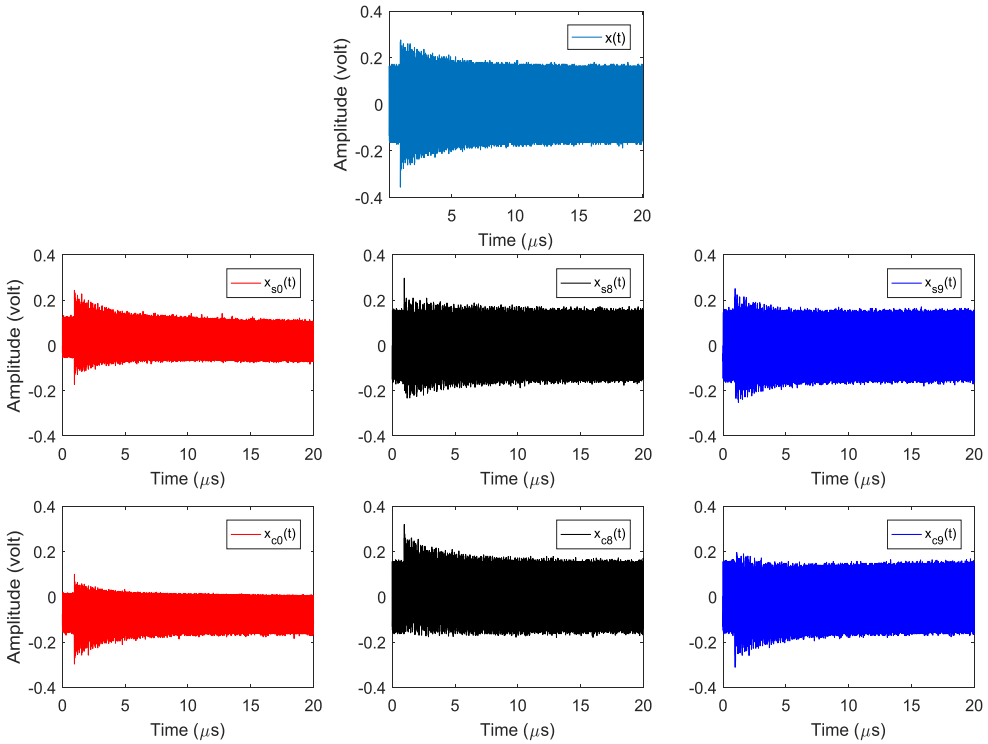

Figure 5.2 Filtered signal $x(t)$, and its components $x_{si}(t)$ and $x_{ci}(t)$ etc. $i = 0$ is used for the fundamental 1.3 GHz mode, $i = 8$ and 9 the modes 8 and 9 in the TM011 band.

2. Determination of phase for each mode

   After the operation in equations 5.1 and 5.2, the signal $x(t)$ is decomposed into DC and higher frequency components. This is essentially a digital down converting process.

   The phase of each mode inside the signal $x(t)$ is determined by equation 5.3. By integrating the signal, the DC part accumulates while the higher frequency part is filtered out:

$$\varphi_i = \arctan\left(\frac{\int x_{ci}(t)dt}{\int x_{si}(t)dt}\right). \qquad 5.3$$

   Taking into account the phase delays from components between the cavity and the measurement device, e.g. RF cables, the calibration phase φ_{ical} is determined during calibration and subtracted from φ_i for each mode i individually:

$$\delta\varphi_i = \varphi_i - \varphi_{ical}. \tag{5.4}$$

3. Determination of beam phase relative to the 1.3 GHz signal
   After calibration, the phase of each HOM is converted into time based on the frequency of each mode:

$$t_i = \frac{\delta\varphi_i}{\omega_i}. \tag{5.5}$$

   The average arrival time is defined as,

$$t_a = \sum_{i=1}^{N} t_i w_i, \tag{5.6}$$

   where N is the number of HOMs used in the calculation and w_i is the weight of mode i according to its power. The phase of the 1.3 GHz signal relative to t_a can be calculated with,

$$\varphi_{1.3} = (t_0 - t_a)\omega_0, \tag{5.7}$$

   where $\omega_0 = 2\pi \times 1.3 \times 10^9$ rad·s^{-1} is the angular frequency of the accelerating mode.

Based on steps 1-3, the beam phase relative to RF field can be calculated. The algorithm is implemented in a MATLAB script and is used in the following sections.

5.2. Simulation based on a Circuit Model

A single chain circuit model has been developed to study the dynamics of the second monopole band as described in Chapter 3. Each LC unit of the circuit is driven by a Gaussian pulse to simulate the electron beam. The time delay of two adjacent pulses is set to a half period of the 1.3 GHz mode, which is ~ 0.38 ns. This delay is introduced to simulate the propagation of the beam along the cavity. The normalized voltage across the capacitor can then be obtained by solving the circuit, as described in [41]. The circuit model is implemented in Simulink® and solved with a 5 ps step. The voltages across the first and ninth cells, denoted by HOM1 and HOM2 respectively, are superimposed with a 1.3 GHz signal. The associated algorithm for data processing as described in section 5.1.2 was developed based on this model.

In Figure 5.3, example spectra for HOM1 and HOM2 are shown. The vertical lines mark the eigenmode frequencies of a TESLA cavity obtained from MAFIA simulations [35]. There are nine modes excited corresponding to the nine eigenmodes of the 2nd monopole band. These modes are named mode 1, mode 2, up to mode 9 according to the frequencies in ascending order. Modes 8 and 9 are excited strongly due to their higher R/Q. Therefore, these two modes are used to determine the beam phase. In principle, nine modes can be used jointly to give the beam phase, but the improvement in terms of resolution is small, while the computation power required is tripled. Therefore, in later calculations, only modes 8 and 9 are used unless otherwise specified.

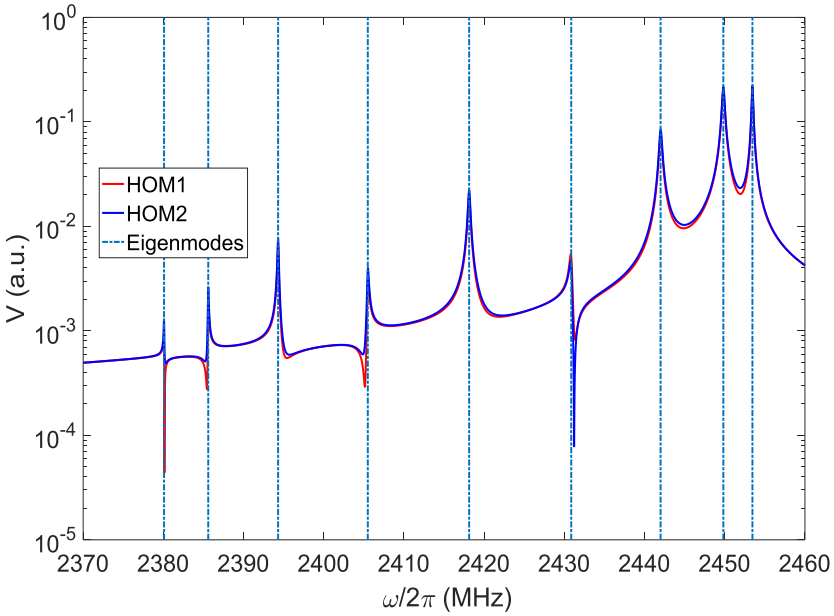

Figure 5.3 Spectra of waveforms HOM1 and HOM2 in the vicinity of 2.4 GHz. The vertical dashed lines are the eigenmode frequencies from MAFIA simulation of the TESLA cavity (Appendix G).

The phase of the 1.3 GHz signal is varied by ± 5° to simulate a phase change and can be calculated with the procedure described in section 5.1.2. The calculation is done independently for HOM1 and HOM2. The RMS of the phase difference between HOM1 and HOM2 can be used to evaluate the resolution of the beam phase determination. A factor of $\sqrt{2}/2$ is applied by assuming that the two channels are identical (see Appendix B). A variable level of AWGN[11] (Add White Gaussian Noise) is superimposed to the HOM1 and HOM2 to simulate realistic data. HOM1 and HOM2 are sampled at different frequencies to investigate the influence on the resolution. The result is summarized in Figure 5.4.

[11] Widely used to model the channel noise for communication system

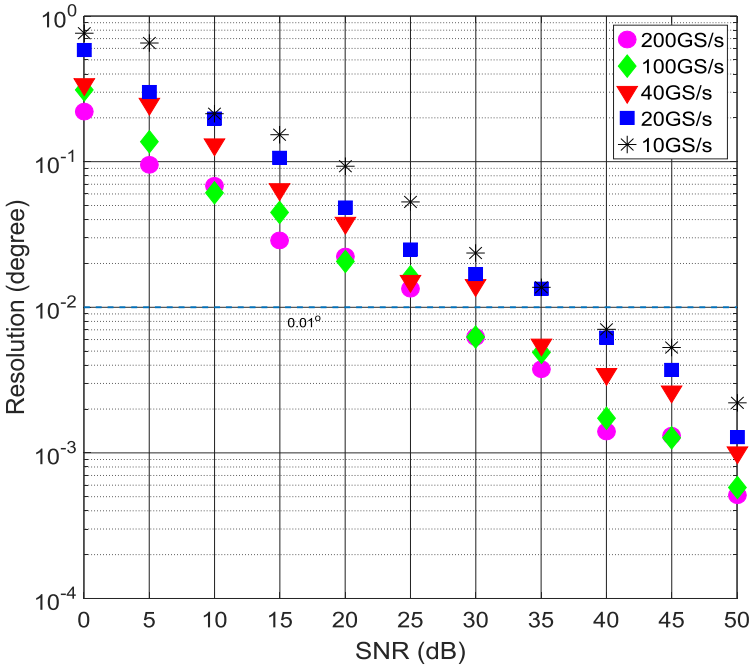

Figure 5.4 Resolution dependence on noise level and sampling frequency.

One can see that the resolution exhibits an exponential decay dependence on the SNR (Signal to Noise Ratio). A higher sampling frequency will generally give better resolution. Though high sampling rate digitizers with hundreds MS/s are rare to date in the market, usable system with 300 GS/s exists [62]. However, the resolution is ultimately limited by the SNR. The dependence of the resolution R on the SNR is obtained by fitting as (in logarithmic scale):

$$\ln(R) = B - 0.118 \times SNR, \tag{5.8}$$

where B is an intercept term that depends on the sampling frequency. For a sampling frequency of 20 GS/s, as used in later measurements, B is -0.542. Figure 5.5 shows the resolution dependence on the SNR in linear scale.

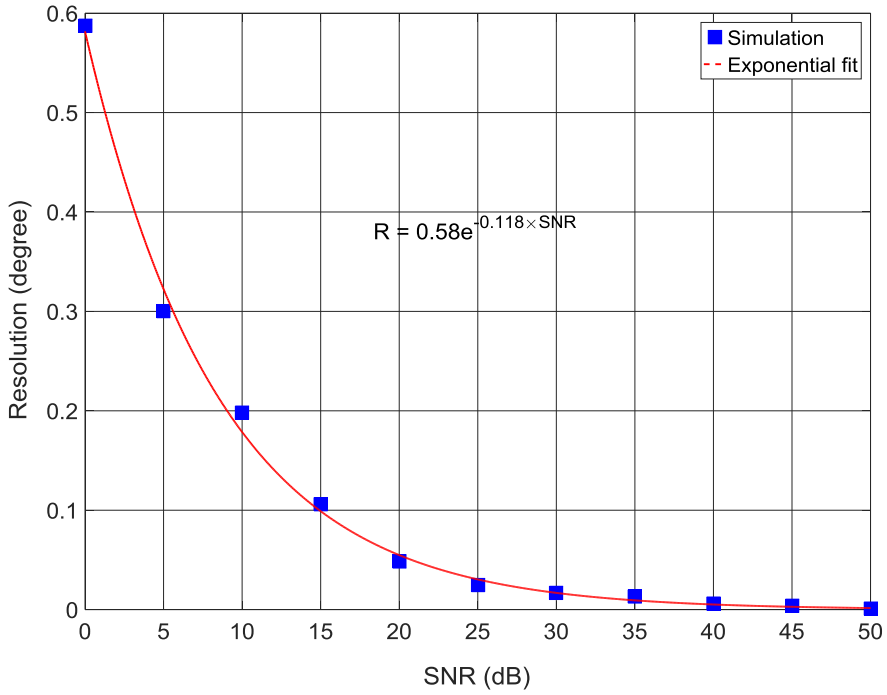

Figure 5.5 Resolution dependence on the SNR and exponential decay fitting for a sampling rate of 20 GS/s.

Based on the simulation result in Figure 5.4, in order to meet the phase requirement (0.01°) at the E-XFEL [63], the SNR should be higher than 35 dB.

As discussed in section 5.1.2, the frequency of each mode employed for beam phase determination has to be known beforehand and stored in a database. In order to investigate the resolution dependence on the frequency error, the mode frequencies are shifted with respect to the eigenmode frequencies from -1 to 1 MHz with a step of 100 kHz. The SNR is fixed at 20 dB, a value estimated from measurements as it will be discussed later. Figure 5.6 shows the resolution dependence on the mode frequency shift. The resolution is almost unaffected by the frequency shifts within this range.

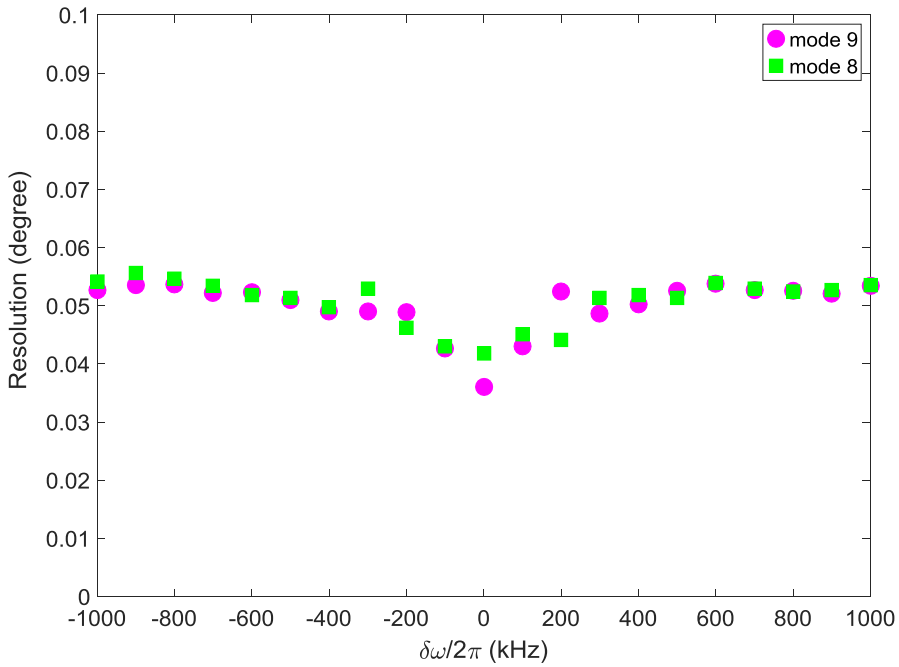

Figure 5.6 Resolution dependence on the frequency shifts of modes 8 and 9 with a step of 100 kHz.

This result was anticipated because when one mode frequency is shifted, the phase information is essentially determined from the other unaffected mode. If the frequencies of modes 8 and 9 are shifted independently, the result is summarized in Figure 5.7. The 3D plot shows that at the maximum 1 MHz shift, the resolution degrades by almost a factor of nine. Therefore at least one mode frequency should be determined accurately.

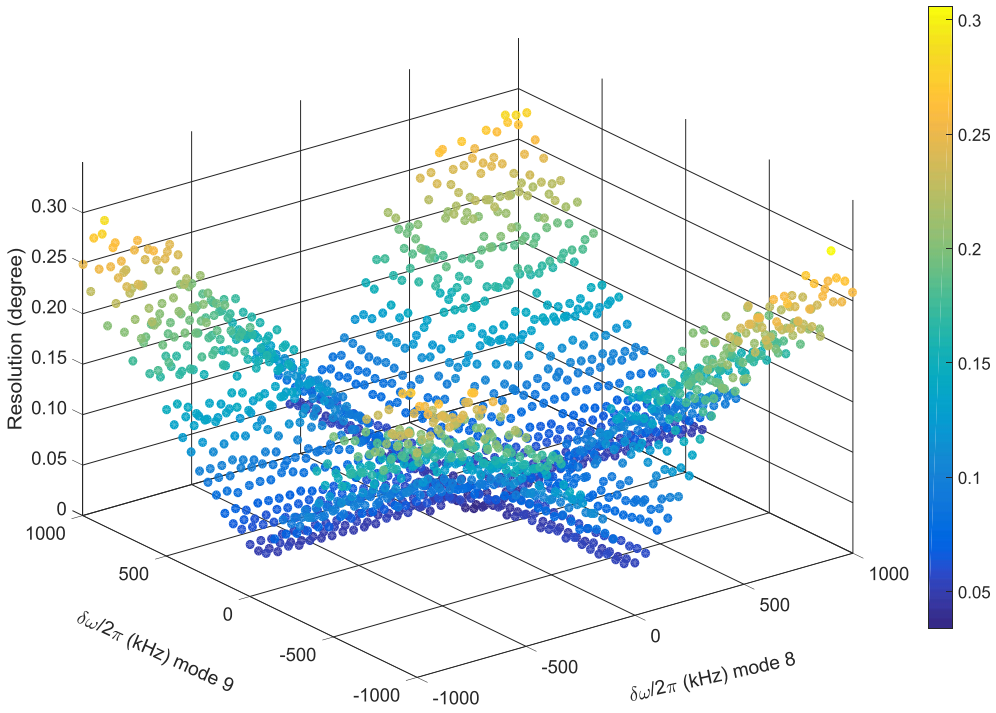

Figure 5.7 Resolution dependence on the frequency shift of modes 8 and 9 with a step of 50 kHz.

Up to now, I assumed that the signal power from HOM1 and HOM2 is balanced. In reality, however, due to the difference of the two physical channels, the power is unbalanced. Therefore, it is also necessary to scale the simulation data to gain insight into the system as it will be discussed later.

5.3. Beam Phase Measurements

Beam phase measurements were made at the E-XFEL injector module A1 and the 1st, 2nd, 5th and 6th accelerating modules at FLASH. The measurement setup is described in section 5.3.1. The estimation of noise and power levels is presented in section 5.3.2. The measurement results and comparison with simulation are shown in the last two sections.

5.3.1. Experimental setup

The setup consists of several RF bandpass filters, combiner/splitter, and a fast scope and is schematically shown in Figure 5.8.

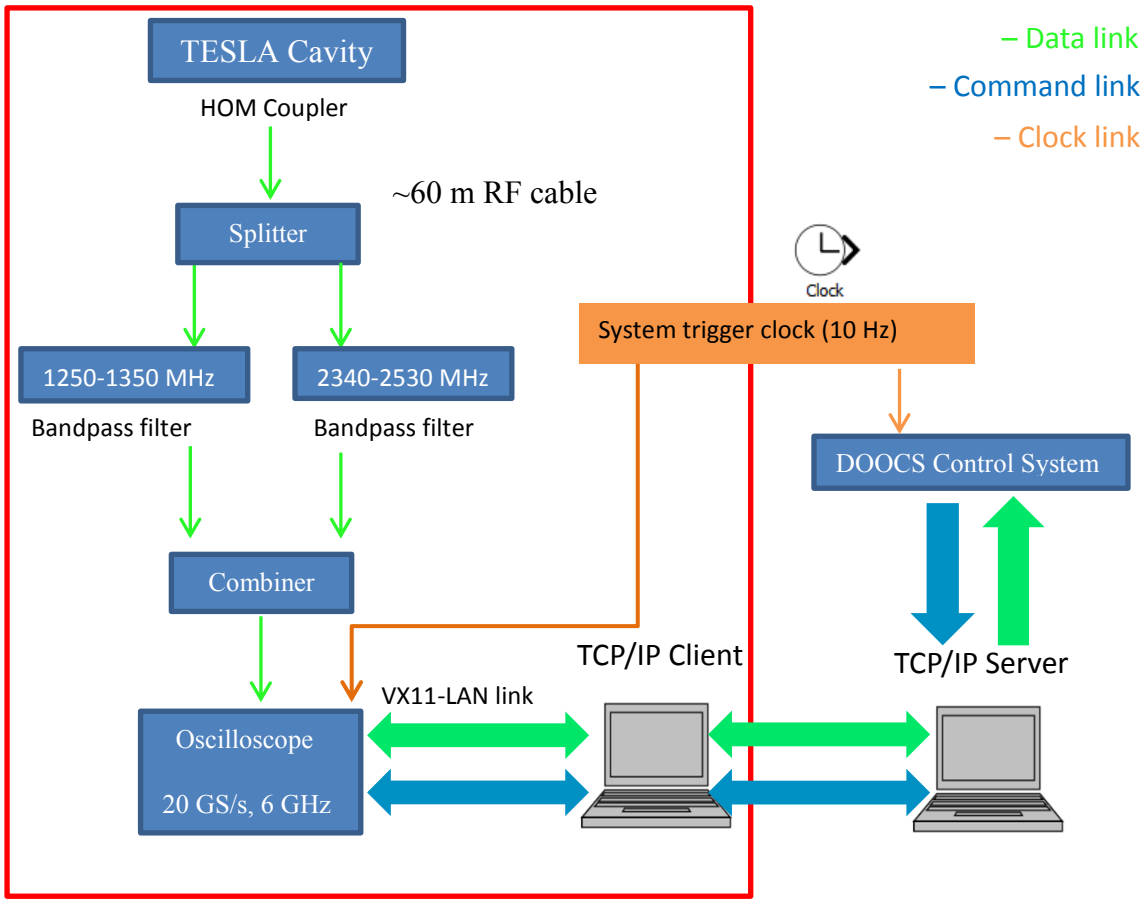

Figure 5.8 Block diagram of the beam phase measurements setup at FLASH and the E-XFEL. Two identical channels are used for the two HOM couplers of a cavity.

The two HOM couplers on each cavity deliver the signal for the two channels used for beam phase measurement. The signal from each HOM coupler is transmitted with a RF cable with length of ca. 60 m from the E-XFEL tunnel to the measurement rack. The signal is then split with a power splitter (5-2500 MHz). Each split signal is then filtered in parallel, one centered at approximately 1300 MHz with 100 MHz bandwidth and the other approximately 2435 MHz with 190 MHz bandwidth. The filtered signals are then combined again before they are fed into the Tektronix® oscilloscope TDS6604B (20 GS/s with 6 GHz bandwidth). The scope is triggered by an external 10 Hz trigger, which is synchronized with the data acquisition from the DOOCS control system [64]. The scope is remotely connected to a PC with VX11[12] protocol. One PC serves as a TCP/IP client and a second one as a server for collecting data from DOOCS. It should be pointed out

[12] VX11 is an industrial standard to provide instrument connectivity for remote control and data acquisition.

that the whole system is only partially synchronized with the electron beam because the synchronism is provided by the TCP/IP protocol and the command routing inside the network depends on the momentary traffic. It takes approximately 20 seconds to complete one triggered measurement.

As an example, a typical waveform and the associated spectrum are shown in Figure 5.9. The recorded waveform is 20 μs long and the frequency step in the spectrum is 50 kHz.

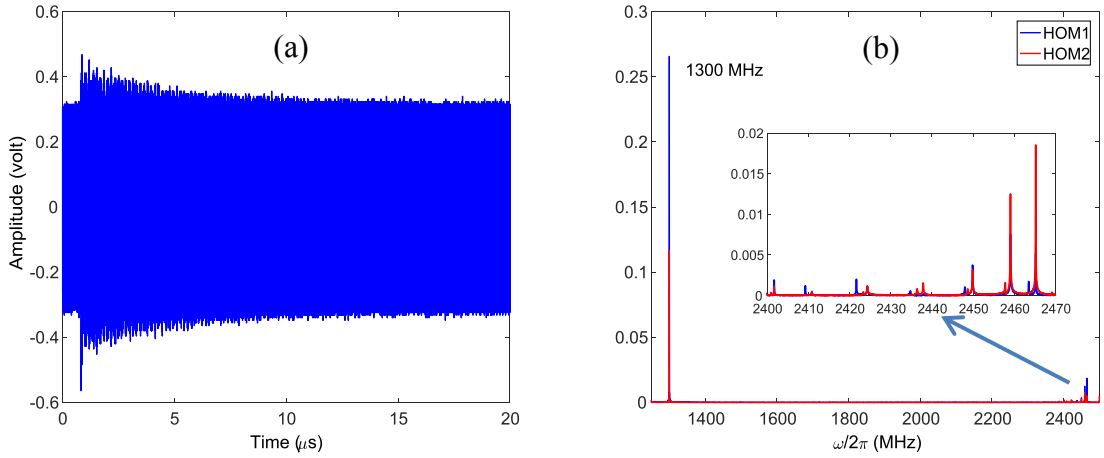

Figure 5.9 Measured waveforms (a) and spectra (b) of signals from HOM1 (blue) and HOM2 (red). The inset shows the spectra in the region of 2.4 GHz. The last two modes are excited strongly and are used for the phase determination.

The last two modes (mode 8 and mode 9) in the spectrum are excited strongest. The mode frequencies can be easily identified by overlapping the signals HOM1 and HOM2.

5.3.2. Non-parametric noise filtering and estimation

The resolution has a strong dependence on the noise level as shown by simulation study. Therefore, it is important to estimate the level in the measurements. For this purpose, I used the SVD[13] (see Appendix B) method. The signals were put in a data matrix *D* row wise. The SVD eigen components of matrix *D* can be found, which are the basis for signal decomposition.

[13] Singular Value Decomposition

The signals show larger singular values due to the correlation among signals while the noise exhibits smaller singular values due to the randomness. In this way, the signal and the noise can be separated. The separation is of course not perfect based on this method, but it provides a good estimation. The measurement is made at the 2nd cavity in the A1 module at the E-XFEL. Seventy five measurements were used to form the data matrix. The singular values of the data from HOM1 and HOM2 are shown in Figure 5.10.

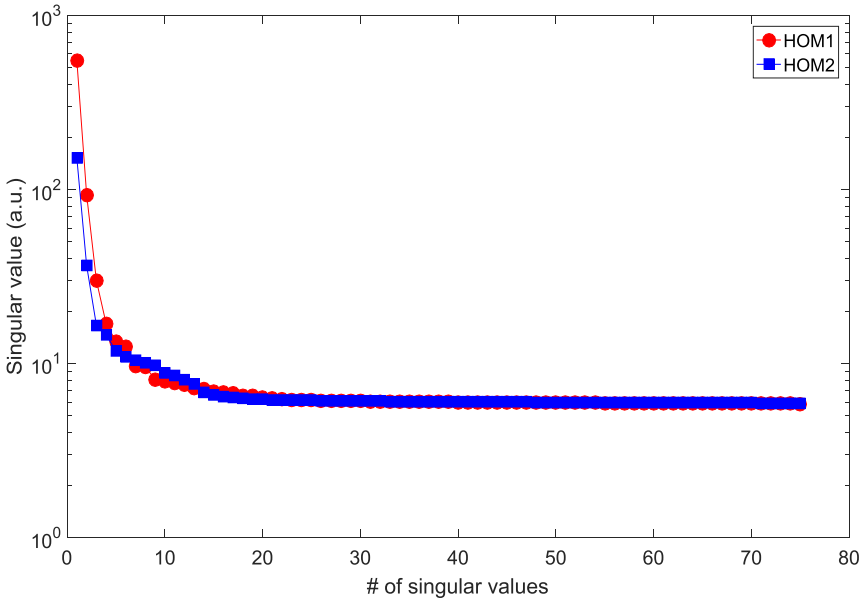

Figure 5.10 Singular values for HOM1 and HOM2. The values from both channels drop quickly to the same level.

In this calculation, the first 24 singular values are used in the reconstruction of the signal and the rest is regarded as noise. The noise waveform is reconstructed based on the remaining 51 singular values. The obtained noise waveform and its distribution are shown in Figure 5.11. The distribution justifies the AWG noise model applied in the simulation. The histogram is found to be a Gaussian distribution with mean value 0 and standard deviation 8 mV.

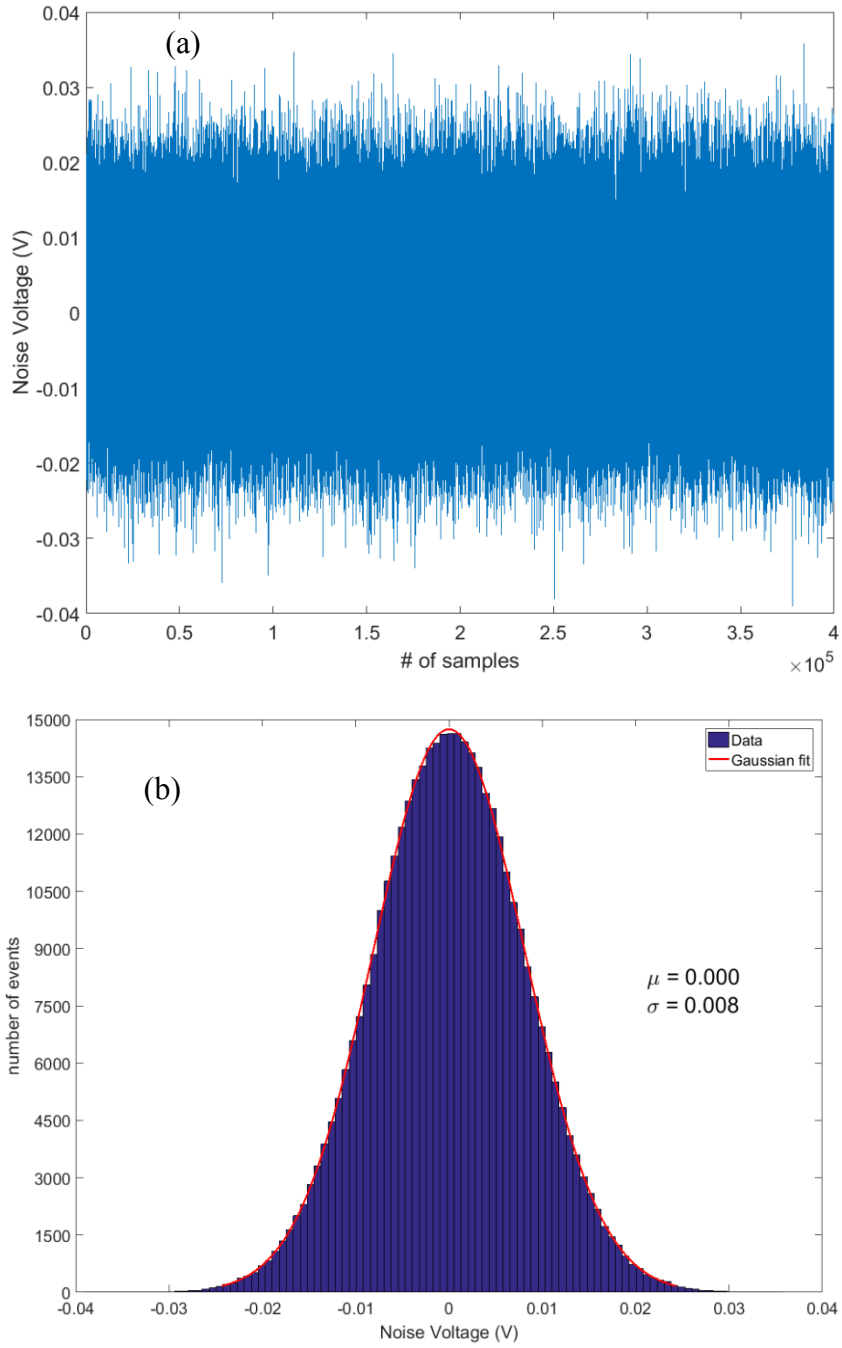

Figure 5.11 (a) Waveform of the reconstructed noise. (b) Histogram of the noise waveform with 400,000 samples. The mean μ is 0 and the standard deviation σ is 8 mV.

Based on this method, it is found that all measured cavities (# 2, 3, 5, 6 at A1 in the E-XFEL) exhibit the same level of noise (~8 mV RMS) and the variation from channel to channel is at the sub-millivolt level.

The SNR can be estimated from the separated signal and noise. With an accelerating gradient of 22 MV/m, the SNR for HOM1 at cavity 2 of A1 is approximately 22 dB in contrast to less than 10 dB for HOM2. The 10 dB difference is likely due to the power leakage difference from the two channels because the two HOM coupler notch filters are tuned differently. In order to compare the simulation and the measurements more accurately, the signals from the simulation are scaled according to this measured power difference.

5.3.3. Results

The frequency varies by a few MHz from cavity to cavity, which is more than the width of each mode (below 1 MHz) at FLASH. Therefore the mode frequency has to be determined for each cavity individually. Once the frequency of each mode is determined, it is kept constant in later calculation. The variation of the mode frequency is a few kHz over time as found in Chapter 4, which is acceptable for our application.

The experimental resolution dependence on the number of monopole modes used is shown in Figure 5.12.

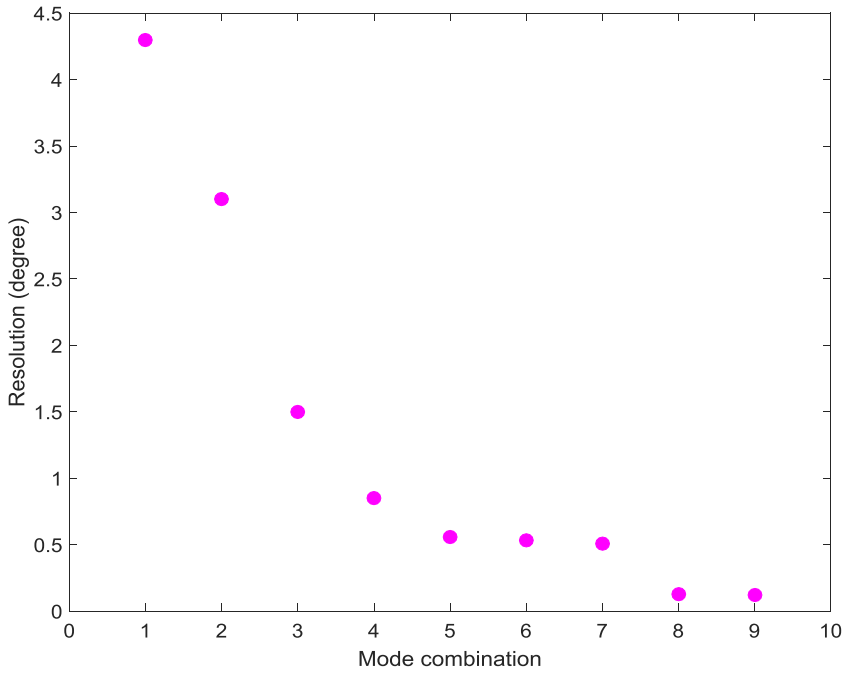

Figure 5.12 Resolution dependence on the number of modes used for phase determination at cavity 2 of injector module at the E-XFEL. On the horizontal axis, 1 means that mode 1 is used and 2 means that modes 1 and 2 are used etc.

When only mode 1 is used the resolution is above 4°. This is improved when more modes are included in the calculation. In the best case, when all nine modes are used, the resolution is 0.12°. This is due to the fact that mode 1 is excited weakly compared with other modes. In contrast, the resolution is 0.12° by solely using mode 9. Including more modes does not improve the resolution as long as mode 8 or 9 is used. It should be noted that due to the cavity geometry variation, mode 9 is not always stronger than mode 8. Therefore the best resolution cannot be guaranteed by using only one mode. In experiments, no other modes from this band are observed to be stronger than modes 8 and 9. Therefore, in later calculations both modes 8 and 9 are used for the phase determination.

The mode frequencies used for digital down conversion are shifted in a similar manner as for the simulation data. The resolution dependence on the frequency shift is presented in Figure 5.13.

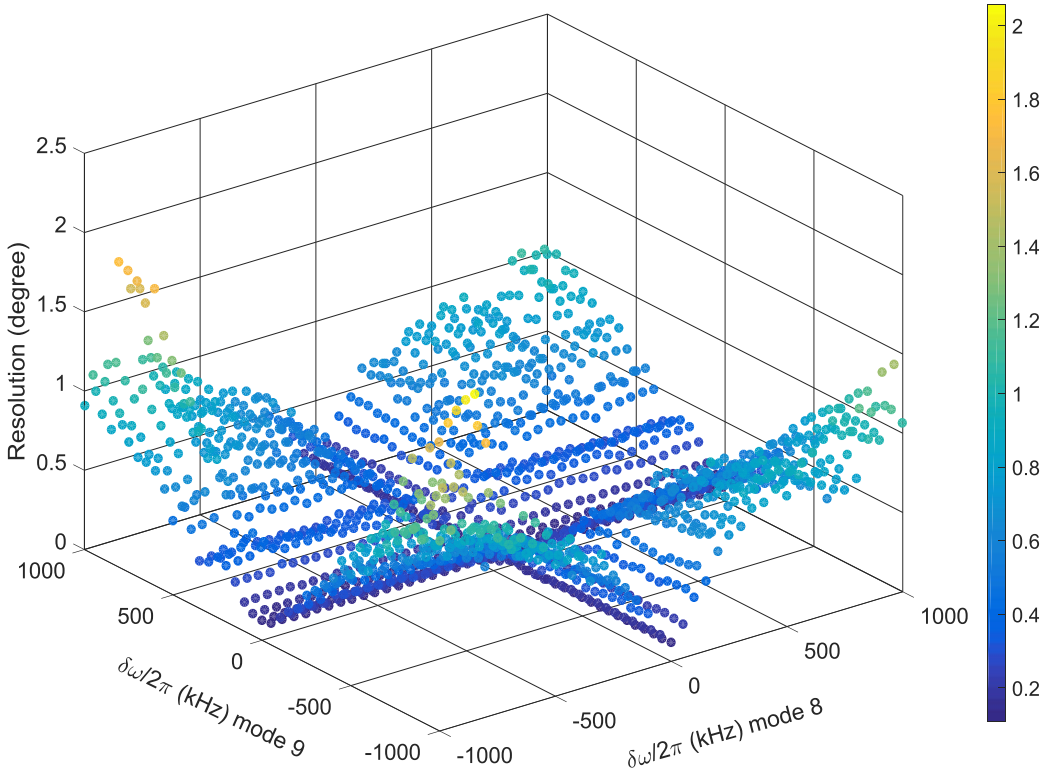

Figure 5.13 Resolution dependence on the frequency shifts of modes 8 and 9 with a step of 50 kHz.

A similar conclusion can be drawn as from the simulation data (Figure 5.7), namely that either mode 8 or 9 delivers a comparable resolution and that at least one mode needs to be determined accurately.

The beam charge was varied in order to investigate the resolution dependence on the charge. The monopole mode amplitude increases linearly as shown in Figure 5.14. Linear dependence is obtained in Figure 5.14 (b) as expected. The amplitude is calculated based on equations 5.1 and 5.2 (see Appendix B).

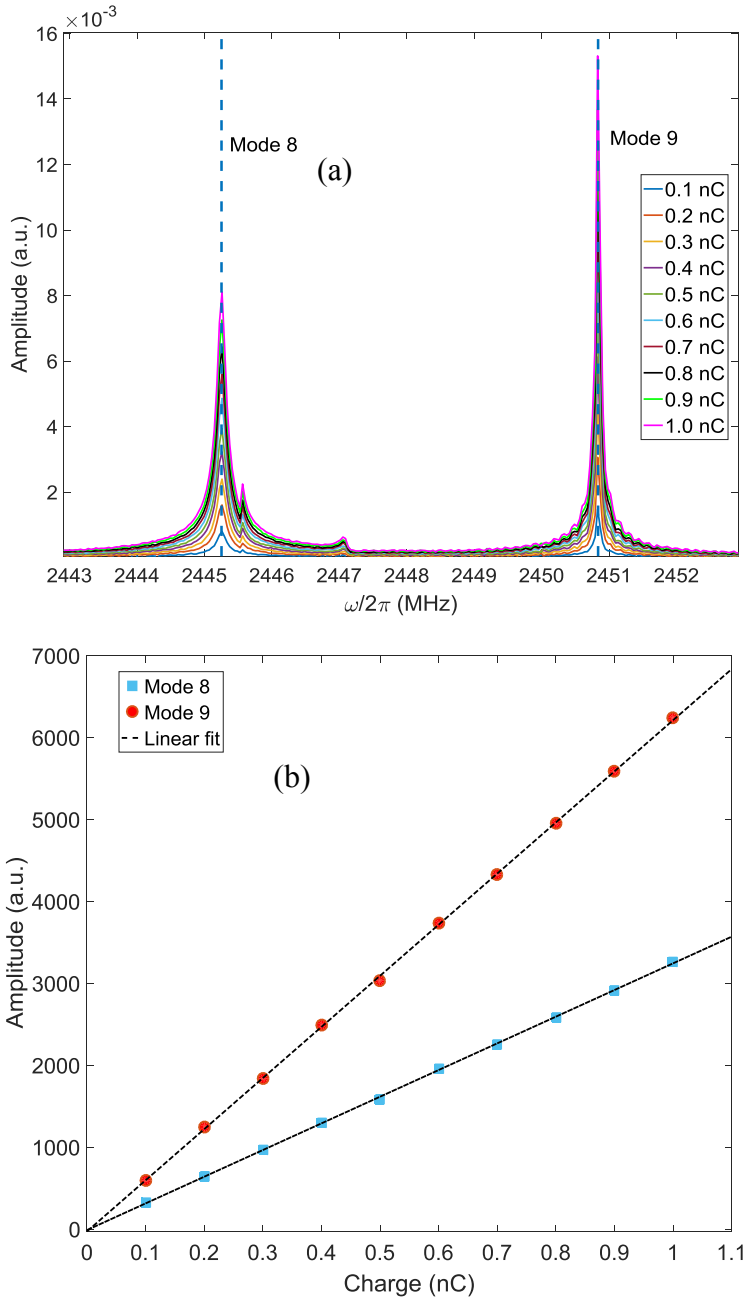

Figure 5.14 (a) Spectra of modes 8 and 9 for various bunch charges and (b) amplitude of modes 8 and 9 for various charges. The measurements were made at cavity 2 at the injector module of the E-XFEL.

For each charge, the RF phase was set to 0°, -5° and 5°. Figure 5.15 shows the calculated phase for a beam charge of 0.5 nC at an accelerating gradient of ~22 MV/m. For each phase, 25 measurements were made. The resolution is 0.12° in this case.

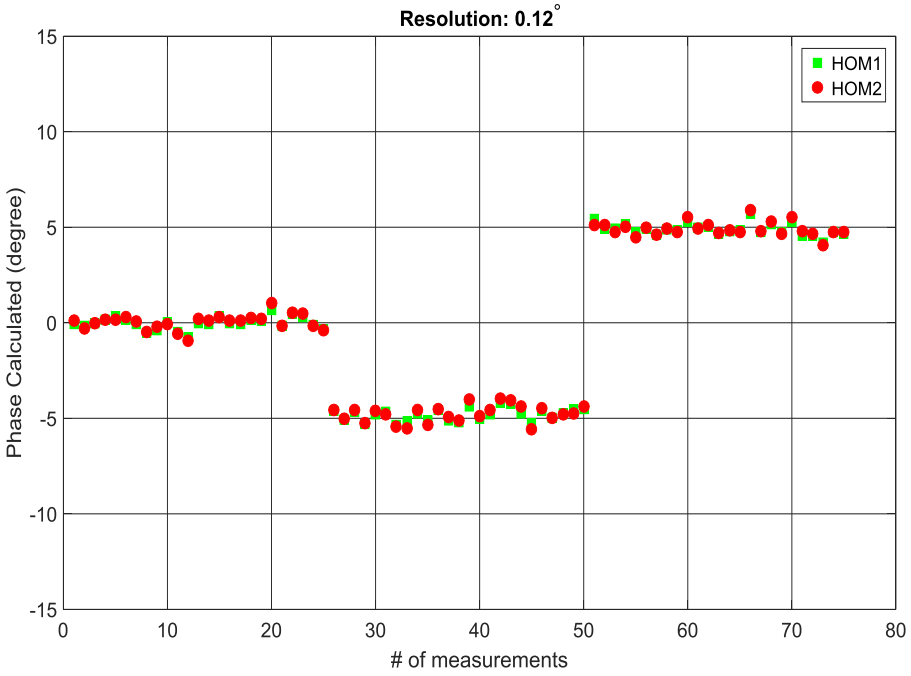

Figure 5.15 Phase obtained based on modes 8 and 9. For each set RF phase, 25 measurements were made. The beam charge is 0.5 nC and the accelerating gradient is ~22 MV/m. The resolution is 0.12°.

The simulation data was scaled with the signal strength measured for the different charges in the measurements. As mentioned before, a 10 dB power difference in channels 1 and 2 is observed and therefore is incorporated in the simulation data as well. The phase of the 1.3 GHz signal is changed by -5°, 0° and 5°. Twenty five calculations are made at each phase value. The comparison between the measurement and the simulation results is shown in Figure 5.16.

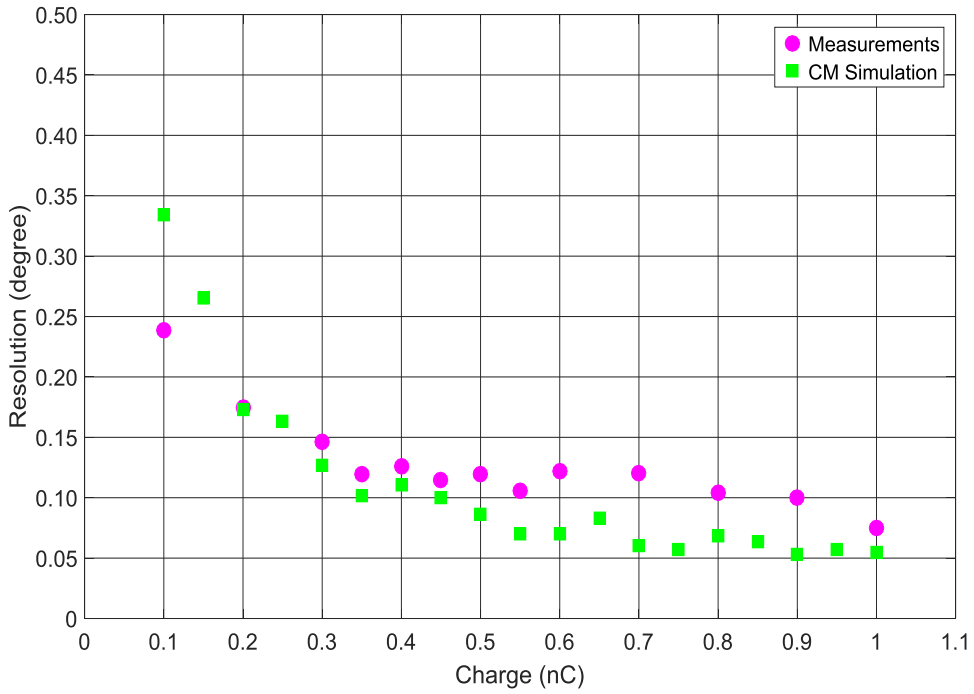

Figure 5.16 Resolution comparison between the measurements and the simulation from circuit model (CM).

The difference is generally below 0.05° except at 0.1 nC where the discrepancy is close to 0.1°. This is due to the fact that a different laser spot size and settings need to be used at low charges and the resolution is more sensitive to the charge fluctuations at low charge.

With a bunch charge of 0.5 nC and an accelerating gradient of ~ 20 MV/m, the resolution is approximately 0.1° both at the E-XFEL and FLASH. The low resolution is observed when the 1.3 GHz signal level is comparable to the noise floor as measured at cavities 2 and 7 in the 5th cryomodule at FLASH. The highest resolution (0.03°) with the current setup is observed at cavity 8 in the 5th module at FLASH. Attenuators were used at FLASH to protect the HOM electronics. By removing them, the resolution can be improved by a factor of 2-4 depending on the specific cavity. More interestingly, assuming a 10 dB improvement in SNR, equation 5.8 predicts that the resolution improves by a factor of 3.

5.3.4. Comparison between HOM-based and LLRF measurements

For the LLRF system, the beam phase is inferred from the 1.3 GHz RF field probe signal. This phase is referred to as probe phase later for discussion, and is available from the DOOCS control system. Based on the experimental setup (see Figure 5.8), the HOM-based phase or HOM phase is determined.

For comparison, the RF phase was changed at the klystron from -10° to 10° with a step of 1° and five measurements were recorded at each step as shown in Figure 5.17.

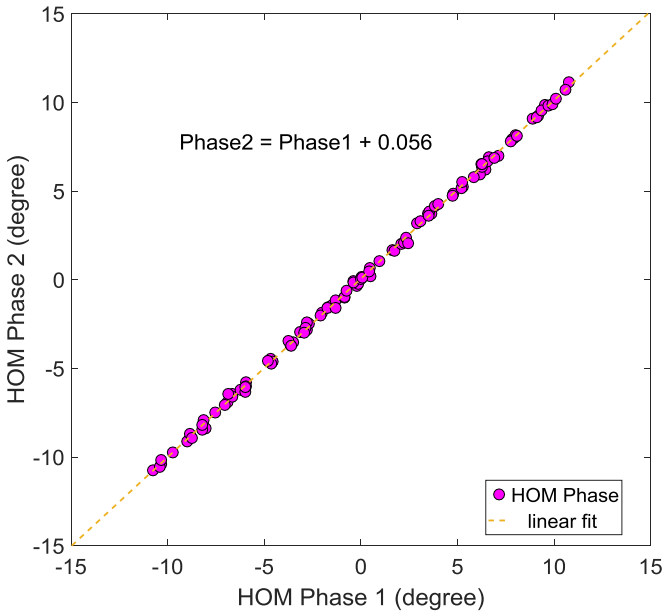

Figure 5.17 HOM phase response when the RF phase is changed. A linear dependence of the two channels indicates that the HOM system gives the consistent phase.

During the measurements, the vector sum phase of all cavities connected to one RF station (VS phase) [65] and the probe phase were also recorded. A comparison between the VS phase and HOM phase is shown in Figure 5.18 (a). The RMS error between the two is approximately 0.4°. The comparison between the probe phase and HOM phase is shown in Figure 5.18 (b). The RMS error between the two is approximately 0.3°. The RMS error is mainly due to the fact that the setup is not fully synchronized with each bunch. The synchronization of the future system is guaranteed by dedicated timing system and is expected to reduce this error.

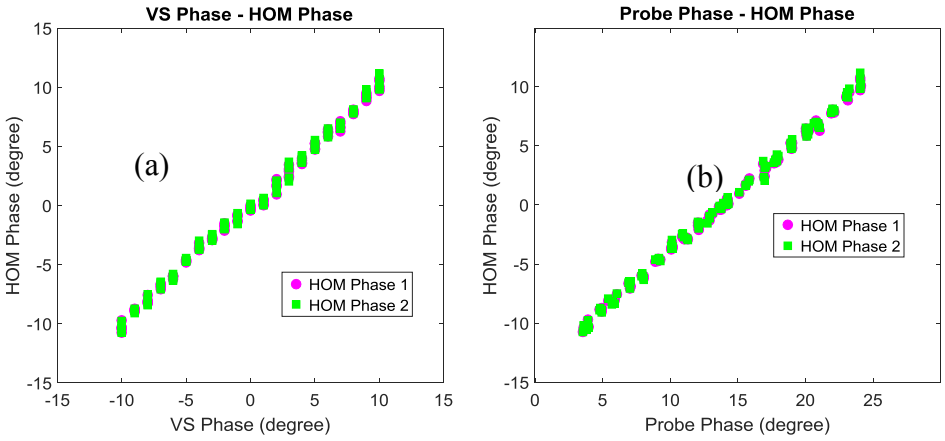

Figure 5.18 HOM phase versus VS phase (a); HOM phase versus probe phase (b).

The RF phase is fixed at 0° and 50 measurements are made. The histogram of the HOM phase from channels 1 and 2 and the probe phase are shown in Figure 5.19.

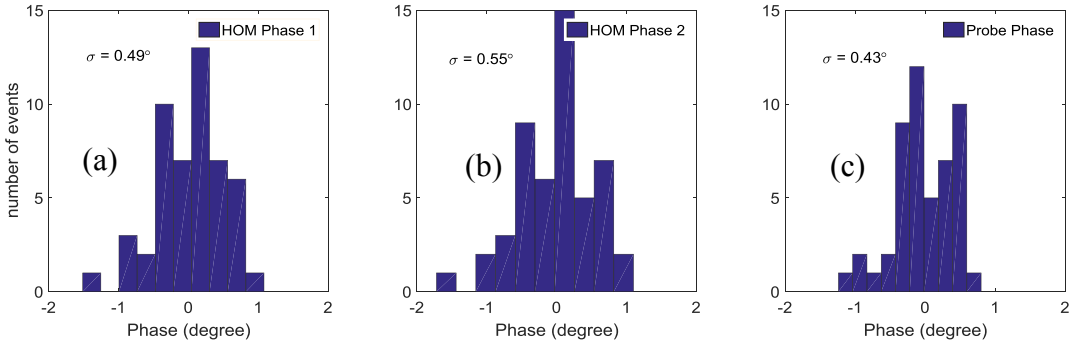

Figure 5.19 Histogram of HOM phase and probe phase when the beam phase is set to zero.

The standard deviation of HOM1 and HOM2 are 0.49° and 0.55° respectively. As a comparison, the standard deviation from the probe phase is 0.43°. The HOM phase is consistent with the probe phase. This result is also expected to be improved with fully synchronized measurements in the future.

5.3.5. Theoretical resolution limit

The resolution of the phase monitor has a strong dependence on the noise level in the system. In this section, the theoretical resolution limit is estimated assuming that only thermal noise is present. The smallest measurable thermal energy, U_{th} , is [66]:

$$U_{th} = \frac{1}{2} k_b T, \tag{5.9}$$

where k_b is the Boltzmann constant, and $T = 300K$ the room temperature. The amount of energy is approximately 2.07×10^{-21} J or 0.013 eV.

The energy deposited into mode 8 for 0.5 nC charge is:

$$\begin{aligned} U_8 &= \frac{\omega}{2}\frac{R}{Q} q^2 = 0.6 \frac{V}{pC} \cdot 500^2 (pC)^2 = 150k\ V \cdot pC \\ &= 9.4 \times 10^{11}\ eV. \end{aligned} \tag{5.10}$$

A fraction, β, of the deposited energy into this mode can be coupled out through the HOM coupler [6], which is assumed to be 0.5. The SNR based on mode 8 and the thermal detectable noise power is then 136 dB. The resolution at this SNR, based on equation 5.8 at 20 GS/s sampling rate, is 6×10^{-8} degree, which is much better than the required 0.01°. In reality the best measured resolution is 0.03°. In this case, the SNR is approximately 22 dB, which predicts a resolution of approximately 0.04° based on the fitting formula in Figure 5.5. Therefore the SNR dominates the resolution. To meet the 0.01° phase resolution requirement, the specially designed electronics can be used to amplify the signal level and limit the noise level to achieve a higher SNR compared to the current measurement setup based on the fast scope.

5.4. Summary and Outlook

The coupled LC circuit model described in Chapter 3 has been used to aid the development of an HOM-based beam phase monitor for 1.3 GHz cavities. The results show that the resolution of the monitor depends crucially on the SNR in the system.

A data acquisition system has been set up based on a fast scope and various industrial standard connection protocols. The measured resolution is approximately 0.1° for both FLASH and the E-XFEL. This is in agreement with circuit simulations, which show that the resolution is governed by the SNR. The best resolution achieved with current experimental setup is 0.03°. The dedicated electronics now under design for the beam phase monitor can improve the SNR by amplifying the signal level and limiting the noise level compared to the current setup based on oscilloscope. This will in the end improve the resolution to meet the 0.01° resolution requirement.

The HOM-based beam phase measurement agrees with the one from the LLRF system and can be integrated into it. The system can be used for long term RF drift monitoring, which is a desirable feature for LLRF system. It is also very critical to identify the phase jitter sources in the injector part because the contributions from RF gun, 1.3 and 3.9 GHz cryomodules are coupled. The developed beam phase monitoring technique can be used to fulfil the task. It should be pointed out that these application scenarios do not require 0.01° resolution.

The electronics that will be used for the beam phase monitor is based on a technique called direct sampling. The electronics integrate the HOMBPM and the HOMBPhM onto the same PCB board. The system will be compact and avoid the issue of phase noise from a local oscillator. The electronics is based on the MicroTCA[14] standard and will be synchronized fully by the DOOCS system. A description of the prototype electronics can be found in [8]. Two topologies can be used for the system. One topology is that the data acquisition unit can be installed as closely as possible to the cryomodule. The data can be processed locally and the results are transferred digitally which is immune to various environmental influences. The disadvantage is that the electronics should be carefully shielded. The other topology is to transfer the signals from the tunnel to an instrumentation room where radiation is not an issue any more. However, the signal integrity might be an issue. Our current measurements are based on the latter topology. The future HOM electronics

[14] see http://mtca.desy.de/

for beam phase measurements will be situated directly under the cryomodule in the tunnel at the E-XFEL.

The 3.9 GHz cavity can, in principle, also be used as HOMBPhM. A band of trapped monopole modes needs to be found. In principle, any trapped mode inside a cavity can be instrumented for beam phase monitoring. The issue however is that the non-monopole modes depend on the beam offset. Also, for a well-centered beam, the beam excites no transverse HOMs so that no phase can be extracted due to the vanishing amplitudes of these modes.

Chapter 6 - HOM-based Beam Position Monitoring

The amplitude of a dipole mode has linear dependence on the beam offset. Based on this fact, HOMBPMs have been built in the past for 1.3 GHz cavities [6] and 3.9 GHz cavities [7] at FLASH. Similar systems are under development for the E-XFEL. However, the fact that the HOMBPMs lose the prediction ability over time, as observed at FLASH prevents them working as robust BPMs. This chapter presents the principles of the HOMBPMs and the techniques used to mitigate the instability.

In section 6.1, the principle behind this method is described, and data analysis techniques are presented. The resolution of the HOMBPM has been monitored over several months. Also when bunch travels obliquely with respect to the cavity axis, an ambiguity arises in terms of beam position. This is discussed in section 6.2.

6.1. HOM-based Beam Position Monitoring

As discussed in Chapter 2, when a bunch of electrons traverses a cavity, HOMs are excited. When the beam offset relative to the radius of the beam pipe is small, the transverse wakefield is dominated by dipole modes [35]. These dipole modes are themselves restricted to a series of bands. Each component presents a transverse momentum kick to the beam [3]. Here I focus on those with the largest kick factors as only these are likely to have an appreciable impact on the beam dynamics and to produce sufficiently large radiation to the attached HOM couplers. This large radiation provides high sensitivity for beam position monitoring.

In the following subsections, the principle of a HOMBPM (section 6.1.1), data preparation and signal processing (section 6.1.2), HOMBPM calibration (section 6.1.3) and characterization (section 6.1.4) are discussed. Due to the unavailability of the HOMBPM system during my project at the E-XFEL, the study is based on a similar system installed at FLASH.

6.1.1. Introduction to HOMBPM

HOMBPM system is under development for both 1.3 and 3.9 GHz cavities at the E-XFEL. Both systems share the same principle by correlating the signal to the beam position. The only difference is that the signal to be used is from a single mode at 1.3 GHz cavities and from a band of modes at 3.9 GHz cavities. The following study will be based on the 1.3 GHz cavities unless otherwise specified.

HOMBPMs are based on the beam-excited dipole signals radiated to the HOM couplers. Their strength is linearly dependent on the beam charge and offset. By normalizing to the beam charge, the beam offset can be obtained. A schematic of the HOMBPM signal processing at FLASH is shown in Figure 6.1. It should be noted that, for TESLA cavities, there is no down-converting stage for the HOMBPM system at the E-XFEL.

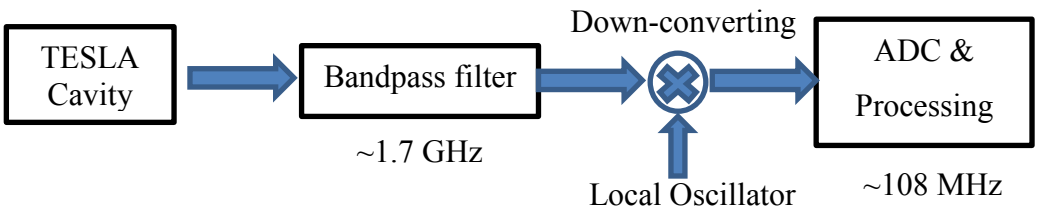

Figure 6.1 Schematic of the HOMBPM signal processing. The bandpass filter is centred at 1.7 GHz and has a bandwidth of 20 MHz. The ADC sampling clock has a frequency of 108.3 MHz.

A dipole mode at ~1.7 GHz (TE111-6) [51] was selected for beam position monitoring because it has strong coupling to the beam and hence will enhance the sensitivity. The HOM signal is filtered at approximately 1.7 GHz with a 20 MHz bandwidth and down converted to 20 MHz IF (intermediate frequency) signal [51]. The IF signal is then sampled at approximately 108 MHz and transmitted to the DOOCS control system [67]. A MATLAB® program was developed to perform data acquisition and processing. An example of signal in the time and the frequency domain is shown in Figure 6.2. The waveform is approximately 19 μs in duration. The corresponding spectrum obtained by FFT spans 0-54 MHz.

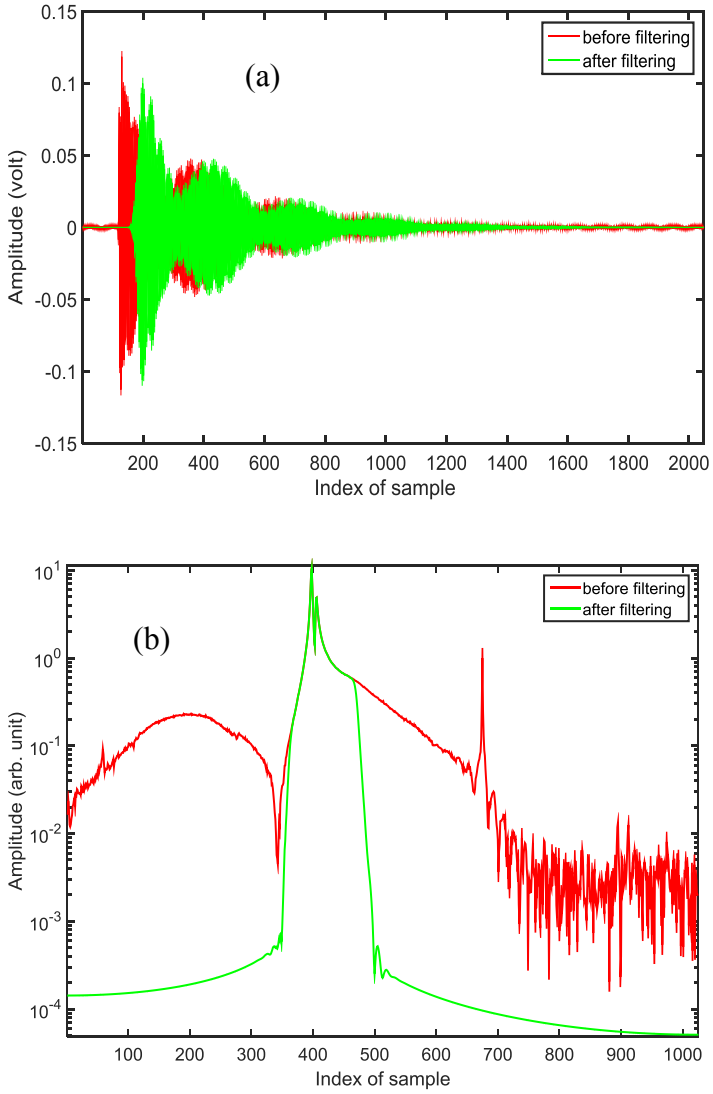

Figure 6.2 Example of a dipole signal before (red) and after (green) Butterworth filter in time domain (a) and frequency domain (b). Note that the filter does not refer to the one used in the electronics. The noise at high frequency (index > 700) has been attenuated in (b) after filtering. The waveform is approximately 19 μs in duration. The frequency in (b) is in the range of 0-54 MHz.

6.1.2. Data preparation and signal processing

All data were recoded with a MATLAB® program synchronously [68] bunch by bunch based on the interface provided by the DOOCS control system.

6.1.2.1. Data preparation

Signals from all 16 HOM couplers in the 5th cryomodule at FLASH were recorded. The charge was read from the nearby toroid. The beam positions were obtained from two BPMs located upstream and downstream of the module. The schematic of the measurement setup is shown in Figure 6.3. A straight beam trajectory is guaranteed by switching off quadrupoles, dipoles, and RF inside the module between the two BPMs.

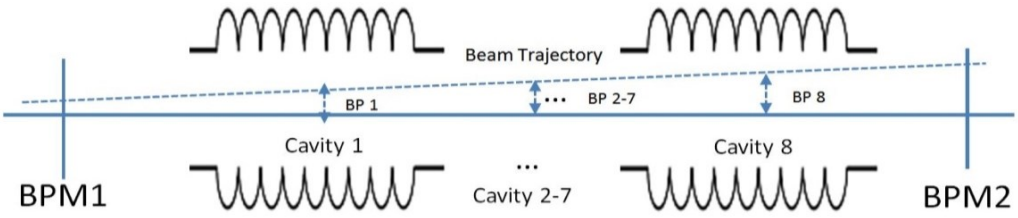

Figure 6.3 Schematic of the measurement setup. The beam positions are recorded by BPMs 1 and 2. Provided the beam travels in a straight trajectory, the beam position in each cavity can be interpolated.

Each dipole waveform has 2048 samples at approximately 108 MHz sample rate. Prior to calibration, I carefully removed data points outside the linear range of BPMs. The saturated dipole waveforms were also eliminated. The HOMBPMs were calibrated in an approximately 2×2 mm^2 range and were evaluated with a different set of data from the same day. Data gathered from other days were used to evaluate the performance.

The data is constructed as in a matrix format:

$$D = \begin{pmatrix} data_1 \\ data_2 \\ \vdots \\ data_m \end{pmatrix} = (d_1, d_2, \dots d_n) \in R^{m \times n}, \qquad 6.1$$

where $data_m$ represents the m^{th} measurement. Typically, the digitized waveforms or their amplitudes are put in the matrix row wise. The position data is organized in a similar way:

$$P = \begin{pmatrix} x_1 & y_1 \\ x_2 & y_2 \\ \vdots & \vdots \\ x_m & y_m \end{pmatrix} \in R^{m\times 2}, \qquad 6.2$$

where (x_m, y_m) is the beam position at the centre of the cavity interpolated from the two BPM readings. The process of calibration aims to find the coefficients between the data matrix D and the position matrix P. Before calibration, the signals were preprocessed to remove components that have weak correlation with the beam position.

6.1.2.2. Dipole signal processing

It was found that there was phase noise in the dipole signals. This noise is induced by the mode frequency variation as described in Chapter 4 and the electronics. To correct the phase noise is not trivial. Therefore I used the magnitude of spectrum of a dipole signal. Besides, there are also components in the signal which have no correlation with the beam position and need to be filtered.

The main information is contained within the two peaks (index 350~500) in Figure 6.2 (b). These two peaks have linear dependence on the beam position [69]. The rest of the spectrum is irrelevant for beam position although a finite quality factor and frequency leakage will cause it to have a weak correlation with the beam position. A 15th order Butterworth bandpass digital filter was designed to process the waveform and remove the unwanted part. The magnitude of the passband is nearly unity (0.1 dB ripple) while the stopband of the filter provides enough damping (-100 dB). In principle an ideal filter could be applied to the spectrum directly, but that gives non-physical signals in time domain which is not desirable and impossible to implement in hardware.

One example of a signal before and after filtering is show in Figure 6.2. Since the following analysis does not rely on the phase information, the obvious distortion of phase does not concern us here. The filtered spectra were normalized with respect to

the charge. The data was not normalized with respect to the charge measured directly but with respect to the mean value from multiple measurements during each beam time. In this way, I potentially minimize the noise of the charge measurements from the toroid of ca. 3 pC RMS[15]. The histograms of charge measurements on various dates are shown in Figure 6.4.

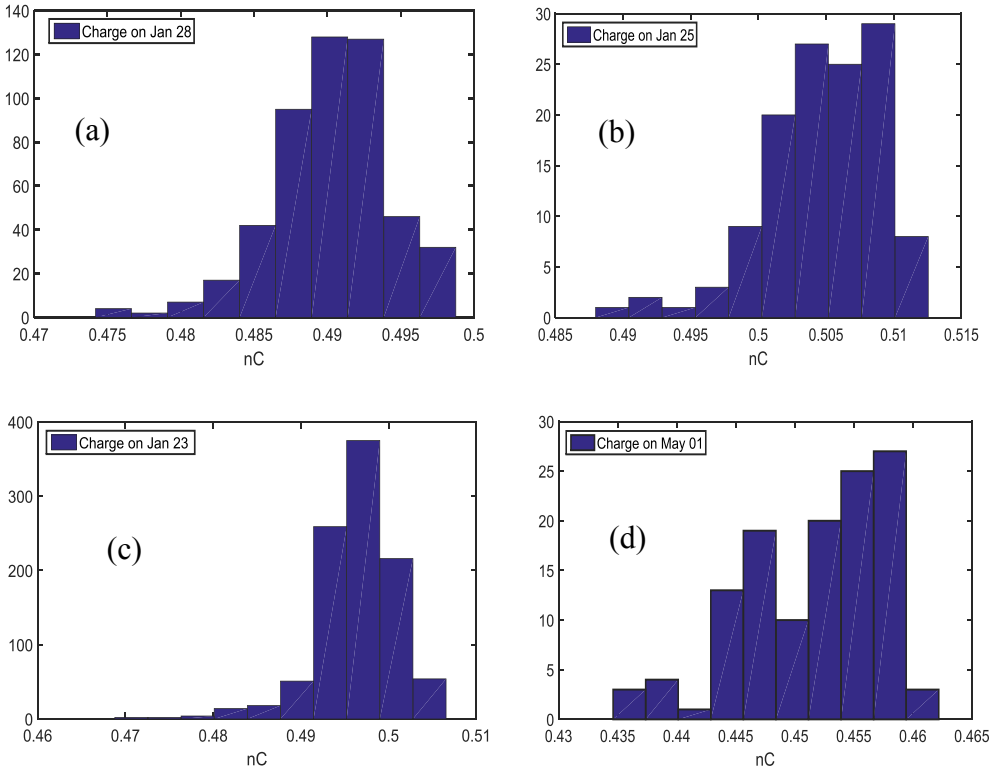

Figure 6.4 Histograms of charge measurements on January 28 (a), 25 (b), 23 (c) and May 01 (d) in 2015. Note that the number of charge measurements is more than the number of data used for calibration. The standard deviation of each histogram is ~0.4%.

Finally, the filtered spectra are organized into data matrix D for calibration. Forty four measurements were selected for calibration from data taken on January 28, 2015. Another 44 measurements were used for validation from data obtained on the same day. Data from January 25, 23 and May 1, 2015 were selected to be within the calibration range (see Figure 6.5 (a)) and used for evaluating the calibrated HOMBPM (called validation in this thesis).

[15] The toroid system has been improved below 1 pC RMS at the E-XFEL.

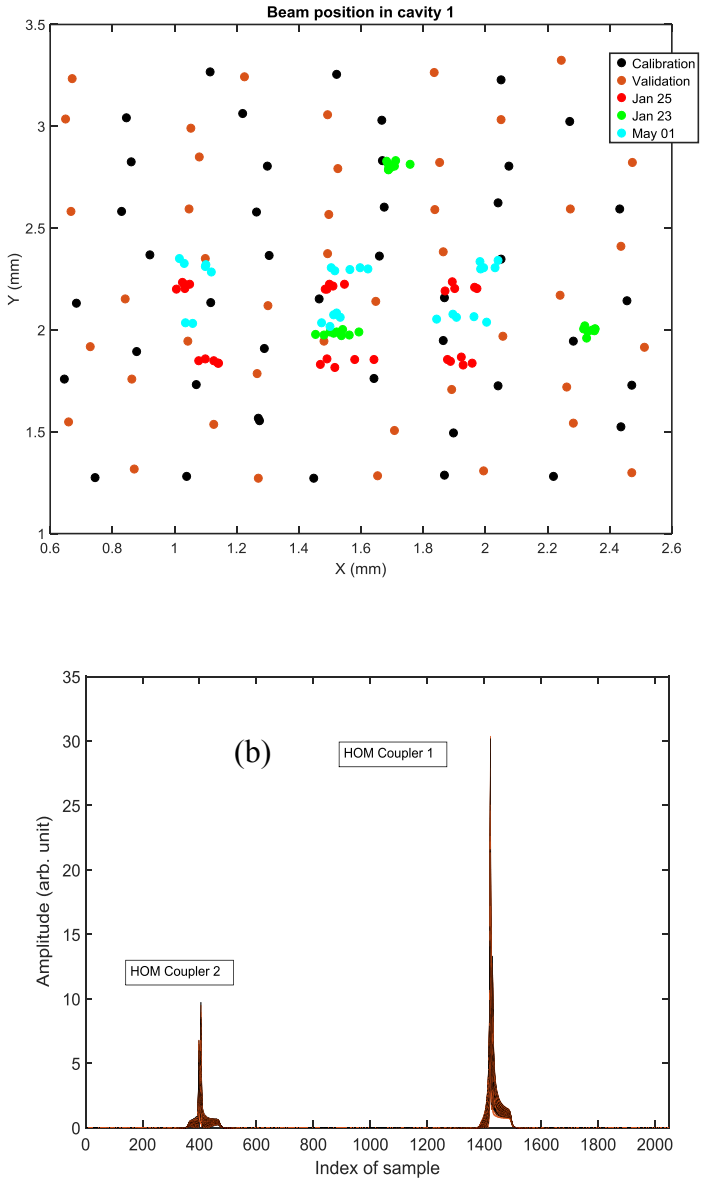

Figure 6.5 Interpolated beam position (see Figure 6.3) in the first cavity at 5th cryomodule used for calibration, validation and characterization; (b) dipole spectra from both HOM couplers are concatenated into a single spectrum.

6.1.3. HOMBPM calibration

Model independent analysis methods are used to extract the beam position. I applied three methods namely PLS (Partial Least Square), SVD (Singular Value Decomposition) and ANN (Artificial Neural Network) to calibrate and compare their performance.

The HOMBPMs in the first three cavities of the 5th cryomodule in FLASH were calibrated and analysed in order to evaluate the performance of the HOMBPM.

6.1.3.1. RMS error and resolution

The RMS error is used as a figure of merit to assess the calibration. The RMS error is defined as the root mean square of the difference between interpolated beam positions from the two BPMs (Figure 6.3) and the calibrated readouts from the HOMBPMs:

$$E_{rms} = \sqrt{\frac{1}{m}\sum_{i=1}^{m}(P_i - P_i^H)^2}, \tag{6.3}$$

where P_i^H is the beam position given by the HOMBPM for measurement i, P_i the interpolated beam position from the two BPMs for measurement i, and m the number of measurements.

The resolution is calculated based on the three-BPM method [70] (see Appendix B). More specifically, beam positions given by HOMBPM in cavity 2 were compared with beam position given by HOMBPMs from cavity 1 and 3. One σ of the residuals can be calculated. By applying the geometrical factor $\sqrt{2/3}$ [6], [70], the resolution of the HOMBPM can be obtained by:

$$R_{HOMBPM} = \sqrt{\frac{2}{3}}\sqrt{\frac{1}{m}\sum_{i=1}^{m}(P_2^H - aP_1^H - bP_3^H - c)^2}, \tag{6.4}$$

where $P^{H}_{1,2,3}$ represent the beam position measured by HOMBPM at cavity 1, 2 and 3. The coefficients a, b and c can be calculated by linear regression [70]. The HOMBPMs 1, 2, 3 were assumed to have identical resolution in the calculation.

6.1.3.2. HOMBPM calibration based on PLS, SVD and ANN

Three methods, PLS, SVD, and ANN, are used to extract the beam position from the spectra of the dipole signals. The calibration procedure is: 1. Interpolate the beam position into each cavity under consideration and build matrix P (equation 6.2). 2. Concatenate the dipole signal spectra from both couplers of a cavity and build matrix D (equation 6.1). 3. Calculate the correlation between the matrices P and D.

Written in a compact matrix form, it reads:

$$D \cdot C = P, \tag{6.5}$$

where C can be obtained by multiple linear regressing D against P. Each row in matrix D corresponds to one measurement, and each column corresponds to one predictor in the regression model. One drawback of using direct regression is that, as it will be seen below, the predictors are correlated with each other. To alleviate the potential issues, I adopted partial least square regression [71]. In this thesis, the components found by PLS methods are called latent components and they were put in matrix D.

In the SVD method, the amplitudes of dipole signal in the SVD mode space were used for matrix D. The calibration matrix can be obtained by linearly regressing D against P.

The calibration matrix C can also be represented by a neural network to map the complicated relations, if any, between D and P. To this end, I designed one

feedforward neural network based on the Bayesian regulation algorithm [72], [73]. The three methods are discussed respectively in the following subsections.

- Calibration based on PLS

In principle each sample from the spectrum (i.e. each column of *D*) can be treated as a single predictor in the linear regression model. However, many samples are correlated to a certain extent. The correlation coefficient is defined in equation 6.6:

$$Cor_{ij} = \frac{Cov(d_i, d_j)}{\sqrt{Cov(d_i, d_i)Cov(d_j, d_j)}}, \qquad 6.6$$

where d_i and d_j are the i^{th} and j^{th} column of matrix D defined in equation 6.1, $Cov(d_i, d_j)$ is the covariance between d_i and d_j. $Cor_{ij} = \pm 1$ when there is a positive/negative linear correlation between d_i and d_j. $Cor_{ij} = 0$ if there is no linear correlation between d_i and d_j.

The samples between index 400 and 500 in the dipole spectrum are highly correlated as illustrated by the dark red colour in Figure 6.6. This violates the assumption of independence among predictors in multiple linear regression and the regression is vulnerable to noise from measurement [71].

The PLS regression algorithm was applied to overcome this issue [71]. I used PLS to find latent components in the spectrum that have high correlation with the beam position. Normally the number of components found is significantly smaller than the number of samples. The correlations between latent components were found to be zero.

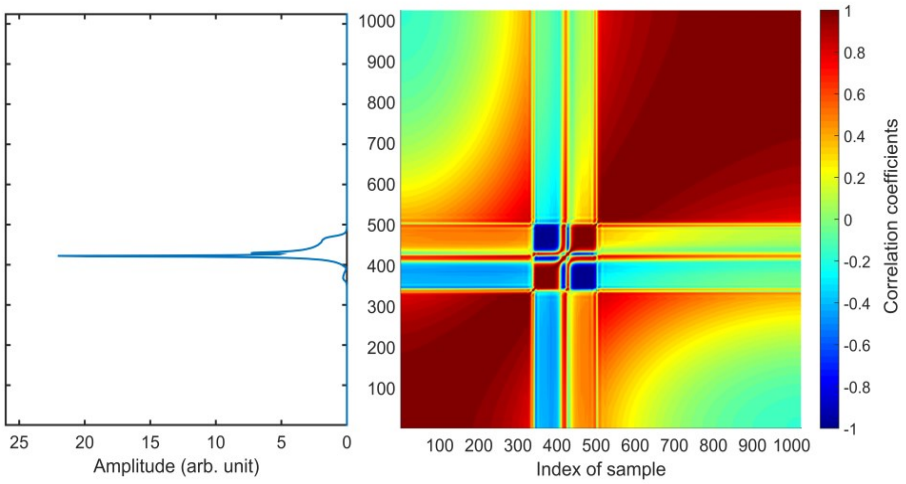

Figure 6.6 Correlation coefficients of individual samples in the dipole spectrum (from HOM coupler 1 of the first cavity at 5th cryomodule). Note: the dipole peak region (index 400-500) is highly correlated as indicated by the dark red colour.

The latent components are put in the data matrix D column wise. The linear regression of D against P is performed to find the calibration matrix C. The RMS error (for both calibration and validation) dependence on the number of latent components is shown in Figure 6.7 for cavity 1. Similar results were obtained for cavities 2 and 3 [75].

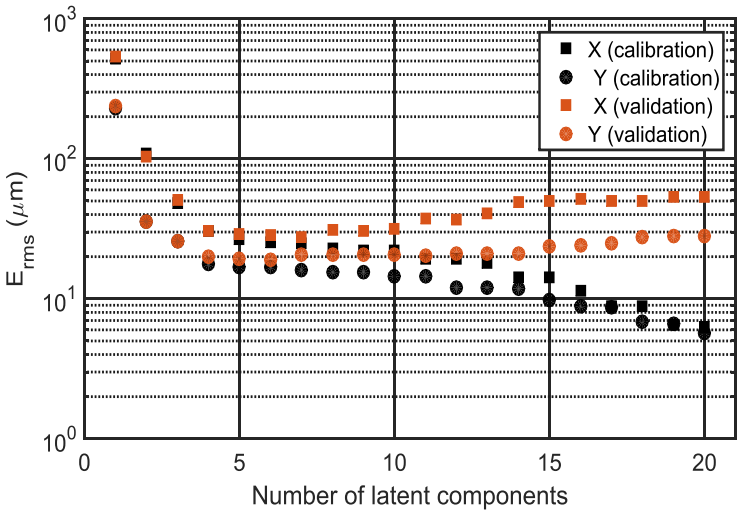

Figure 6.7 The RMS error dependence on the number of latent components for HOMBPM 1. Data from January 28 was used for both calibration and validation.

The minimum number of latent components needed for calibration without increasing the validation RMS error is six. Therefore, six latent components were used for calibration and later for the resolution calculation.

- Calibration based on SVD

In the SVD method, the spectrum matrix D is decomposed to find a number of principal components (SVD modes) that can best represent the original matrix in a least square sense:

$$\mathrm{D} = \mathrm{U} \cdot \mathrm{S} \cdot \mathrm{V}^{\mathrm{T}}, \tag{6.7}$$

where U and V^T represent singular vectors and S is a diagonal matrix that contains the singular values. The details of the SVD method can be found in [6], [7], [76]. The original data matrix D can be reconstructed based on the top k modes (D_k) with good approximation. The Euclidean norm between D and D_k is,

$$\|D - D_k\| = S_{k+1}, \tag{6.8}$$

where S_{k+1} is the $(k+1)^{th}$ singlar value in equation 6.7. This gurantees that the matrix D_k is a good approximation to D in the least square sense.

Figure 6.8 (a) shows the top 30 singular values found by the decomposition. The singular values change by almost three orders of magnitudes for the top 30 modes.

The singular vectors in V are the SVD modes found by decomposition. The top two modes are shown in Figure 6.8 (b). The first SVD mode resembles the original dipole spectrum. These modes found are generally a combination of physical modes [6].

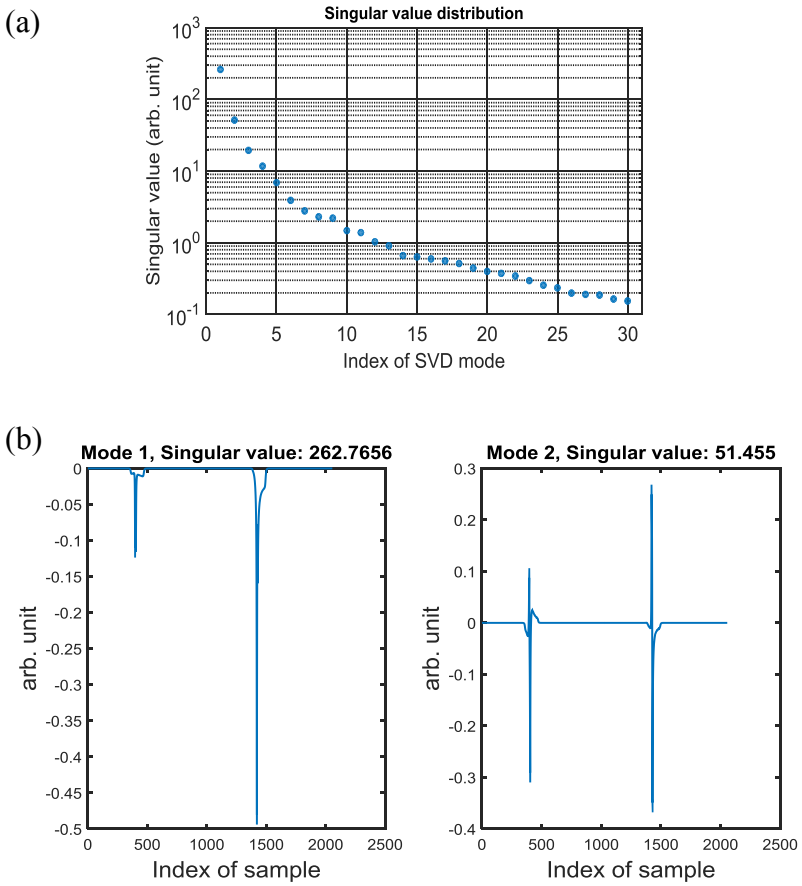

Figure 6.8 (a) The singular values of the spectrum matrix in cavity 1 and (b) the corresponding top 2 SVD modes.

The amplitude for each spectrum in the SVD mode space can be calculated by the dot product:

$$A = D \cdot V = (A_1^{SVD}, A_2^{SVD}, \dots A_n^{SVD}), \tag{6.9}$$

where A_n^{SVD} is a vector containing the amplitudes for all measurements in the nth SVD mode.

Figure 6.9 shows the reconstructed spectra based on eight SVD modes. The correlation between the amplitudes A_n^{SVD} and the beam position is shown in Figure 6.10. One can observe the amplitude's linear dependence on the beam position for the first two SVD modes. This justifies the usage of linear regression with small number of modes. However the dependence becomes complicated with more modes

taken into consideration. This motivates the use of ANN to mimic the complicated relation.

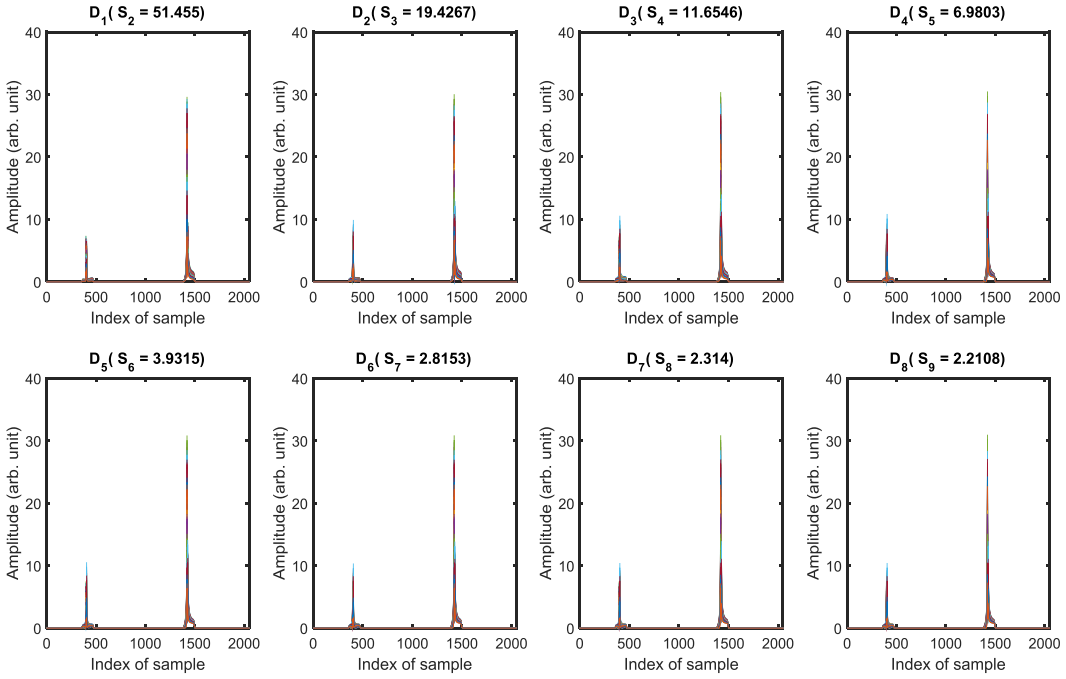

Figure 6.9 Spectra reconstructed based on various number of SVD modes used. D_i means that the first i SVD modes were used for reconstruction. S_i is the singular value or the Euclidean norm between the original matrix and the reconstructed one (equation 6.8).

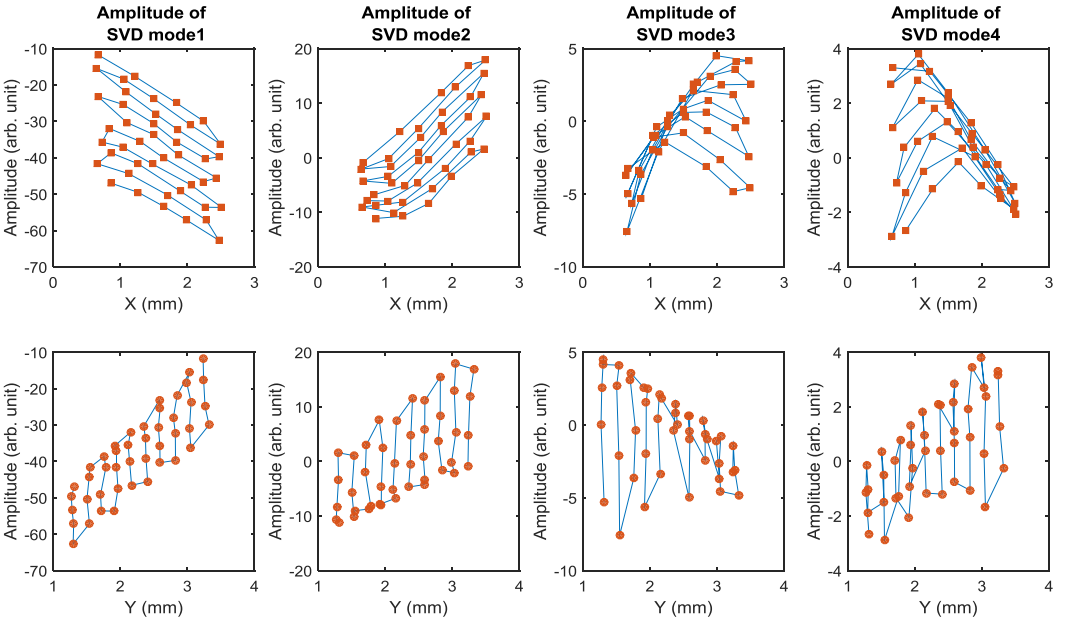

Figure 6.10 The SVD mode amplitudes versus the beam positions in cavity 1. It is based on the first cavity at module 5. The blue lines are used to indicate the beam movement sequence.

The SVD mode amplitudes (A in equation 6.9) are put in the data matrix D column wise. The linear regression of D against P is performed to find the calibration matrix C.

The RMS error (for both calibration and validation) dependence on the number of SVD modes is shown in Figure 6.11 for cavity 1. Similar results were obtained for cavities 2 and 3 [75].

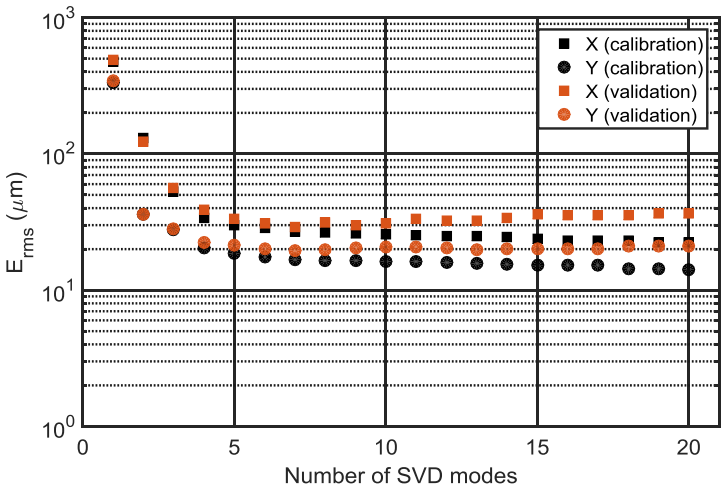

Figure 6.11 The RMS error dependence on the number of SVD modes for HOMBPM 1. The calibration and validation were performed on January 28, 2015.

The minimum number of SVD modes needed for calibration without increasing the validation RMS error is 7, 11, and 14 for cavities 1, 2 and 3 respectively. It should be pointed out that the number of modes chosen for calibration is somewhat arbitrary within the region where the RMS error has minor change (e.g. modes number 7-11 in Figure 6.11). Reducing or adding a few modes has a minor influence on the RMS error.

- Calibration based on ANN

Artificial neural network (ANN) is a branch of statistical learning methods [77]. It can be used to learn the complicated relationship from inputs to outputs and has wide applications in machine learning. There is a wide range of topologies available for different purposes [78]. For beam position extraction, I used feedforward neural

network based on one hidden layer with 20 neurons for computation. The inputs are the amplitudes calculated in the SVD method. Effort was mainly made to optimize the number of inputs for the network with a fixed hidden layer. The number of neurons is less concerned because Bayesian regulation techniques are adopted to find the optimal size automatically. A detailed description of the algorithms can be found in [79]. One schematic of an ANN is shown in Figure 6.12.

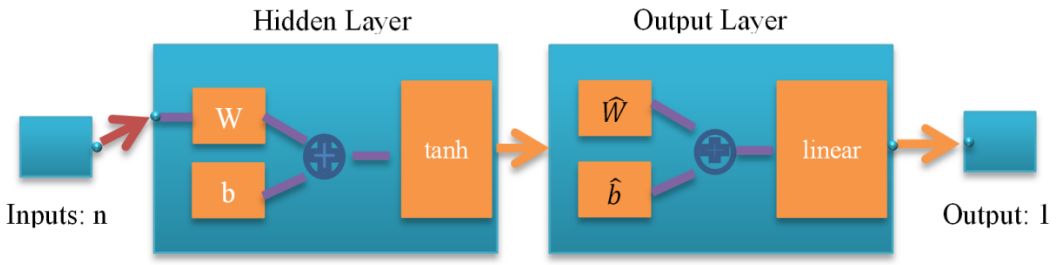

Figure 6.12 Schematic of a feedforward neural network. The number of inputs n was varied from 1 to 20 and the number of hidden neurons is fixed at 20. The number of outputs is set to 1 (for x or y position).

The input and output mapping can be written as:

$$x \text{ or } y = \sum_j \widehat{w}_j \tanh\left(\sum_i^n w_{ij} d_i + b_j\right) + \hat{b}, \qquad 6.10$$

where w_{ij} represents the weight for the synapse connection i and j in the hidden layer, b_j is the bias term. $\widehat{w}_j$ and $\hat{b}$ are the weight and bias for the output layer respectively.

In principle a fraction of the spectrum can be used to train the network. But it has proved to be less efficient and consumes large amount of computing time and memory. Therefore, the amplitudes used in SVD method were used as inputs for the ANN. The number of inputs was varied from 1 to 20 in order to find out the optimal number. The interpolated beam positions were used as the outputs (targets) for learning. This forms a supervised learning problem. Two separate networks were built for x and y respectively.

The RMS error dependence on the number of inputs (SVD modes) is shown in Figure 6.13 for cavity 1. Similar results were obtained for cavities 2 and 3 [75].

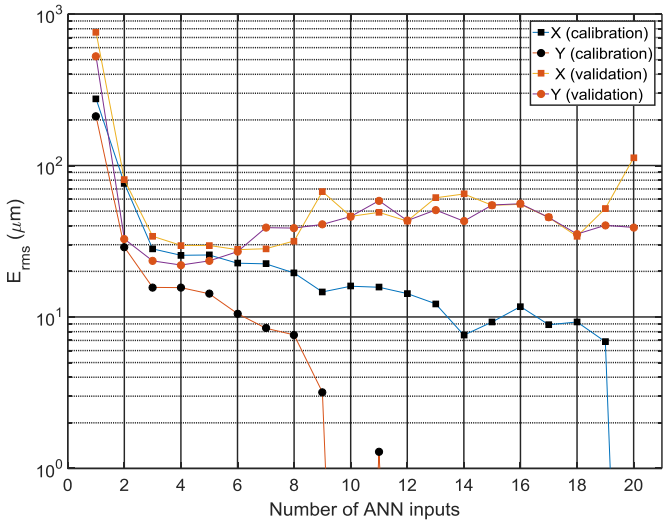

Figure 6.13 The RMS error dependence on the number of inputs for HOMBPM 1. The points with error below 1 micron are excluded and are regarded as over-trained by the network.

Therefore the number of inputs for ANN was chosen as 4, 2 and 3 respectively, based on the same criteria as for other two methods.

In summary, the HOMBPM is calibrated based on three different methods, namely PLS, SVD and ANN. The RMS errors for the calibration are summarized in Table 6-1. They show comparable performance with each other in terms of validation RMS error. PLS operates faster than the other two methods in general. ANN needs more time to converge in the learning (training) process. ANN used here refers to the topology presented in this section instead of ANN in a general sense.

Table 6-1 Summary of RMS errors for the calibration data on January 28

Method	PLS			SVD			ANN		
Cavity #	1	2	3	1	2	3	1	2	3
January 28 (x,y) (μm)	(25,17)	(30,19)	(36,25)	(27,17)	(31,17)	(32,16)	(26,16)	(33,22)	(35,30)

6.1.4. HOMBPM validation and characterization

6.1.4.1. HOMBPM validation

Datasets from January 25, January 23 and May 01, 2015 were applied to the calibrated HOMBPMs 1, 2 and 3 respectively. The RMS errors for all three methods are summarized in Table 6-2.

Table 6-2 Summary of RMS errors for January 23 and 25 and May 01 based on the calibrated HOMBPMs on January 28.

Method	PLS			SVD			ANN		
Cavity #	1	2	3	1	2	3	1	2	3
January 25 (x,y) (µm)	(42,32)	(46,40)	(60,30)	(43,32)	(47,37)	(55,31)	(46,37)	(66,33)	(63,46)
January 23 (x,y) (µm)	(32,34)	(41,74)	(40,77)	(35,33)	(43,68)	(41,82)	(37,37)	(78,61)	(43,104)
May 01 (x,y) (µm)	(49,42)	(49,73)	(51,75)	(49,43)	(51,76)	(49,68)	(51,49)	(55,81)	(52,71)

In Table 6-2 the RMS error tends to increase from cavity 1 to 3. This is due to the fact that BPM 2 used for interpolation has worse resolution than BPM 1 (see Figure 6.3).

Several factors contribute to the RMS error given in Table 6-2: 1. The resolution of the BPMs 1 and 2 used for calibration 2. Bunch angle effects (the angle is ~100-200 µrad for the calibration data) 3. The noise of HOMBPM electronics 4. The mechanical stability of the cryomodule including the BPMs.

It should be mentioned that the calibration using signal in time domain as in [6], rather than the frequency domain as shown above, also gives acceptable calibration RMS error (approximately 50 µm). However the RMS error for the validation degrades over time from 50 µm to millimetre range.

6.1.4.2. HOMBPM resolution

The resolution of HOMBPM is calculated based on equation 6.4. The minimum possible resolution, assuming that only thermal noise is present, is no more than

130 nm [6]. It was reported that the resolution of the HOMBPM is, to a large extent, limited by the charge measurement (contributes ~ 6 µm at 1 mm offset) and phase noise of the local oscillator (contributes ~ 1 µm at 1 mm offset) [6]. Instead of normalization to individual charge measurement, the mean value of multiple measurements was used. In this manner, the error in the charge measurement is reduced. The calibration based on the spectra of dipole signals mitigates the issue of phase jitter.

Using the procedure presented in the previous sections, a resolution below 2 µm is achieved in the y direction for January 23 and 25 and May 1, 2015 based on the PLS method. A resolution below 5 µm was observed for most of the data based on all three methods. The results are summarized in Figure 6.14.

(a) PLS

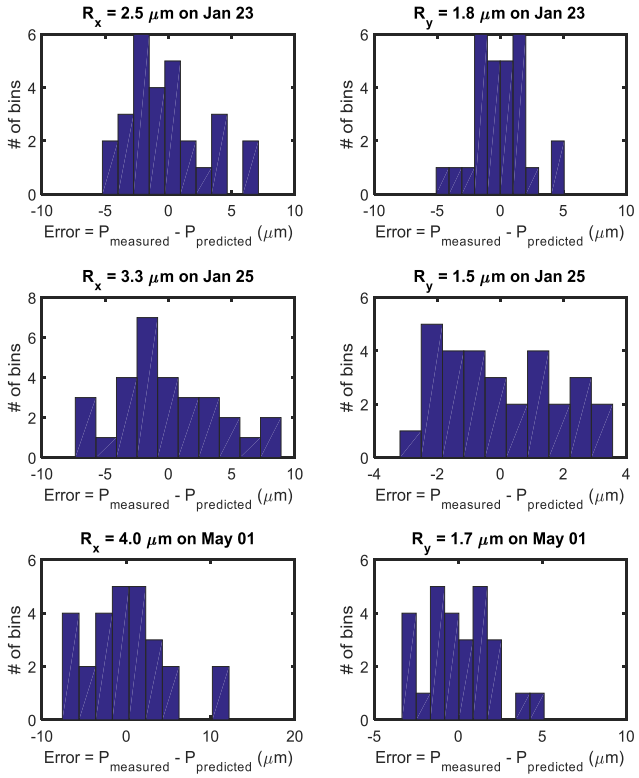

(b) SVD

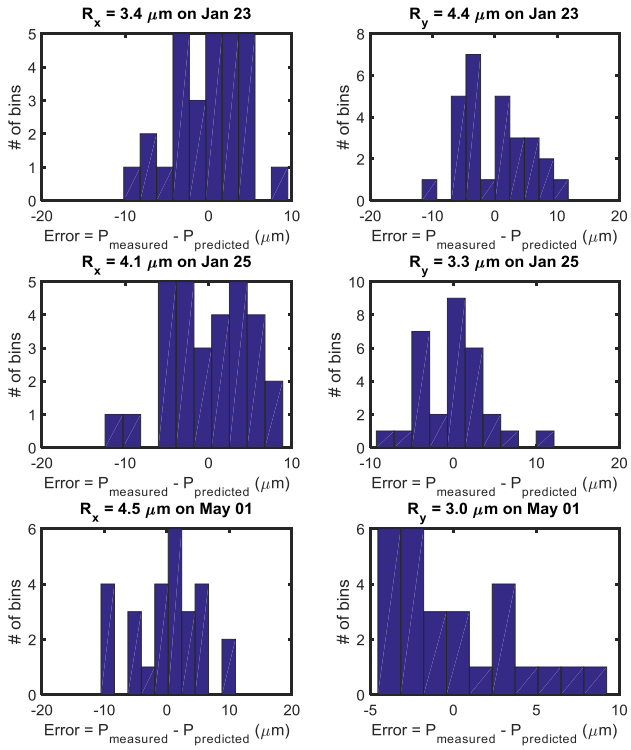

(c) ANN

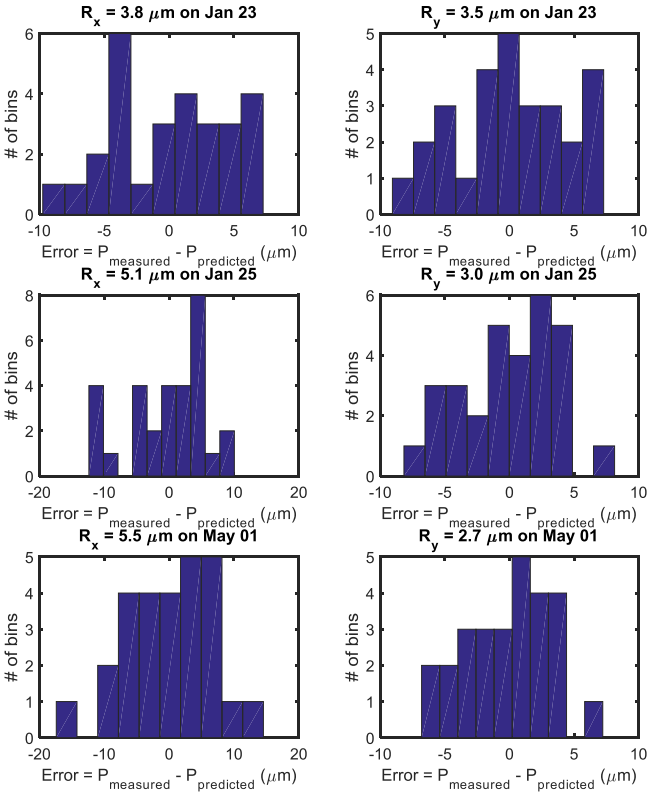

Figure 6.14 Summary of resolution on January 23 and 25 and May 01, 2015 based on three methods: PLS, SVD, ANN (a, b, c). PLS method suggests best resolution with below 2 µm in y and below 4 µm in x. All three methods give below ~5 µm resolution.

It should be noted that the resolution was evaluated with a beam position range of 2 by 2 mm^2 (Figure 6.5 (a)). Therefore the resolution obtained is an averaged value within the range in contrast to the beam jitter data normally used for the calibration of a standard BPM.

In summary, a resolution of ~ 5 μm has been achieved over a period of three months in 2015. I used three methods to extract the beam position, namely ANN, SVD and PLS. The latter yielded the best resolution and minimum computation time.

6.2. Dipole Modes induced by Beam Trajectory Angle

6.2.1. Dipole mode excitation

The dipole modes radiated to the HOM ports can be caused by a combination of bunch transverse offset y, bunch tilt α, and bunch trajectory angle θ with respect to the cavity axis [6] as illustrated in Figure 6.15:

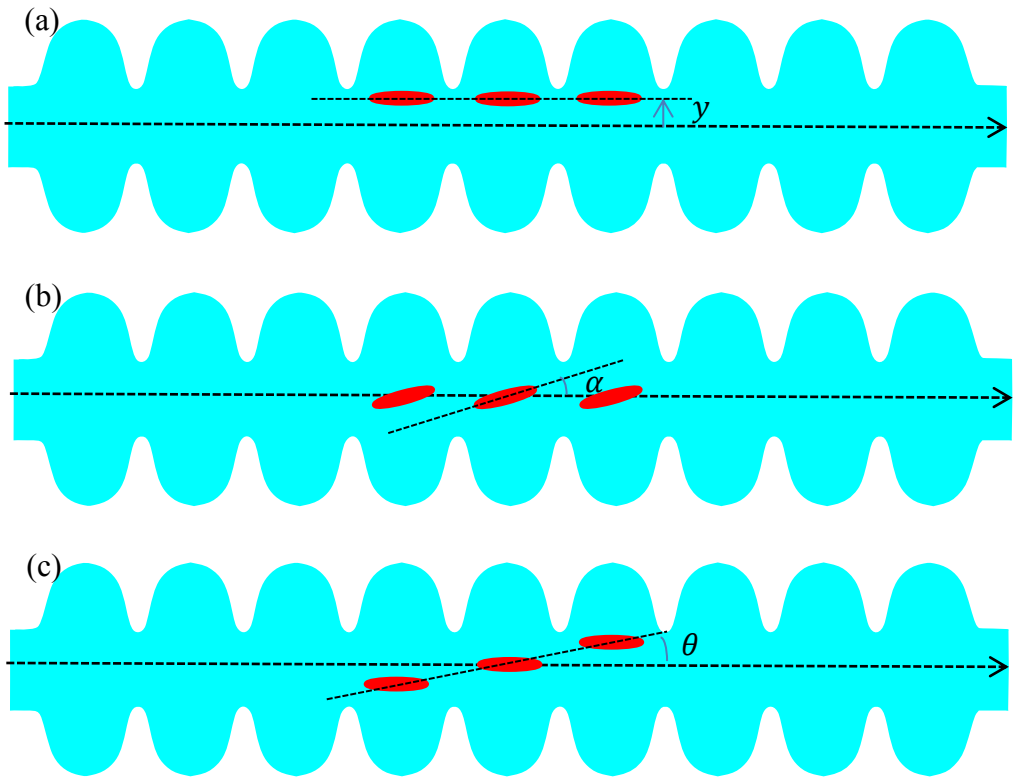

Figure 6.15 Three scenarios of a bunch traveling through a cavity: (a) the bunch travels with an offset, (b) the bunch is tilted and (c) the bunch travels with an angle with respect to cavity axis.

The corresponding signal voltages have the following dependence [70]:

$$V_y \propto y e^{-\frac{t}{2\tau}} \sin(\omega t), \tag{6.11}$$

$$V_\alpha \propto -\alpha e^{-\frac{t}{2\tau}} \cos(\omega t), \tag{6.12}$$

$$V_\theta \propto \theta e^{-\frac{t}{2\tau}} \cos(\omega t), \tag{6.13}$$

where $\tau = Q_L/\omega$ is the decay constant. Normally the contribution from bunch tilt to the signal strength is vanishingly small [6] compared with beam offset signal at FLASH and E-XFEL due to the ultrashort bunches (hundred femtoseconds). The contribution of the wakefield from bunch trajectory angle is not negligible in several cases [6], [51]. Therefore the following discussion will focus on this contribution.

6.2.2. Angle effects based on eigenmode expansion

Based on the method described in Appendix A, the amplitude evolution of a mode can be described in time as a harmonic oscillator by equations A.13 and A.14 for various bunch trajectories.

The field distribution of eigenmode TE111-6 is solved for an ideal TESLA cavity with the computer codes CST®. Equations A.13 and A.14 are then solved numerically for various beam offsets and angles. The beam offset was varied from 0 to 35 mm with a step of 1 mm. The amplitude dependence on the beam offset y is shown in Figure 6.16. The beam angle θ was varied from 0 rad to 23.1 mrad with a step of 1.1 mrad. The amplitude dependence on the beam angle θ is shown in Figure 6.17.

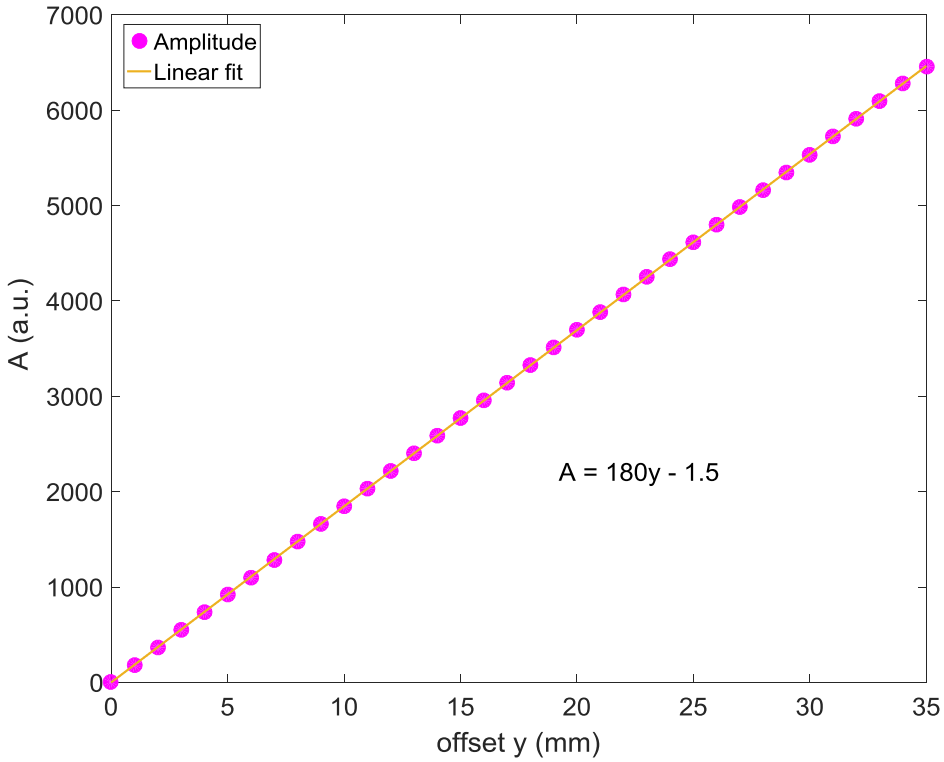

Figure 6.16 Dependence of amplitude A on the beam offset y for mode TE111-6 of a TESLA cavity

By linear fit, one obtains the following amplitude A dependence on the beam offset y: $A = 180y - 1.5$. Similarly, performing a linear fit to the amplitude versus angle θ is shown in Figure 6.17 and $A = 3.9 \times 10^4\theta - 1.9$.

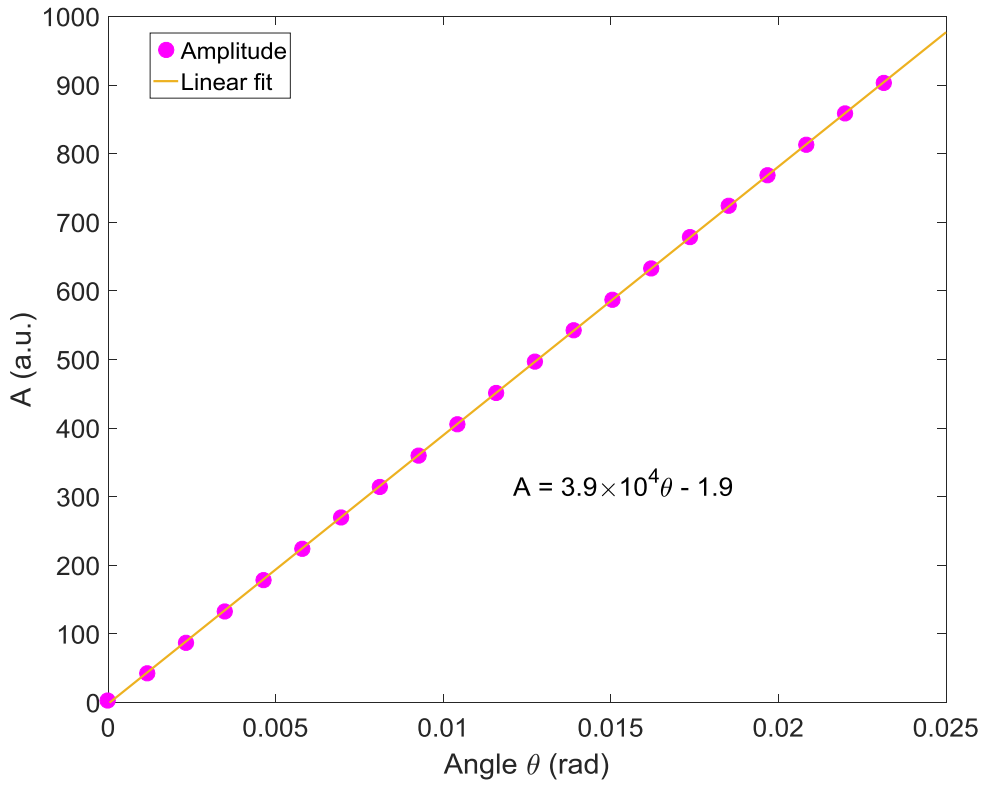

Figure 6.17 Dependence of amplitude A on the angular offset of the beam θ for mode TE111-6 of a TESLA cavity

From here I deduce that the amplitude of a signal produced by a point charge travelling with an angle of 1 mrad is the same as the one travelling with approximately 200 μm offset. This is different than predicted in [6], that a 1 mrad signal has the same amplitude as a 100 μm offset signal. The difference is due to the fact that the angle effect is estimated for a single cell in [6]. The beam trajectory angle θ with respect to the BPM reference evaluated by BPM reading in previous sections is in the range of 100-200 μrad during the measurements, which corresponds to 20-40 μm in terms of offsets. This adds ambiguity to the beam position determination. This is difficult to eliminate because the beam angle excites the mode with the same frequency as the beam offset.

It was observed in Chapter 4 that the dipole mode frequencies vary with a few kHz over time. This is not an issue for our present application because in the calibration and validation parts, the effects caused by this variation were contained in the analysis. In our present system the sampling step (~50 kHz) is insufficient to resolve the mode frequency variation.

In summary, the principle of a HOMBPM and the procedure of calibration and validation have been presented. By working in frequency domain and discarding the phase information, the system delivers a resolution below 5 μm over a 2 mm by 2 mm range stably over a three-month period. The beam angle contributes a few tens μm to the calibration and validation RMS error depending on the beam actual trajectory angle. Based on the simulation it shows that 1 mrad angle is equivalent to ~200 μm in terms of the amplitude of the induced dipole signal.

For the HOMBPM system now being built for the 1.3 GHz cavities at the E-XFEL, a directly sampling technique will be utilized [8]. This avoids the issue from LO. Instead of using directly the charge value measured by toroids, the monopole signal can be used for normalization. In this respect, the performance of HOMBPM may be improved. The HOMBPhM will be integrated with HOMBPM onto the same electronics in order to make the whole system compact and economical.

The HOMBPMs for the 3.9 GHz cavities at the E-XFEL have been designed [55] similar to the system at FLASH [7]. The modal spectra presented in Chapter 4 can be used to finely tune the filters for the electronics. Future work in this area will be focused on testing the associated electronics with beam and commissioning at the E-XFEL.

Chapter 7 - Conclusions

In this thesis, I have investigated the beam instrumentation of higher order modes for 1.3 and 3.9 GHz accelerating cavities at the E-XFEL. The accelerating cavities are used as beam pickups for beam phase and position monitoring. This novel method is non-invasive and economical. The phase of the accelerating field directly influences the quality of the electron beam. One main part of my thesis is to explore the beam phase measurement based on the beam-excited higher order modes in 1.3 GHz cavities. In particular, I investigated the beam phase monitoring with a coupled circuit model and an experimental setup expressly developed for this purpose. The necessary algorithms have been developed and the ways to improve the resolution have been identified. The other part of the thesis concerns HOM-based beam position monitoring for 1.3 and 3.9 GHz cavities. Both types of HOMBPMs installed at FLASH are subject to a drift in calibration. I focused on the HOMBPMs for 1.3 GHz cavities. I demonstrated for the first time a stability of the calibration over several months by implementing complex signal processing and data mining techniques. A study in view of the HOMBPMs for 3.9 GHz cavities at the E-XFEL was mainly focused on the understanding of the HOM spectra of the eight coupled cavities. Therefore extensive measurements and characterization work has been done in this respect.

7.1. Summary

Among the beam-excited higher order modes, the monopole modes depend only on the charge of the excitation bunch, but not on the offset. This property makes them suitable candidates for the beam phase measurement. The dipole modes depend on the beam charge and offset. Therefore by normalizing the dipole signal with respect to charge, the beam offset can be determined.

7.1.1. HOM-based phase measurement studies

A proof of principle of HOM-based beam phase measurements for 1.3 GHz cavities has been previously demonstrated. I built on this initial concept to provide a reliable

phase measurement. This is the first monitor that can directly deliver the beam phase with respect to the accelerating field inside a cavity. I first used a coupled circuit model (Chapter 3) to aid the development of the beam phase monitor and investigate the means to improve its performance. The circuit model quantifies the dependence of the resolution of the beam phase determination on the SNR and the sampling frequency. I proposed and fully implemented a fast scope based experimental system that is able to be integrated into the accelerator control system. Measurements have been made at both FLASH and the European XFEL. For a bunch charge of 0.5 nC and accelerating gradient of 20 MV/m, the obtained resolution is approximately 0.1° (Chapter 5) which is limited by the signal power. With an amplified signal power, the best resolution observed was 0.03°. The dedicated electronics under design can improve the SNR by amplifying the signal strength and limiting the noise level and hence the resolution is expected to be improved to meet 0.01° resolution.

The dependence of the resolution on the bunch charge was studied experimentally. The resolution obtained is consistent with the results from my circuit model. The experimental results are also found to be consistent with the phase readouts from the LLRF system (see Chapter 5). The theoretical resolution limit is estimated to be 6×10^{-8} degree, which is several orders of magnitude smaller than the required (0.01°). The measured resolution is mainly limited by SNR. Therefore there is an opportunity to improve the resolution. Since the monitor delivers the beam phase directly with respect to the accelerating field, and is insensitive to the drifts of the trigger, it can be used for long term RF drift monitoring, which can provide diagnostic information to the current LLRF system. Also it is capable to decouple the phase jitter from the injector 1.3 GHz module, the gun or the 3.9 GHz module so that it is expected to largely improve the long term performance.

7.1.2. HOM-based beam position monitoring studies

My HOMBPM study is focused on means to improve the system stability over time. This is an issue of the HOMBPM system at FLASH, for both the 1.3 and 3.9 GHz cavities. This problem may also occur at the systems at the E-XFEL.

I looked for a cure of the instability of the HOMBPM for the 1.3 GHz cavities at FLASH by investigating different signal processing and data mining techniques. A resolution below 5 μm was demonstrated over a period of several months. Three methods were used, namely, PLS, SVD, and ANN, to extract the beam position. The resolutions found by three methods are consistent with each other. The PLS method was found to give the best resolution, with less computation power. However, with modern digital processors or FPGAs, the computation power needed for either method should not be of concern.

The study of the HOMBPM for the 3.9 GHz cavities at the E-XFEL focused on the measurements and characterization of the HOM spectra of the eight coupled cavities due to the limited experience with such a system. The simulation of eigenmodes for such an electrical large structure is quite demanding, not to mention the quantification of the influence of fabrication errors on the spectra. Therefore I have measured the HOM spectra of single as well as coupled cavities. The bands to be used for the HOMBPM are selected to be around 5440 MHz (propagating modes in the 2^{nd} dipole band) to monitor the beam position in a cryomodule and 9040 MHz (trapped modes in the 5^{th} dipole band) to monitor the beam position in each cavity.

The HOMBPM system can also give other valuable information. It can be used to detect the cavity misalignment inside the cryomodule, which is important to prove that all cavities are still positioned within the required alignment tolerance. The system could also be used to find the beam orbit that minimizes the transverse kick from wakefields. These application scenarios are independent of the instability issue aforementioned.

7.2. Outlook

Based on the extensive measurements at FLASH and the E-XFEL, the electronics for the HOM-based beam diagnostic system have been designed and prototypes are now being built and tested. These include the electronics of HOMBPhM and HOMBPM for the 1.3 GHz cavities and the electronics of HOMBPM for the 3.9 GHz cavities.

Future work on the characterization of the prototype electronics with beam is planned. Its impact on the LLRF performance needs to be studied. Various aforementioned application scenarios can be experimentally explored.

For the 3.9 GHz cavities, based on the experience with the HOMBPM system at FLASH, the beam-based tuning of the electronics is essential for the reliable operation. Also the developed algorithms have to be implemented in the control system. A study on the possibility to monitor the beam phase in 3.9 GHz cavities is also worth investigation.

With the momentum of HOM-based beam diagnostics, further investigations could be made on the use of other higher order modes such as quadrupole modes for beam distribution prediction [80].

Bibliography

[1] K. Honkavaara, B. Faatz, J. Feldhaus, S. Schreiber, R. Treusch, *et al.*, "FLASH: First Soft X-ray FEL Operating Two Undulator Beamlines simultaneously," in *Proceedings of FEL2014*, Basel, 2014, p. 635.

[2] R. Abela, A. Aghababyan, M. Altarelli, C. Altucci, G. Amatuni, *et al.*, "The European X-Ray Free-Electron Laser: Technical Design Report," Hamburg, DESY Report, DESY 2006-097, 2007.

[3] R. M. Jones, "Wakefield Suppression in High Gradient Linacs for Lepton Linear Colliders," *Phys. Rev. Spec. Top. - Accel. Beams*, vol. 12, no. 10, p. 104801, 2009.

[4] A. W. Chao, Physics of Collective Beam Instabilities in High Energy Accelerators. Wiley, 1993.

[5] R. E. Shafer, "Beam Position Monitoring," in *Proceedings of AIP Conf.*, 1989, vol. 212, p. 26.

[6] S. Molloy, J. Frisch, D. McCormick, J. May, M. Ross, *et al.*, "High Precision Superconducting Cavity Diagnostics with Higher Order Mode Measurements," *Phys. Rev. Spec. Top. - Accel. Beams*, vol. 9, no. 11, p. 112802, 2006.

[7] P. Zhang, "Beam Diagnostics in Superconducting Accelerating Cavities," Ph.D. Thesis, Springer International Publishing, 2013.

[8] S. B. Habib, H. Schlarb, N. Baboi, and A. Abramowicz, "New Design of High Order Modes Electronics in MTCA.4 Standard for FLASH and the European XFEL," in *Proceedings of IBIC13*, Oxford, UK, 2013, p. 443.

[9] N. Joshi, N. Baboi, R. Jones, and L. Shi, "Simulation of Electromagnetic Scattering Through the E-XFEL Third Harmonic Cavity Module," in *Proceedings of IPAC16*, Busan, Korea, 2016, p. 3001.

[10] A. Brandt, "Development of a Finite State Machine for the Automated Operation of the LLRF Control at FLASH," Ph.D. Thesis, Hamburg University, 2007.

[11] T. P. Wangler, RF Linear Accelerators, 2nd ed. Weinheim: Wiley-VCH, 2008.

[12] P. Schmüser, M. Dohlus, and J. Rossbach, Ultraviolet and Soft X-Ray Free-Electron Lasers, vol. 229. Springer Berlin Heidelberg, 2009.

[13] B. Aune, R. Bandelmann, D. Bloess, B. Bonin, A. Bosotti, *et al.*, "Superconducting TESLA Cavities," *Phys. Rev. Spec. Top. - Accel. Beams*, vol. 3, no. 9, p. 092001, 2000.

[14] E. Schneidmiller and M. Yurkov, "An Overview of the Radiation Properties of the European XFEL," in *Proceedings of FEL14*, Basel, Switzerland, 2014, p. 204.

[15] "Technical Information about the XFEL Project." http://xfel.desy.de/technical_information.

[16] P. Pierini, M. Bertucci, A. Bosotti, C. Maiano, P. Michelato, *et al.*, "European XFEL 3.9 GHz System," in *Proceedings of SRF13*, Paris, France, 2013, p. 100.

[17] E. Vogel, E. Harms, H. Edwards, K. Jensch, T. Khabiboulline, *et al.*, "Considerations on the Third Harmonic RF of the European XFEL.," in *Proceedings of SRF07*, Beijing, China, p. 481.

[18] S. Schreiber, "The TESLA Linear Collider Project," *Int. J. Mod. Phys. A*, vol. 13, no. 14, p. 2431, 1998.

[19] H. Edwards and E. Harms, "3.9 GHz Cavity Module for Linear Bunch Compression at FLASH," in *Proceedings of LINAC10*, Tsukuba, Japan, 2010, p. 41.

[20] M. Vogt, J. Feldhaus, K. Honkavaara, J. Rönsch-Schulenburg, S. Schreiber, *et al.*, "The Superconducting Soft X-Ray Free-Electron Laser User Facility FLASH," in *Proceedings of IPAC16*, Busan, Korea, 2016, p. 729.

[21] T. Wamsat and N. Baboi, "First Tests of a Micro-TCA-Based Downconverter Electronics for 5GHz Higher Order Modes in Third Harmonic Accelerating Cavities at the XFEL," in *Proceedings of IBIC14*, Monterey, CA, USA, 2014, p. 337.

[22] A. Kuramoto, N. Baboi, and H. Hayano, "Measurements of Cavity Misalignment by Beam Induced HOM Excited in 9-cell Superconducting Cavities," in *Proceedings of LINAC2014,* Geneva, Switzerland, 2014, p. 370.

[23] R. Flükiger, "Overview of Superconductivity and Challenges in Applications," *Rev. Accel. Sci. Technol.*, vol. 05, p. 1, 2012.

[24] H. Padamsee, J. Knobloch, and Tomas Hays, RF Superconductivity for Accelerators, 2nd ed. Weinheim: Wiley-VCH, 2008.

[25] R. L. Geng, G. V. Eremeev, H. Padamsee, and V. D. Shemelin, "High Gradient Studies for ILC with Single-cell Re-entrant Shape and Elliptical Shape Cavities made of Fine-grain and Large-grain Niobium," in *Proceedings of PAC2007*, New Mexico, USA, 2007, p. 2337.

[26] R. L. Geng, "Review of New Shapes for Higher Gradients," *Phys. C Supercond.*, vol. 441, p. 145, 2006.

[27] R. L. Geng, "Overview of ILC High Gradient Cavity R&D at Jefferson Lab," in *Proceedings of SRF2011*, Chicago, IL USA, 2011, p. 74.

[28] H. Padamsee, RF Superconductivity: Science, Technology, and Applications. Weinheim: Wiley-VCH, 2009.

[29] E. U. Condon, "Forced Oscillations in Cavity Resonators," *J. Appl. Phys.*, vol. 12, no. 2, p. 129, 1941.

[30] T. Weiland and R. Wanzenberg, "Wake fields and Impedances," in *Frontiers of Particle Beams: Intensity Limitations*, Springer Berlin Heidelberg, 1992, p. 39.

[31] T. Khabibouline, N. Solyak, and R. Wanzenberg, "Higher Order Modes of a 3rd Harmonic Cavity with an Increased End-cup Iris," TESLA-FEL, TESLA-FEL 2003-01, 2003.

[32] H. Weise, "How to Produce 100 Superconducting Modules for the European XFEL in Collaboration and with Industry," in *Proceedings of IPAC14*, Dresden, Germany, p.1923, 2014.

[33] P. Pierini, A. Bosotti, N. Panzeri, D. Sertore, J. Iversen, *et al.*, "Third Harmonic Superconducting Cavity Prototypes for the XFEL," in *Proceedings of of LINAC08*, Victoria, BC, Canada, 2008, p. 821.

[34] P. B. Wilson, "Introduction to Wakefields and Wake Potentials," AIP, Batavia Illinois, USPAS School, SLAC-PUB-4547, 1989.

[35] R. Wanzenberg, "Monopole, Dipole and Quadrupole Passbands of the TESLA 9-cell Cavity," Hamburg, DESY Report, TESLA 2001-33, 2001.

[36] W. K. H. Panofsky and W. A. Wenzel, “Some Considerations Concerning the Transverse Deflection of Charged Particles in Radio-Frequency Fields,” *Rev. Sci. Instrum.*, vol. 27, no. 11, p. 967, 1956.

[37] “CST.” https://www.cst.com/.

[38] C. Adolphsen, K. Bane, G. A. Loew, R. Ruth, K. Thompson, *et al.*, “Measurements of Wakefields Generated in Accelerator Test Structures Using the SLC,” SLAC-PUB-5941, 1992.

[39] N. Baboi, R. M. Jones, J. R. Lewandowski, G. B. Bowden, S. G. Tantawi, *et al.*, “Wire Measurement of Impedance of an X-band Accelerating Structure,” in *Proceedings of LINAC2004,* Lubeck, Germany, 2004, p. 165.

[40] D. M. Pozar, Microwave Engineering, 4th ed. Hoboken, NJ: John Wiley & Sons, 2012.

[41] T. Shintake, “Analysis of the Transient Response in Periodic Structures based on a Coupled-Resonator Model,” in *Proceedings of Course Conference C96-09-09.3*, 1996, p. 435.

[42] R. M. Jones, V. A. Dolgashev, and J. W. Wang, “Dispersion and Energy Compensation in High-gradient Linacs for Lepton Colliders,” *Phys. Rev. Spec. Top. - Accel. Beams*, vol. 12, no. 5, p. 051001, 2009.

[43] D. E. Nagle, E. A. Knapp, and B. C. Knapp, “Coupled Resonator Model for Standing Wave Accelerator Tanks,” *Rev. Sci. Instrum.*, vol. 38, no. 11, p. 1583, 1967.

[44] B. Szczesny, I. R. R. Shinton, and R. M. Jones, “Third Harmonic Cavity Modal Analysis,” in *Proceedings of SRF09*, Berlin, Germany, 2009, p. 599.

[45] K. L. Bane and R. L. Gluckstern, “The Transverse Wakefield of a Detuned X Band Accelerator Structure,” *Part. Accel.*, vol. 42, p. 123, 1992.

[46] R. M. Jones, C. E. Adolphsen, J. W. Wang, and Z. Li, “Wakefield Damping in a pair of X-band Accelerators for Linear Colliders,” *Phys. Rev. Spec. Top.-Accel. Beams*, vol. 9, no. 10, p. 102001, 2006.

[47] “TESLA Technology Collaboration-Cavity Database.” http://tesla-new.desy.de/.

[48] “European XFEL Cavity Database.” http://xfel.desy.de/cavity_database/.

[49] A. Sulimov, J. Iversen, D. Kostin, W.-D. Moeller, D. Reschke, *et al.*, “Efficiency of High Order Modes Extraction in the European XFEL LINAC,” in *Proceedings of LINAC2014,* Geneva, 2014, p. 883.

[50] S. S. M. Wong, Computational Methods in Physics and Engineering, 2nd ed. World Scientific Publishing Company, 1997.

[51] J. Frisch, N. Baboi, N. Eddy, S. Nagaitsev, O. Hensler, *et al.*, “Electronics and Algorithms for HOM Based Beam Diagnostics,” in *Proceedings of Beam Instrumentation Workshop 2006*, 2006, p. 313.

[52] P. Zhang, N. Baboi, and R. M. Jones, “Higher Order Mode Spectra and the Dependence of Localized Dipole Modes on the Transverse Beam Position in Third Harmonic Superconducting Cavities at FLASH,” DESY Report, DESY 12-109, 2012.

[53] L. Shi, N. Baboi, and R. M. Jones, “Measurements and Characterization of Higher Order Modes for the 3.9 GHz cavities at the European-XFEL,” To be published, DESY Report, 2017.

[54] C. Maiano, M. Bertucci, and A. Bosotti, “Status of the Fabrication of the XFEL 3.9 GHz Cavity Series,” in *Proceedings of IPAC2014,* Dresden, Germany, 2014, p. 2512.

[55] T. Wamsat and N. Baboi, “First Tests of a MICRO-TCA-Based Downconverter Electronics for 5GHz Higher Order Modes in Third Harmonic Accelerating Cavities at the XFEL,” in *Proceedings of IBIC14*, Monterey, CA, USA, 2014, p. 337.

[56] T. Flisgen, J. Heller, T. Galek, L. Shi, N. Joshi, *et al.*, “Compendium of Resonant Modes in the Chain of Third Harmonic TESLA Cavities for the European XFEL,” *Phys. Rev. Accel. Beams*, vol.20, no. 4, p.042002, 2017.

[57] I. R. R. Shinton and N. Juntong, “Compendium of Eigenmodes in Third Harmonic Cavities for FLASH and the XFEL,” DESY Report, DESY-12-053, 2012.

[58] C. Schmidt, “RF System Modelling and Controller Design for the European XFEL,” Ph.D. Thesis, Hamburg University of Technology, 2011.

[59] C. Schmidt, “Performance of the MICROTCA.4 based LLRF System at FLASH,” in *Proceedings of IPAC2014,* Dresden, Germany, 2014, p. 2433.

[60] J. Branlard, G. Ayvazyan, M. Grecki, and M. Hoffmann, “The European XFEL LLRF System,” in *Proceedings of IPAC12,* New Orleans, 2012, p. 55.

[61] S. Pfeiffer, C. Schmidt, Marie Kristin Bock, H. Schlarb, and W. Jalmuzna, “Fast Feedback Strategies for Longitudinal Beam Stabilization,” in *Proceedings of IPAC12,* New Orleans, USA, 2012, p. 26.

[62] M. Caselle, M. Brosi, S. Chilingaryan, T. Dritschler, H. Hiller, *et al.*, “A Picosecond Sampling Electronic ‘KAPTURE’ for Terahertz Synchrotron Radiation,” in *Proceedings of IBIC14*, Monterey, CA, USA, 2014, p. 24.

[63] C. Schmidt, “Recent Developments of the European XFEL LLRF System,” in *Proceedings of IPAC2013*, Shanghai, China, 2013, p. 2941.

[64] S. Goloborodko, “DOOCS: an Object Oriented Control System as the integrating part for the TTF Linac,” in *Proceedings of ICALEPCS*, Beijing, China, 1997.

[65] T. Schilcher, “Vector Sum Control of Pulsed Accelerating Fields in Lorentz Force Detuned Superconducting Cavities,” Ph.D. Thesis, Hamburg University, 1998.

[66] W. van Etten, Introduction to Random Signals and Noise. Chichester, England ; Hoboken, NJ: Wiley, 2005.

[67] K. Rehlich, “Status of the FLASH Free Electron Laser Control System,” in *Proceedings of ICALEPCS*, Knoxville, Tennessee, USA, 2007, vol. 7, p. 53.

[68] A. Agababyan, G. Grygiel, O. Hensler, R. Kammering, V. Kocharyan, *et al.*, “Evolution of the FLASH DAQ System,” in *Proceedings of ICALEPCS2009*, Kobe, Japan, 2009, p. 37.

[69] L. Shi, R. M. Jones., and N. Baboi, “Stability Study of the Higher Order Mode Beam Position Monitors at the Accelerating Cavities at FLASH,” in *Proceedings of IBIC14*, Monterey, CA, USA, 2014, p. 327.

[70] S. Walston, S. Boogert, C. Chung, P. Fitsos, J. Frisch, *et al.*, “Performance of a High Resolution Cavity Beam Position Monitor System,” *Nucl.Instrum.Meth.*, vol. A578, p. 1, 2007.

[71] R. Rosipal and N. Krämer, “Overview and Recent Advances in Partial Least Squares,” in *Subspace, Latent Structure and Feature Selection*, C. Saunders, M. Grobelnik, S. Gunn, and J. Shawe-Taylor, Eds. Springer Berlin Heidelberg, 2006, p. 34.

[72] R. Battiti, “First and Second-Order Methods for Learning: between Steepest Descent and Newton’s Method,” *Neural Comput.*, vol. 4, p. 141, 1992.

[73] S. S. Haykin, Neural Networks and Learning Machines. Prentice Hall, 2009.

[74] P. Zhang, N. Baboi, and R. M. Jones, “Statistical Methods for Transverse Beam Position Diagnostics with Higher Order Modes in Third Harmonic 3.9GHz Superconducting Accelerating Cavities at FLASH,” *Nucl.Instrum.Meth.*, vol. A734, p. 84, 2014.

[75] L. Shi, N. Baboi, and R. M. Jones, “Stability and Resolution Studies of HOMBPMs for the 1.3 GHz Superconducting Accelerating Cavities at FLASH,” *Phys.Procedia*, vol. 77, p. 42, 2015.

[76] H. Anton and C. Rorres, Elementary Linear Algebra: Applications Version, 10th ed. Hoboken, NJ: Wiley, 2010.

[77] I. Narsky and F. C. Porter, Statistical Analysis Techniques in Particle Physics: Fits, Density Estimation and Supervised Learning, 1st ed. Wiley-VCH Verlag GmbH & Co. KGaA, 2013.

[78] S. O. Haykin, Neural Networks and Learning Machines, 3 edition. New York: Prentice Hall, 2008.

[79] C. M. Bishop, Pattern Recognition and Machine Learning. Springer, 2006.

[80] N. Barov, J. S. Kim, A. W. Weidemann, R. H. Miller, and C. D. Nantista, “High-Precision Resonant Cavity Beam Position, Emittance and Third-moment Monitors,” in *Proceedings of the PAC2005*, Knoxville, Tennessee, USA, 2005, p. 4311.

[81] S. de Jong, “SIMPLS: An alternative Approach to Partial Least Squares Regression,” *Chemom. Intell. Lab. Syst.*, vol. 18, no. 3, p. 251, 1993.

[82] L. A. Zadeh and C. A, Desoer, Linear System Theory: The State Space Approach. New York: McGraw-Hill, 1963.

[83] R. M. Jones, “Wakefields and Collective Effects,” Cockcroft Institute, Lecture Notes, 2015.

Appendix A. Condon Method

Condon [29] stated that an arbitrary electromagnetic field inside a closed resonator which satisfies the boundary conditions can be expanded in terms of resonant wave patterns (modes). The method is reviewed first and then used for the evaluation of angular wakefields.

A1. Condon Method

The following derivation is based on Condon [29], and Bane [45]. The electric field $\boldsymbol{E}$ and magnetic field $\boldsymbol{H}$ are expanded in terms of orthogonal eigen-functions $\boldsymbol{e}^{(m)}(x,y,z)$ and $\boldsymbol{h}^{(m)}(x,y,z)$:

$$\boldsymbol{E}(x,y,z,t) = Re\left\{\sum_m q^{(m)}(t)\boldsymbol{e}^{(m)}(x,y,z)\right\}, \tag{A.1}$$

$$\boldsymbol{H}(x,y,z,t) = Re\left\{\sum_m p^{(m)}(t)\boldsymbol{h}^{(m)}(x,y,z)\right\}, \tag{A.2}$$

where $\boldsymbol{e}^{(m)}(x,y,z)$ and $\boldsymbol{h}^{(m)}(x,y,z)$ are the field distributions of eigenmode normalized with the energy stored in the mode:

$$\int \boldsymbol{e}^{(m)} \cdot \boldsymbol{e}^{(n)}\, dV = \delta_{mn}, \tag{A.3}$$

$$\int \boldsymbol{h}^{(m)} \cdot \boldsymbol{h}^{(n)}\, dV = \delta_{mn}. \tag{A.4}$$

where $\delta_{mn}$is the Kronecker delta function.

The Maxwell Equation (Ampère's law) in vacuum with current source:

$$\nabla \times \boldsymbol{H} = \boldsymbol{J} + \epsilon_0 \frac{\partial \boldsymbol{E}}{\partial t}, \tag{A.5}$$

can be written based on equations A.1 and A.2 as:

$$\nabla \times \sum_m p^{(m)} \boldsymbol{h}^{(m)} = \boldsymbol{J} + \epsilon_0 \frac{\partial}{\partial t}\left(\sum_m q^{(m)} \boldsymbol{e}^{(m)}\right). \quad \text{A.6}$$

By multiplying $\boldsymbol{e}^{(m)}$ on both sides of equation A.6 and then integrating over the cavity volume, one obtains:

$$\frac{\omega_m}{c} p^{(m)}(t) = \epsilon_0 \frac{d}{dt} q^{(m)}(t) + \int_V \boldsymbol{J} \cdot \boldsymbol{e}^{(m)} dV. \quad \text{A.7}$$

The relation $\nabla \times \boldsymbol{h}^{(m)} = \frac{\omega_m}{c} \boldsymbol{e}^{(m)}$ is used. Based on the Maxwell equation (Faraday's law):

$$\nabla \times \boldsymbol{E} = -\mu_0 \frac{\partial \boldsymbol{H}}{\partial t}, \quad \text{A.8}$$

the following equation can be obtained by using the relation $\nabla \times \boldsymbol{e}^{(m)} = \frac{\omega_m}{c} \boldsymbol{h}^{(m)}$:

$$\frac{\omega_m}{c} q^{(m)}(t) + \mu_0 \frac{d}{dt} p^{(m)}(t) = 0. \quad \text{A.9}$$

From the equations A.7 and A.9, $p^{(m)}(t)$ can be decoupled from $q^{(m)}(t)$ to obtain a second order differential equation of $q^{(m)}(t)$:

$$\left(\frac{d^2}{dt^2}+\omega_m^2\right)q^{(m)}(t)=-\frac{1}{\epsilon_0}\frac{d}{dt}\left(\int_V \boldsymbol{J}\cdot\boldsymbol{e}^{(m)}dV\right). \quad \text{A.10}$$

The equation A.10 dictates the amplitude evolution over time of mode m.

A2. Mode Amplitude Evolution for various Beam Trajectories

There is no restriction on the trajectory of the current source $\boldsymbol{J}$ in equation A.10. Assuming a charge moving with trajectory of $(x_0(t), y_0(t), z_0(t))$ and density $\rho(x,y,z,t)=Q\delta(z-z_0)\delta(x-x_0)\delta(y-y_0)$, the current source then can be written as:

$$\boldsymbol{J}=\rho c\boldsymbol{r}, \quad \text{A.11}$$

where $\boldsymbol{r}$ is the unit instant direction vector along the trajectory. By substituting A.11 for A.10, the amplitude $q(t)$ can be solved.

$$\left(\frac{d^2}{dt^2}+\omega_m^2\right)q^{(m)}(t)=-\frac{Qc}{\epsilon_0}\frac{d}{dt}\left(\boldsymbol{e}^{(m)}(x_0,y_0,z_0)\cdot\boldsymbol{r}\right). \quad \text{A.12}$$

Two scenarios are considered here:

1. The charge travels in parallel to the cavity axis $\boldsymbol{z}$:

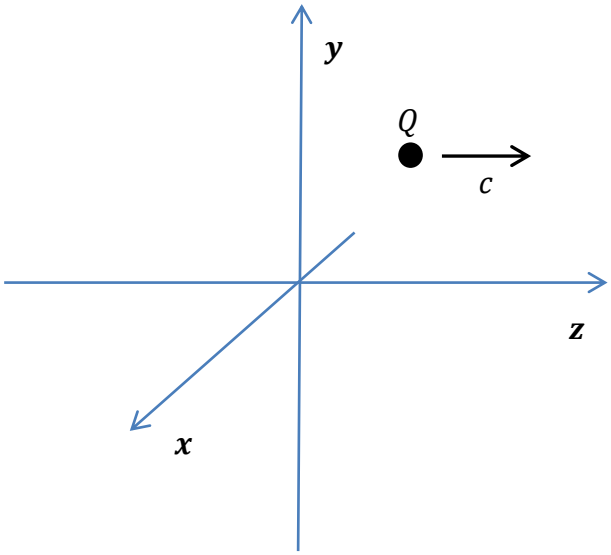

Figure A.1 A point charge travels in parallel with the cavity axis z

$$\left(\frac{d^2}{dt^2}+\omega_m^2\right)q^{(m)}(t)=-\frac{Qc}{\epsilon_0}\frac{d}{dt}\left(\boldsymbol{e}^{(m)}(x_0,y_0,z_0+ct)\cdot\boldsymbol{z}\right). \qquad \text{A.13}$$

2. The charge travels at an angle to the cavity axis $\boldsymbol{z}$:

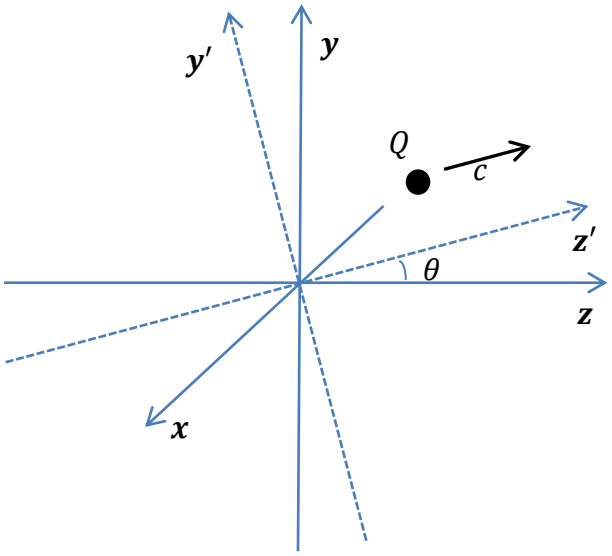

Figure A.2 A point charge travels at an angle θ to the cavity axis z

$$\left(\frac{d^2}{dt^2}+\omega_m^2\right)q^{(m)}(t)=-\frac{Qc}{\epsilon_0}\frac{d}{dt}\left(\boldsymbol{e}^{(m)}(x_0,y_0+ct\sin\theta,z_0+ct\cos\theta)\boldsymbol{z}'\right)$$

$$=-\frac{Qc}{\epsilon_0}\frac{d}{dt}\left(\boldsymbol{e}^{(m)}(x_0,y_0+ct\sin\theta,z_0+ct\cos\theta)(\boldsymbol{y}\sin\theta+\boldsymbol{z}\cos\theta)\right). \quad \text{A.14}$$

The eigenmode field $\boldsymbol{e}^{(m)}$ can be obtained from any 3D eigenmode field solver. The equations A.13 and A.14 can be solved numerically.

Appendix B. Data Analysis Techniques

This is a collection of signal processing techniques used throughout the thesis.

B1. Singular Value Decomposition

Singular value decomposition (SVD) is used to lower the dimensions required for data analysis while retaining most of the information in a matrix.

A $m \times n$ real matrix A can be decomposed as:

$$\begin{aligned} A &= U \cdot S \cdot V^T, \\ U &= [u_1, u_2, \dots u_m], \\ S &= diag(s_{11}, s_{22}, \dots, s_{kk}), k \leq \min(m, n), \\ V^T &= [v_1, v_2, \dots v_n], \end{aligned} \quad \text{B.1}$$

where U is a $m \times m$ matrix with orthonormal columns u_m. S is a $m \times n$ diagonal matrix. The diagonal elements are sorted in descending order and are called singular values. V is a $n \times n$ matrix with orthonormal columns v_n. V^T is the transpose of V.

If matrix A is decomposed as in B.1, it can be reconstructed with:

$$A_k = \sum_{i=1}^{k} s_{ii} \cdot u_i \cdot v_i^T, k \leq rank(A). \quad \text{B.2}$$

Equation B.2 is a rank k approximation to the matrix A. It can be proved that the 2-norm distance[16] between the original and reconstructed matrices is given by:

$$\|A - A_k\| = s_{k+1}. \tag{B.3}$$

Equation B.3 guarantees that A_k is an optimized approximation to A in the least square sense.

B2. Linear Regression and PLS – Partial Least Square

X is a $n \times m$ predictor matrix with the form $X = [x_1\ x_2 \dots x_m]$, which contains m predictors and n observations or measurements. The response variable Y contains only one variable and n observations or measurements. Linear regression models the relation between X and Y as:

$$y = \beta_0 + \beta_1 x_1 + \cdots + \epsilon, \tag{B.4}$$

where β_0 is the intercept term and ϵ is the error term. The error may come from effects of other variables and the measurement imperfections.

The regression coefficients in B.4 can be obtained in a least square sense:

$$\beta = V^{-1} cov(X, Y), \tag{B.5}$$

where V is the covariance matrix of X, i.e. $v_{ij} = cov(x_i, x_j)$ and $cov(X, Y)$ the vector of covariances between X and Y and β contains the coefficient β_i in B.4.

[16] The 2-norm distance is defined as the root mean square sum of each element in matrix $A - A_k$

Once the coefficient β is obtained, the model is ready to make predictions. In the ideal case, the prediction error $Y - \beta \cdot X$ will be uncorrelated with the predictor variable x_i.

If predictors in X are correlated, the number of predictors can be reduced. Partial least square (PLS) is one method to reduce the number when some of the predictors are collinear or correlated. The new predictor variables $\hat{X}$ can be written as the linear combination of the original ones from X. The combination factors are found to maximize the covariance between the predictors and the response while $\hat{X}$ still possessing orthogonality and normalization properties. Therefore the algorithm provides a parsimonious model when the predictors are highly collinear. The details of the algorithm can be found in [81].

B3. Signal Decomposition

Signal $x(t) = A\sin(\omega_0 t + \phi)$ can be decomposed into two components:

$$C_1(t) = A\sin(\omega_0 t + \phi)\sin(\omega_0 t) = \frac{1}{2}A[\cos(\phi) - \cos(2\omega_0 t + \phi)], \quad \text{B.6}$$

$$C_2(t) = A\sin(\omega_0 t + \phi)\cos(\omega_0 t) = \frac{1}{2}A[\sin(\phi) + \sin(2\omega_0 t + \phi)]. \quad \text{B.7}$$

By filtering the high frequency components (2nd part on the right side) in equations B.6 and B.7, the phase term (1st part on the right side) can be recovered. This is how the beam phase can be determined as described in Chapter 5.

The amplitude A of the signal component can be readily obtained by taking square sum of the zero frequency components in equations B.6 and B.7.

B4. Fourier Transform

A signal in time domain $x(t)$ and in frequency domain $X(\omega)$ are connected by the transform:

$$X(\omega) = \int_{-\infty}^{\infty} x(t)e^{-j\omega t}dt, \qquad \text{B.8}$$

where j is the imaginary unit and ω the angular frequency. The signal $x(t)$ can be obtained by an inverse transform:

$$x(t) = \frac{1}{2\pi}\int_{-\infty}^{\infty} X(\omega)e^{j\omega t}d\omega, \qquad \text{B.9}$$

$X(\omega)$ is commonly referred to as the spectrum of signal $x(t)$. The equation B.9 is a synthesis equation of the signal $x(t)$. It should be pointed out that not every signal $x(t)$ can be analysed by the Fourier transform.

As an example, the Fourier transform of a Gaussian signal $\frac{1}{\sigma\sqrt{2\pi}}e^{-\frac{t^2}{2\sigma^2}}$ is still Gaussian $e^{-\frac{\omega^2\sigma^2}{2}}$. It can be easily seen that, for a short bunch, the spectrum is rich of various frequency components.

Let us assume that there is some time delay t_0 of the signal $x(t)$. Accordingly $X(\omega)$ is:

$$X(\omega) = e^{j\omega t_0}\int_{-\infty}^{\infty} x(t-t_0)e^{-j\omega t}dt. \qquad \text{B.10}$$

The Fourier transform of the time delayed signal $x(t-t_0)$ is $X(\omega)e^{-j\omega t_0}$. A time delay is equivalent to adding a linear phase to each component of the spectrum $X(\omega)$ while there is no influence on the amplitude of the signal.

A frequency shift $\Delta\omega$ in the spectrum $X(\omega)$ leads to:

$$x(t) = \frac{1}{2\pi} e^{-j\Delta\omega\, t} \int_{-\infty}^{\infty} X(\omega - \Delta\omega\,) e^{j\omega t} d\omega. \qquad \text{B.11}$$

The frequency shift modulates the time domain signal $x(t)$ by $e^{j\Delta\omega t}$ and has the influence on the amplitude of $x(t)$.

B5. The Characteristic Polynomial of a Matrix

For a $n \times n$ matrix A, a characteristic polynomial can be defined as:

$$P(\lambda) = \det(A - \lambda I) = b_0\lambda^n + b_1\lambda^{n-1} + b_2\lambda^{n-2} + \cdots + b_{n-1}\lambda + b_n, \qquad \text{B.12}$$

where I is the $n \times n$ identity matrix and b_i is the coefficient of the characteristic polynomial. The eigen values of the matrix A can be obtained from the roots of $P(\lambda) = 0$. The procedure works well when n is small and the solution becomes complicated when n increases.

For the problem in Chapter 3, the eigen values are already known. The problem is to estimate the unknown parameters or elements inside the matrix A (various coupling terms in Chapter 3). The relationship between the coefficients $b_i s$ and the matrix elements needs to be found. It has been proved that the coefficients can be identified based on the following recursive formula [82]:

$$b_0 = (-1)^n, \qquad b_1 = -b_0 T_1, \qquad b_2 = -\frac{1}{2}(b_1 T_1 + b_0 T_2),$$

$$b_n = -\frac{1}{n}(b_{n-1} T_1 + b_{n-2} T_2 + \cdots + b_1 T_{n-1} + b_0 T_n), \tag{B.13}$$

where T_i denotes the trace of matrix A^i (the power i of matrix A). The trace of a matrix is a relative simple property to compute compared with eigen values or eigen vectors. This enables us to estimate the parameters inside the matrix A.

B6. Error Propagation

Any measurements are subject to uncertainties or errors. When a quantity is based on the calculation of a set of measured data, the uncertainty of the measurements propagates to the calculated results.

Let us consider a calculated quantity $u = f(x, y)$, where x and y are the measured quantities with uncertainties σ_x and σ_y, and f is the mathematical rule of how u is calculated.

By expanding $f(x, y)$ around the mean value $\bar{x}, \bar{y}$, it can be shown that the uncertainty σ_u can be written as:

$$\sigma_u^2 \cong \left(\frac{\partial f}{\partial x}\right)^2 \sigma_x^2 + \left(\frac{\partial f}{\partial y}\right)^2 \sigma_y^2 + 2cov(x, y)\frac{\partial f}{\partial x}\frac{\partial f}{\partial y}, \tag{B.14}$$

where $cov(x, y)$ represents the covariance of x and y. The covariance term can influence the uncertain σ_u a lot depending on the specific measurement. Therefore, the measurements of quantities x and y should be designed as statistically independent as possible. The equation B.14 can then be simplified to:

$$\sigma_u^2 \cong \left(\frac{\partial f}{\partial x}\right)^2 \sigma_x^2 + \left(\frac{\partial f}{\partial y}\right)^2 \sigma_y^2. \quad \text{B.15}$$

The BPM resolution can be calculated based on three-BPM method. If there are three identical beam position monitors (BPMs 1, 2, 3 in one direction) and they are equally positioned. These BPMs are perfectly aligned and there is no coupling between x and y readings. The beam position at BPM 2 can be read out from the beam position monitor as x_2 and also be interpolated as $\hat{x}_2$ based on the BPM 1 and BPM 3 by assuming a straight trajectory:

$$\hat{x}_2 = \frac{1}{2}(x_1 + x_3). \quad \text{B.16}$$

$$\hat{x}_2 - x_2 = \frac{1}{2}(x_1 + x_3) - x_2. \quad \text{B.17}$$

Based on equations B.16 and B.17 , the uncertainty σ_{x_2} can be estimated based on the uncertainty $\sigma_{\hat{x}_2 - x_2}$:

$$\sigma_{x_2} = \sqrt{\frac{2}{3}}\sigma_{\hat{x}_2 - x_2}. \quad \text{B.18}$$

This can be interpreted as resolution of the BPM as used in Chapter 6.

Appendix C. Delta Wake and simple RLC Circuit

Due to the orthogonality of eigenmodes in a closed cavity, each mode can be treated individually and be simulated with a lumped resonant circuit. A parallel circuit is used to illustrate the connection between circuit parameters and the RF parameters for a cavity.

C1. Parallel RLC Circuit

A simple parallel RLC circuit consists of a resistor R, a capacitor C, and an inductor L as shown in Figure C.1.

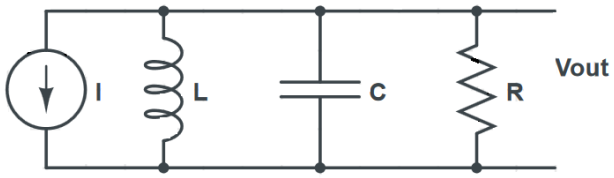

Figure C.1 A parallel RLC circuit.

The circuit forms a simple harmonic oscillator. The energy stored in such a circuit oscillates between the inductor and capacitor. The presence of the resistor consumes the energy, thus the oscillation will die away over time. The quality factor, as defined in Chapter 2, for the circuit is:

$$Q_0 = \frac{\frac{1}{2}V^2C}{\frac{1}{2}V^2T/R/2\pi} = CR\omega_0, \tag{C.1}$$

where V is the amplitude of voltage across the capacitor C, T is the oscillation period, and ω_0 is the resonant angular frequency.

The input (current I) and output (voltage V) in frequency domain are related by:

$$V_{out}(\omega) = \frac{R}{jR\left(\omega C - \frac{1}{\omega L}\right) + 1} I(\omega). \quad \text{C.2}$$

The resonant frequency is defined as the frequency at which the response takes the maximum value, so that $\omega_0 = \frac{1}{\sqrt{CL}}$. Two half power (3 dB) frequencies (ω_1,ω_2) can be found on the resonant curve, therefore two equations are set:

$$R\frac{\omega_2^2}{\omega_0^2} - \omega_2 L - R = 0\,, \quad \text{C.3}$$

$$R\frac{\omega_1^2}{\omega_0^2} + \omega_1 L - R = 0. \quad \text{C.4}$$

Based on equations C.3 and C.4, the relation between Q_0 and the bandwidth $\Delta\omega$ of the resonance curve:

$$\Delta\omega = \omega_2 - \omega_1 = \frac{\omega_0}{Q}\,, \quad \text{C.5}$$

where $\omega_2 > \omega_1$ is assumed.

The impedance of such a circuit can be defined as the voltage and current ratio:

$$Z(\omega) = \frac{R}{jR\left(\omega C - \frac{1}{\omega L}\right) + 1}. \quad \text{C.6}$$

For complex RF structures, it is not trivial to determine the capacitance and inductance directly from the geometry. Therefore, it is useful to express $Z(\omega)$ in terms of Q_0 and ω_0, which are readily available from measurements or simulations.

$$Z(\omega) = \frac{R}{jQ_0\left(\frac{\omega}{\omega_0} - \frac{\omega_0}{\omega}\right) + 1}. \tag{C.7}$$

As we can perceive from equation C.7, the impedance shows different electrical properties:

1. $\omega > \omega_0$, the impedance is capacitive.
2. $\omega < \omega_0$, the impedance is inductive.
3. $\omega = \omega_0$, the impedance is purely resistive.

The real part of the impedance shows how the energy decays over time:

$$Re\{Z(\omega)\} = \frac{-R}{1 + Q_0^2\left(\frac{\omega_0}{\omega} - \frac{\omega}{\omega_0}\right)^2} \cong \frac{-R}{1 + 4\left(\frac{\omega - \omega_0}{\Delta\omega}\right)^2}. \tag{C.8}$$

Equation C.8 justifies the Lorentz fitting equation used in Chapter 4.

C2. Circuit natural response when t < 0, t = 0, t > 0

If $t = 0$ is defined as the time when beam enters a RF cavity, the response of the simple RLC circuit can be used to simulate the wake potential for a single mode. Here three regimes are discussed namely $t < 0, t = 0, t > 0$:

- $t < 0$: the voltage across the capacitor and the current through the inductor in Figure C.1 are zero. This means that there is no wakefield ahead of the bunch according to causality for ultra-relativistic bunch.

- $t = 0$: the circuit in Figure C.1 is fed with a driving current $I(t) = q_0\delta(t)$. The voltage across capacitor ramps up to $\frac{q_0}{C}$ instantly. At the same time, the current that goes through the inductor is zero. These two initial conditions serve as the starting point of the RLC circuit when $t > 0$. From the energy conservation point of view, the energy stored in the capacitor is $\frac{1}{2}CU^2$ or $\frac{1}{2}\frac{q_0^2}{C}$ and the energy loss when beam transverses an empty cavity is q_0U_1. Therefore the voltage is $U_1(t = 0) = \frac{1}{2}\frac{q_0}{C}$.
- $t > 0$: the circuit response is first solved in *s* domain, and then the time domain solution is obtained through inverse Laplace transformation.

The components of R, L, C can be modelled as R, sL and $1/sC$ in *s* domain. Therefore the response of the circuit can be written as:

$$\mathcal{L}(V_{out}) = \frac{\frac{q_0}{C}s}{s^2 + \Delta\omega s + \omega_0^2}, \tag{C.9}$$

where $\mathcal{L}$ represents the Laplace operator and $\Delta\omega$ is defined in equation C.5.

The output voltage in *s* domain can be expanded as:

$$\mathcal{L}(V_{out}) = \frac{A_1}{s - (-a + jb)} + \frac{A_1^*}{s - (-a - jb)}, \tag{C.10}$$

where $a = \frac{\Delta\omega}{2}, b^2 = \omega_0^2 - \frac{\Delta\omega^2}{4}$, A_1 is a complex number containing the information of initial conditions and A_1^* the complex conjugate of A_1.

By inverse transformation, the voltage is:

$$V_{out}(t) = e^{-at}\left(A_1 e^{jbt} + A_1^* e^{-jbt}\right), t \geq 0^+. \quad \text{C.11}$$

The constants A_1 and A_1^* can be determined based on the initial conditions. When the quality factor is high enough, which is the general case for SRF cavities, the time response is:

$$V_{out}(t) = \frac{q_0}{C}\ \frac{\omega_0}{\omega_d} e^{-\frac{\Delta\omega}{2}t} \cos\left(\omega_d t + \arctan(\frac{\Delta\omega}{2\omega_d})\right), \quad \text{C.12}$$

where $\omega_d = \frac{\sqrt{|\Delta\omega^2 - 4\omega_0^2|}}{2}$. When $Q \gg 1$, $\omega_d \cong \omega_0$.

Based on $\omega_0 = \frac{1}{\sqrt{CL}}$, $Q_0 = CR\omega_0$, in the context of wakefield, a loss factor can be defined as:

$$k_{loss} = \frac{Energy\ loss\ of\ point\ charge}{point\ charge^2} = \frac{1}{2C} = \frac{\omega_0 R}{2Q_0}. \quad \text{C.13}$$

Equation C.12 is useful when expressed in quantities which can be obtained through measurements or simulation:

$$V_{out}(t) = 2k_{loss}q_0\ \frac{\omega_0}{\omega_d} e^{-\frac{\Delta\omega}{2}t} \cos\left(\omega_d t + \arctan\left(\frac{\Delta\omega}{2\omega_d}\right)\right). \quad \text{C.14}$$

In a superconducting cavity, Q_0 is normally in the order of $10^9 \sim 10^{10}$, therefore equation C.14 can be further simplified as:

$$V_{out}(t) = 2k_{loss}q_0\, e^{-\frac{\Delta\omega}{2}t}\cos(\omega_d t). \qquad \text{C.15}$$

Interestingly, V_{out} can also be obtained directly by inverse Laplace transformation of C.9:

$$V_{out}(t) = \frac{1}{2\pi j}\int_{\gamma-j\infty}^{\gamma+j\infty} V(s)e^{st}\,ds\,, \qquad \text{C.16}$$

where γ lies on the right side of any poles from $V(s)e^{st}$. The integral in equation C.16 can be evaluated by constructing contours C1 and C2 as shown in Figure C.2.

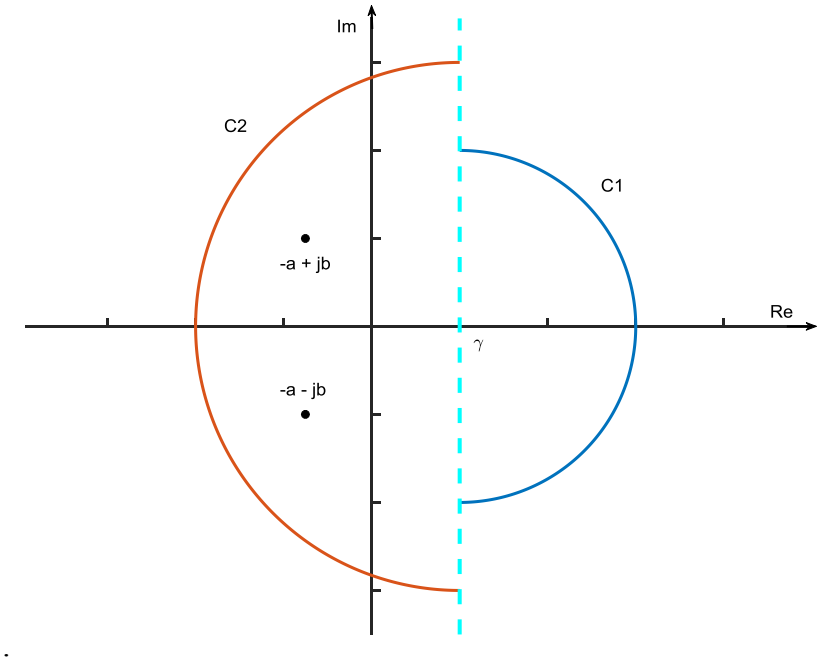

Figure C.2 The integral contours C1 and C2 used for equations C.17 and C.19.

If $t < 0$, one can take the contour C1 so that according to Cauchy's theorem, the integral is zero:

$$V_{out}(t) = \frac{1}{2\pi j} \lim_{(R\to+\infty)} \left(\oint_{C1} V(s)e^{st}ds - \int_{\frac{\pi}{2}}^{-\frac{\pi}{2}} V(s)e^{st}\, d\theta \right) = 0 - 0 = 0. \quad \text{C.17}$$

If t = 0, equation C.16 becomes:

$$V_{out}(0) = \frac{1}{2\pi j} \int_{\gamma-j\infty}^{\gamma+j\infty} V(s)\, ds. \quad \text{C.18}$$

The integral is evaluated along the contour C2 and according to Residue theorem one can obtain:

$$V_{out}(0) = \frac{1}{2\pi j} \lim_{(R\to+\infty)} \left(\oint_{C2} V(s)\, ds - \int_{\frac{\pi}{2}}^{\frac{3\pi}{2}} V(s)\, d\theta \right) \quad \text{C.19}$$

$$= (A_1 + A_1^*) - \frac{1}{2}(A_1 + A_1^*) = \frac{1}{2}(A_1 + A_1^*) = \frac{1}{2}\frac{q_0}{C}.$$

In summary, the voltage response V_{out} is:

$$V_{out}(t) = \begin{cases} 0, & t < 0, \\ k_{loss}q_0, & t = 0, \\ 2k_{loss}q_0\, e^{-\frac{\Delta\omega}{2}t}\cos(\omega_d t), & t > 0. \end{cases} \quad \text{C.20}$$

C3. Capacitance and R/Q

The quantity R/Q as defined in Chapter 2 can be written as:

$$\frac{R}{Q} = \frac{1}{C\omega_0} = \sqrt{\frac{L}{C}}. \qquad \text{C.21}$$

R/Q is a useful quantity to describe the beam cavity interaction and does not depend on the cavity size and material. Therefore there is no dependence on the resistance R in the expression. Based on the definition of loss factor (equation C.13), the relation between R/Q and loss factor k_{loss} can be obtained:

$$\frac{R}{Q} = \frac{1}{C\omega_0} = \frac{2k_{loss}}{\omega_0}. \qquad \text{C.22}$$

Several RLC circuits can be coupled together to represent a band of modes as shown in Chapter 3 and Appendix D. This technique is exploited in Chapter 3 and also demonstrated in Appendix D.

Appendix D. Double Chain Circuit Model

D1. Double Chain Circuit Model

The first two dipole bands for the TESLA cavity are TE111 and TM110 like bands [35]. The modes in these bands are hybrid in their nature. Compare to the circuit model for monopole band in Chapter 3, two chains of circuits are required to represent the TE and TM bands. The model is schematically shown in Figure D.1 [83]. Mutual inductances $\boldsymbol{M}$ and $\widehat{\boldsymbol{M}}$ are introduced in order to account for the coupling within each band. The cross coupling term $\overline{M}$ represents the coupling between TE and TM band. Beam current is coupled to the TM band by adding a parallel current source to the capacitors in TM band.

The model was reported in [45] and I tailored it to represent the first two dipole bands for a cavity with nine identical cells. The dispersion relation is obtained from an infinite circuit model. The infinite chain is then truncated to represent a nine cell cavity.

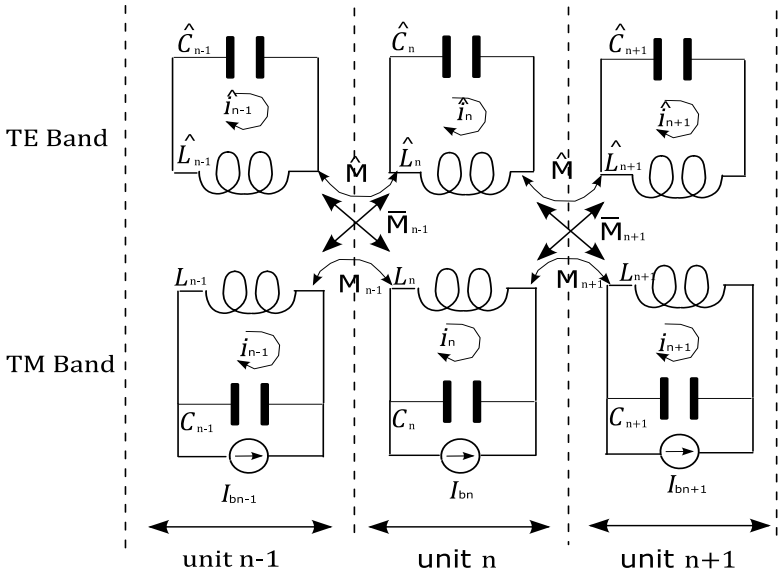

Figure D.1 A two chain coupled LC circuit model. The quantities with circumflex are reserved for the TE band, e.g. $\hat{L}$ is the inductance for the TE band circuit. M and $\widehat{M}$ indicate the mutual inductance in the TM and TE band circuit model respectively. A third coupling term $\overline{M}$ is introduced in the model to account for the coupling between the TE and TM bands. The beam current I_{bn} is used to represent the beam current or the excitation for the circuit model. Note that the notation is slightly different compared with [83].

The dynamics of the system is governed by the equations for the TE and TM band respectively as shown in [83]:

$$\frac{1}{\hat{C}_n}\int \hat{\imath}_n dt + \hat{L}_n\frac{d\hat{\imath}_n}{dt} + \frac{\widehat{M}_{n+1}}{2}\frac{d\hat{\imath}_{n+1}}{dt} + \frac{\widehat{M}_{n-1}}{2}\frac{d\hat{\imath}_{n-1}}{dt} - \frac{\bar{M}_{n-1}}{2}\frac{di_{n+1}}{dt} + \frac{\bar{M}_{n-1}}{2}\frac{di_{n-1}}{dt} = 0, \quad \text{D.1}$$

$$\frac{1}{C_n}\int (i_n - I_{bn})dt + L_n\frac{di_n}{dt} - \frac{M_{n+1}}{2}\frac{di_{n+1}}{dt} - \frac{M_{n-1}}{2}\frac{di_{n-1}}{dt} + \frac{\bar{M}_{n+1}}{2}\frac{d\hat{\imath}_{n+1}}{dt} - \frac{\bar{M}_{n-1}}{2}\frac{d\hat{\imath}_{n-1}}{dt} = 0, \quad \text{D.2}$$

where I_{bn} represents the beam current in cell n. For convenience, the equation is normalized by the current terms: $a_n = i_n\omega_n\sqrt{L_n}$ and $\hat{a}_n = \hat{\imath}_n\hat{\omega}_n\sqrt{\hat{L}_n}$. Then equations D.1 and D.2 become:

$$\hat{\omega}_r^2\iint \hat{a}_n\,dt + \hat{a}_n + \frac{1}{2}\hat{\eta}(\hat{a}_{n+1} + \hat{a}_{n-1}) - \frac{1}{2}\bar{\eta}\frac{\hat{\omega}_r}{\omega_r}(a_{n+1} - a_{n-1}) = 0\,, \quad \text{D.3}$$

$$\omega_r^2\iint a_n\,dt + a_n - \frac{1}{2}\eta(a_{n+1} + a_{n-1}) + \frac{1}{2}\bar{\eta}\frac{\omega_r}{\hat{\omega}_r}(\hat{a}_{n+1} - \hat{a}_{n-1}) = \omega_r^2\iint a_b\,dt\,. \quad \text{D.4}$$

The coupling terms are defined as, $\eta_{n\pm\frac{1}{2}} = \frac{M_{n\pm1}}{\sqrt{L_n L_{n\pm1}}}$, $\hat{\eta}_{n\pm\frac{1}{2}} = \frac{\hat{M}_{n\pm1}}{\sqrt{\hat{L}_n \hat{L}_{n\pm1}}}$ and $\bar{\eta}_{n\pm\frac{1}{2}} = \frac{\bar{M}_{n\pm1}}{\sqrt{L_n \hat{L}_{n\pm1}}}$,where $\hat{\omega}_r$ and ω_r are the resonant frequencies for the TE111 and TM110 modes in a single cell respectively. $\hat{\eta}$ and η are the coupling terms for the TE and TM bands, and $\bar{\eta}$ is responsible for the TE to TM band coupling. I assumed: $\hat{\eta}_{n+\frac{1}{2}} = \hat{\eta}_{n-\frac{1}{2}} = \hat{\eta}$, $\eta_{n+\frac{1}{2}} = \eta_{n-\frac{1}{2}} = \eta$ and $\bar{\eta}_{n+\frac{1}{2}} = \bar{\eta}_{n-\frac{1}{2}} = \bar{\eta}$. The $n \pm \frac{1}{2}$ indices indicate the coupling from the right and left side in the same cell n. a_b is beam excitation source. Since the cavity under consideration has nine cells, there are 18 coupled recursive equations in total.

D2. Infinite Periodic coupled Circuit

It is straight forward to translate equations D.3 and D.4 into frequency domain (beam current is set to zero):

$$\left(1 - \frac{\hat{\omega}_r^2}{\omega^2}\right)\hat{A}_n + \frac{1}{2}\hat{\eta}\left(\hat{A}_{n+1} + \hat{A}_{n-1}\right) - \frac{1}{2}\bar{\eta}\frac{\hat{\omega}_r}{\omega_r}\left(A_{n+1} - A_{n-1}\right) = 0\,, \tag{D.5}$$

$$\left(1 - \frac{\omega_r^2}{\omega^2}\right)A_n - \frac{1}{2}\eta\left(A_{n+1} + A_{n-1}\right) + \frac{1}{2}\bar{\eta}\frac{\omega_r}{\hat{\omega}_r}\left(\hat{A}_{n+1} - \hat{A}_{n-1}\right) = 0\,. \tag{D.6}$$

By assuming the Floquet periodic boundary condition ($A_{n+1} = A_n e^{j\phi}$ and $\hat{A}_{n+1} = \hat{A}_n e^{j\phi}$) in equations D.5 and D.6, the dispersion relation can be derived:

$$\left(\frac{1 + \hat{\eta}\cos\phi}{\hat{\omega}_r^2} - \frac{1}{\omega^2}\right)\left(\frac{1 - \eta\cos\phi}{\omega_r^2} - \frac{1}{\omega^2}\right) - \frac{\bar{\eta}^2}{\hat{\omega}_r^2\omega_r^2}\sin^2\phi = 0. \tag{D.7}$$

The parameters in equation D.7 can be obtained based on a single cell simulation. Here the coupling terms $\hat{\eta}$, η and $\bar{\eta}$ are restricted to be positive. The parameters can be determined based on the frequency values with phase advance of 0 and π:

$$\omega_r = \sqrt{\frac{2\omega_\pi^2\omega_0^2}{\omega_\pi^2+\omega_0^2}} \text{ and } \eta = \frac{\omega_0^2 - \omega_\pi^2}{\omega_\pi^2+\omega_0^2}, \quad \text{D.8}$$

$$\hat{\omega}_r = \sqrt{\frac{2\hat{\omega}_\pi^2\hat{\omega}_0^2}{\hat{\omega}_\pi^2+\hat{\omega}_0^2}} \text{ and } \hat{\eta} = \frac{\hat{\omega}_\pi^2-\hat{\omega}_0^2}{\hat{\omega}_\pi^2+\hat{\omega}_0^2}. \quad \text{D.9}$$

Under the assumption of thin irises [45], the band to band coupling term $\bar{\eta}$ can be estimated by the relation:

$$\bar{\eta} = \sqrt{\eta\hat{\eta}}. \quad \text{D.10}$$

The coupling parameters estimation based on equations D.8 and D.9 is called method 1. The parameters in the dispersion curve can be obtained by fitting to the data from single cell simulation and it is named as method 2. Both methods are shown in Figure D.2.

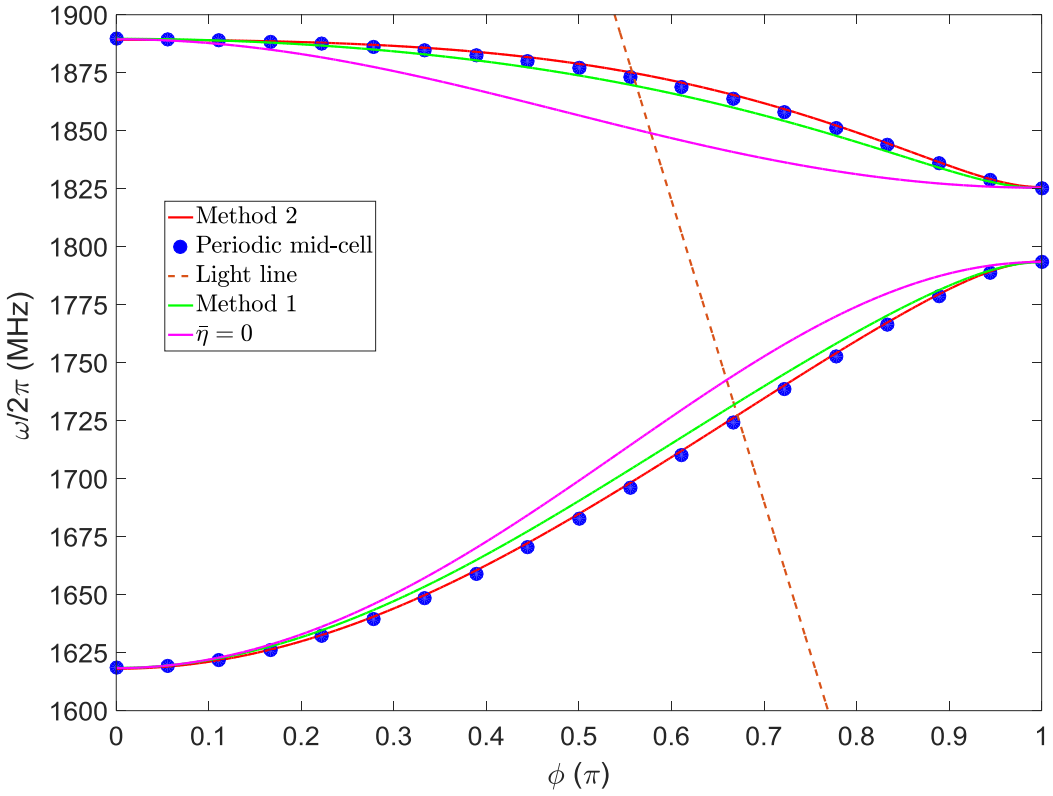

Figure D.2 Dispersion relation of a single cell subject to periodic boundary condition obtained from CST (blue); Analytic dispersion curve based on 0 and π modes (method 1) and based on fitting (method 2); Dispersion curve when $\bar{\eta} = 0$ (magenta).

It is the band to band coupling term $\bar{\eta}$ that accounts for the behaviour of the coupled TE111 and TM110 bands. Based on method 1 and method 2, the parameters obtained are summarized in Table D.1:

Table D.1 Coupling terms obtained based on method 1 and method 2

	Method 1	Method 2
η	3.46%	3.44%
$\hat{\eta}$	10.23%	10.24%
$\bar{\eta}$	5.95%	6.37%

In Table D.1, η and $\hat{\eta}$ are almost identical for methods 1 and 2 respectively, but method 2 gives a higher band to band coupling. This result agrees with the fact that the irises are not thin for TESLA cavity so that equation D.10 is violated. The following analysis is based on method 2.

The set of equations D.5 and D.6 can be written as in a matrix form:

$$\underbrace{\begin{bmatrix} \frac{1+\hat{\eta}\cos\phi}{\hat{\omega}_r^2} & \frac{j\bar{\eta}}{\omega_m\hat{\omega}_m}\sin\phi \\ -\frac{j\bar{\eta}}{\omega_m\hat{\omega}_m}\sin\phi & \frac{1-\eta\cos\phi}{\omega^2} \end{bmatrix}}_{H} \begin{bmatrix} A \\ \hat{A} \end{bmatrix} = \frac{1}{\omega^2}\begin{bmatrix} A \\ \hat{A} \end{bmatrix}. \quad \text{D.11}$$

The frequencies of the eigenmodes in TE and TM band can be found from the eigenvalues of H.

D3. Truncated Circuit Model

To approximate a nine cell cavity, the infinite model is truncated and boundary conditions need to be specified as described in Chapter 3. There are two possible sets of boundary conditions ever proposed [45], [83]. One set corresponds to N-cell structure:

$$A_0 = A_1, A_{N+1} = A_N, \hat{A}_0 = -\hat{A}_1, \hat{A}_{N+1} = -\hat{A}_N. \quad \text{D.12}$$

The other set of boundary condition corresponds to N-2 full cells terminated by two half cells:

$$A_0 = A_2, A_{N+1} = A_{N-1}, \hat{A}_0 = 0, \hat{A}_{N+1} = 0. \quad \text{D.13}$$

By using equation D.12 as boundary conditions, on average the mean difference between mode frequencies from the circuit model and from the CST simulation of a cavity is 6 MHz. The boundary condition D.13 suggests approximately 10 MHz difference. To further reduce the error, a third type of boundary condition is proposed by terminating the structure similar as the single chain circuit as in Chapter 3. The first equation ($n = 1$) for the TE and TM bands can be written as:

$$\hat{\kappa}_1\hat{A}_1 + \hat{\kappa}_2\hat{A}_2 + \kappa_3 A_2 + \kappa_4 A_1 = 0\,, \tag{D.14}$$

$$\kappa_1 A_1 + \kappa_2 A_2 + \kappa_3\hat{A}_2 + \kappa_4\hat{A}_1 = 0\ . \tag{D.15}$$

There are six unknown parameters in equations D.14 and D.15. A program was written in MATLAB® in order to tune the parameters with the goal to minimize RMS between the circuit model results and the CST simulation.

To make the parameter space scan converge faster, I used again the relation in Appendix B (section B5) to reduce the dimension of the parameter space. The work flow of the tuning program is shown in Figure D.3.

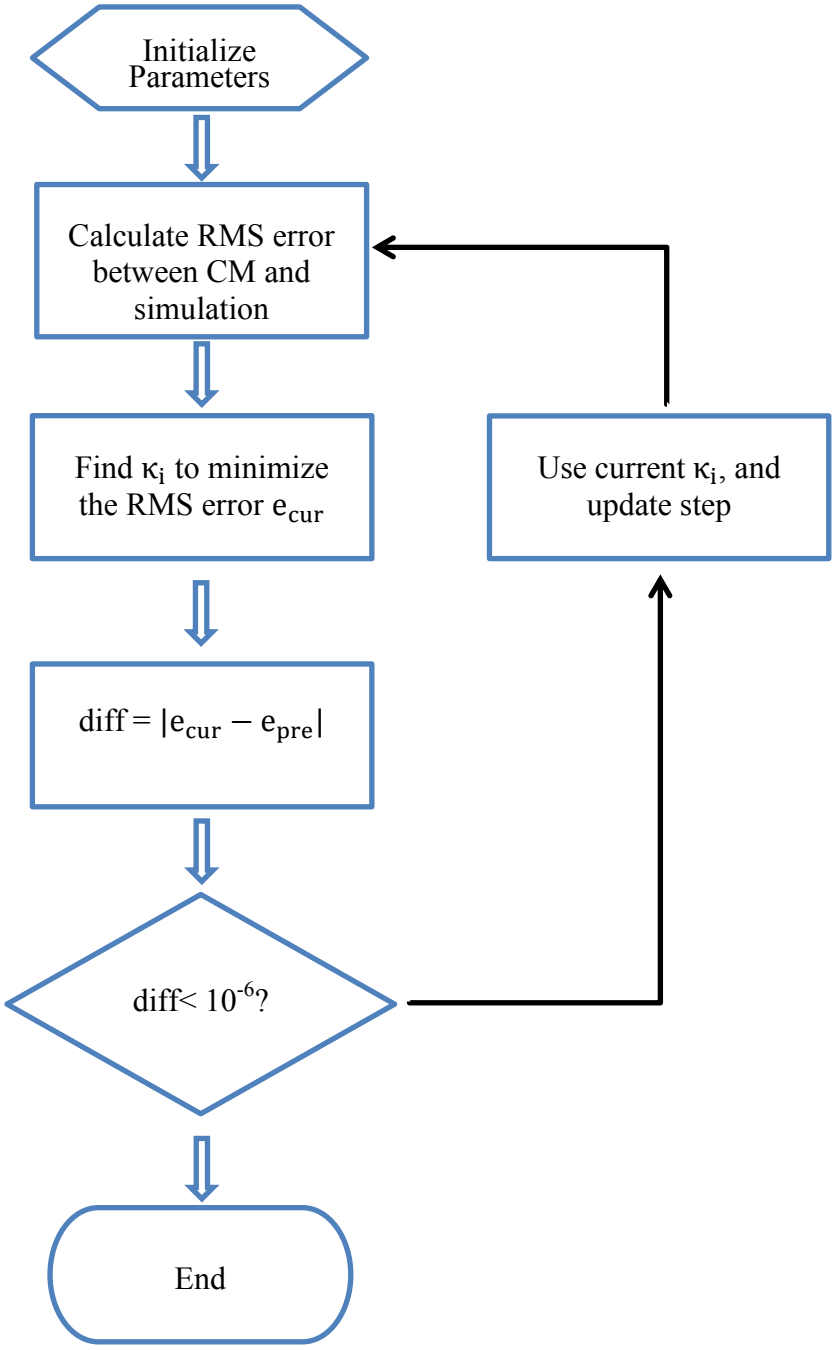

Figure D.3 Flow chart of tuning procedure to find the unknown parameters in the circuit model (equations D.14 and D.15)

The relative tolerance is chosen to be 10^{-6}, which corresponds to 1 Hz. After tens of iteration, the program is able to converge to the parameters that minimize the RMS error. After tuning, the error is below 1 MHz compared to 10 MHz before the tuning.

As shown in Figure D.4, the average absolute error is below 1 MHz.

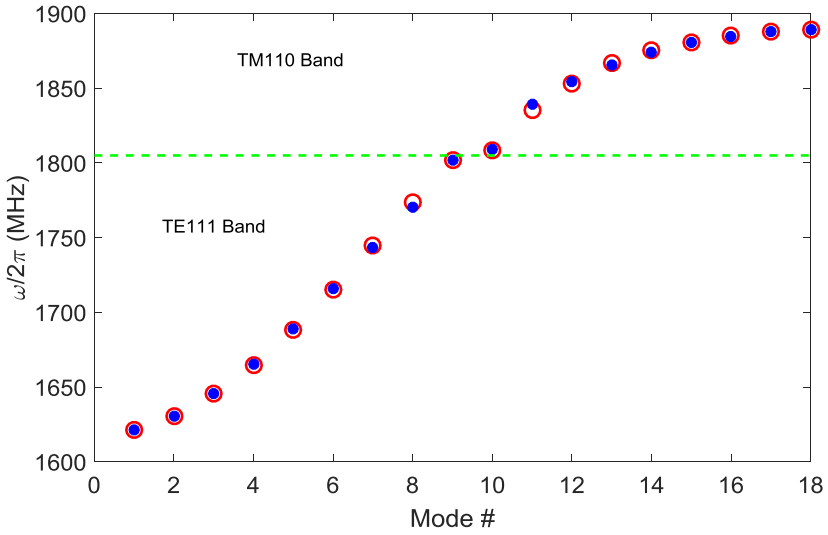

Figure D.4 Mode frequencies of a tuned circuit (Blue dots) and a nine cell structure with beam pipes from CST simulation. The average error is below 1 MHz.

Appendix E. Scattering Matrix for Network Analysis

Due to the difficulty in dealing with impedances in microwave frequencies, a more convenient way to characterize the system is to analyze the reflected and transmitted waves with the scattering matrix [40]. In order to illustrate the definition of the scattering matrix, an arbitrary N-port microwave network is shown in Figure E.1.

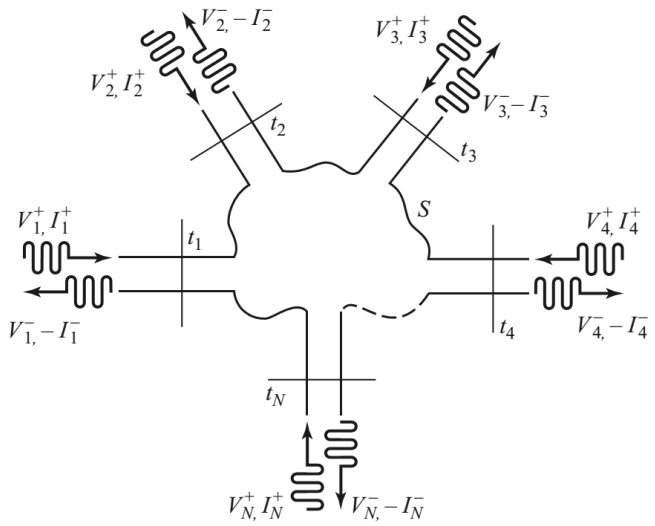

Figure E.1 An arbitrary N-port microwave network (from [40], p.174).

The reflected voltage amplitude V_n^- at port n is related to the incident voltage wave V_n^+ on the same port by:

$$\begin{bmatrix} V_1^- \\ V_2^- \\ \vdots \\ V_N^- \end{bmatrix} = \begin{bmatrix} S_{11} & S_{12} & \cdots & S_{1N} \\ S_{21} & S_{22} & \cdots & S_{2N} \\ \vdots & \vdots & \vdots & \vdots \\ S_{N1} & S_{N1} & \cdots & S_{NN} \end{bmatrix} \begin{bmatrix} V_1^+ \\ V_2^+ \\ \vdots \\ V_N^+ \end{bmatrix}. \qquad \text{E.1}$$

The element S_{ij} in the S matrix can be determined as:

$$S_{ij} = \frac{V_i^-}{V_j^+}\bigg|_{V_k^+=0\ for\ k\neq j} . \qquad \text{E.2}$$

Taking the transmission measurements in Chapter 4 as an example, the cavity can be treated as a two port system with the couplers HOM1 and 2 as port 1 and 2. The parameter S_{21} is the ratio between voltage wave V_2^- coming out of the port 2 and voltage wave V_1^+ coming into the port 1. This meaning justifies the name transmission parameter S_{21}. Conveniently, the S matrix of a system e.g. a RF cavity, can be measured with a vector network analyser.

Appendix F. Technical Setup of Beam Phase and Position Measurements and associated Electronics

The beam phase measurement setup at FLASH is shown in Figure F.1. It consists of a fast scope, a set of splitters and filters. The setup is essentially the same as the experimental setup at the E-XFEL in section 5.3.1 of Chapter 5.

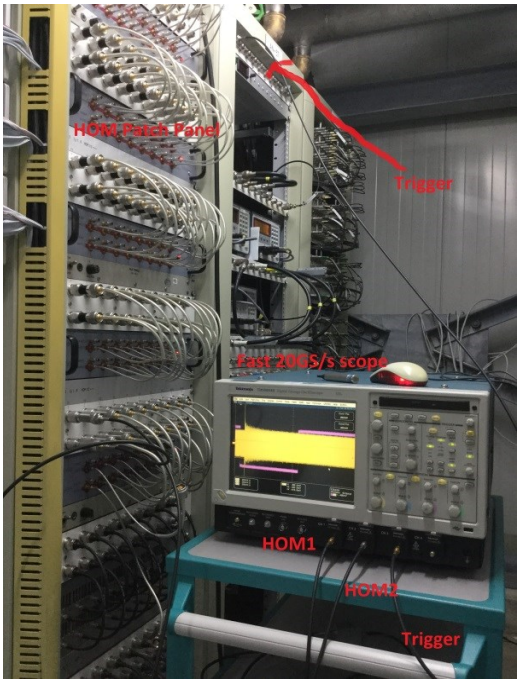

Figure F.1 Photo of the broadband setup for beam phase measurement at FLASH.

F1. Electronics of HOMBPM for 3.9 GHz Cavities

This section shows the block diagram and real pictures for the electronics used by HOMBPM for 3.9 GHz cavities.

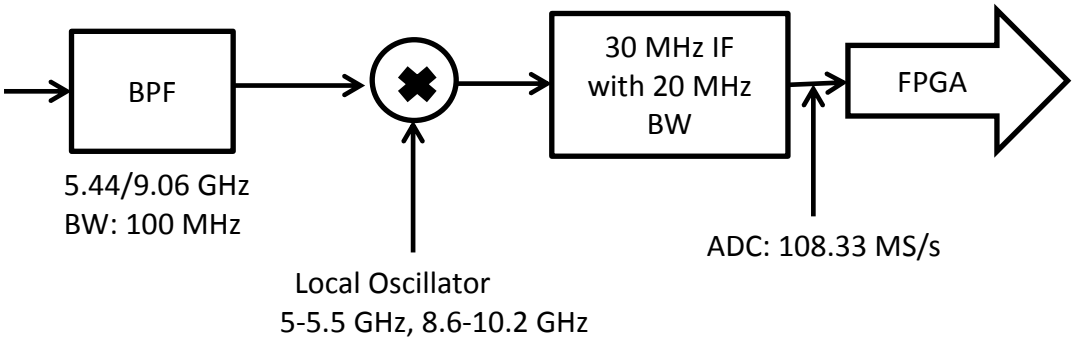

Figure F.2 A block diagram of the HOM electronics for 3.9 GHz cavities at the E-XFEL [55].

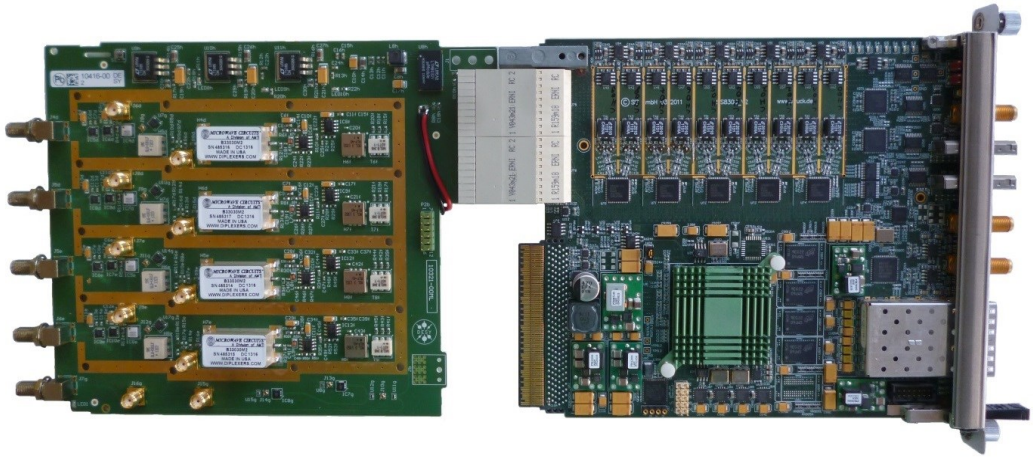

Figure F.3 Photo of downconverter RTM (Rear Transition Module) with Struck SIS8300 AMC. (Courtesy of Thomas Wamsat)

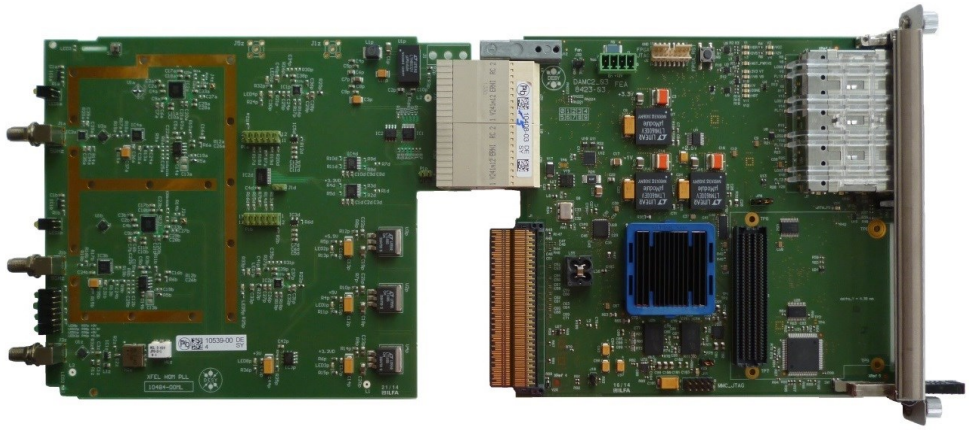

Figure F.4 Photo of the PLL (Phase Locked Loop) RTM with DAMC2. (Courtesy of Thomas Wamsat)

F2. HOMBPM and HOMBPhM for 1.3 GHz Cavities

This section shows the block diagram and a real picture for the electronics used by HOMBPM and HOMBPhM for 1.3 GHz cavities.

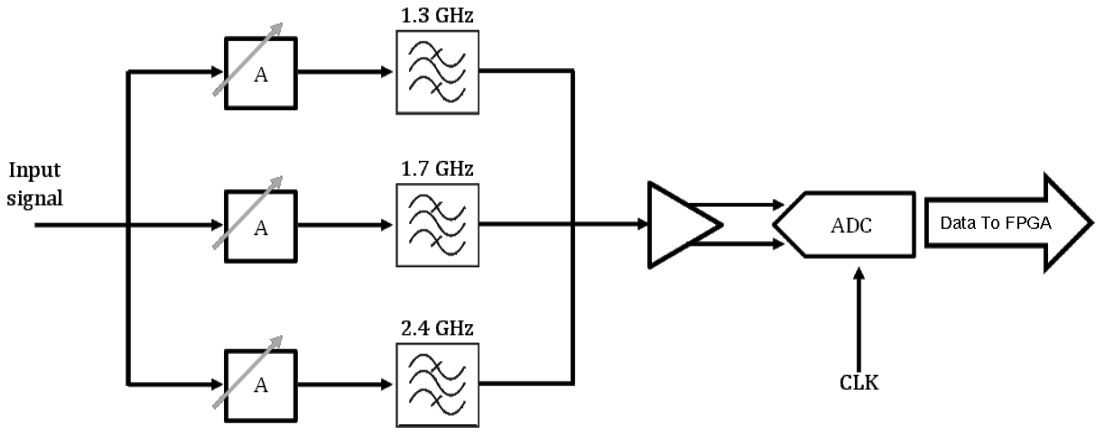

Figure F.5 A block diagram of the HOM electronics for 1.3 GHz cavities at the European XFEL. The HOMBPM and HOMBPhM are integrated in the same electronics.

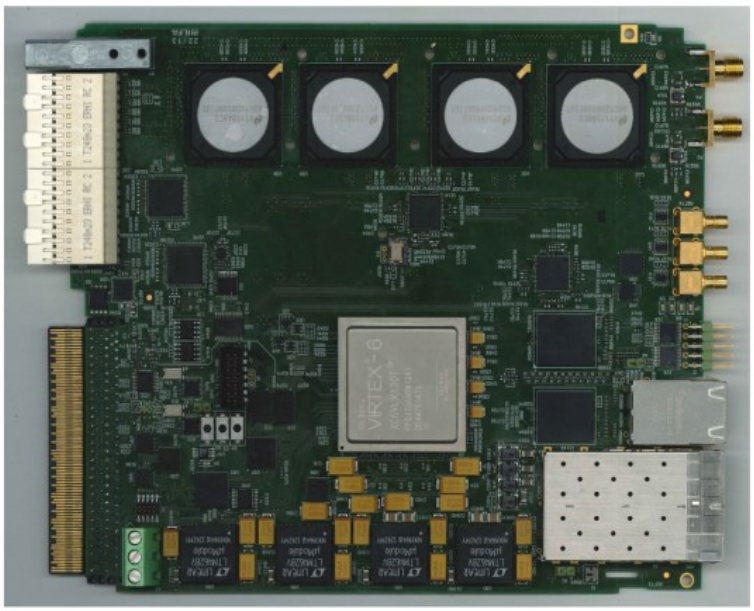

Figure F.6 Photo of DAMC-DS800 MTCA.4 Fast Digitizer. The future electronics will be slightly different from this picture. (Courtesy of Samer Bou Habib)

Appendix G. Simulation Data

The following two tables show the data used in Chapter 3 for the circuit model development. The data is reproduced from the report [35].

Table G.1 Eigenmode frequencies used for circuit model of first monopole band in Chapter 3. The data is cited in page 30 of report [35].

Mode index	$\omega/2\pi$ (GHz)	R/Q (Ω)	Phase advance: ϕ (°)
TM010-1	1.2756	0.0002	20.0
TM010-2	1.2776	0.0001	39.9
TM010-3	1.2807	0.0013	59.9
TM010-4	1.2845	0.0005	79.8
TM010-5	1.2885	0.0005	99.8
TM010-6	1.2924	0.0019	119.7
TM010-7	1.2955	0.0339	139.6
TM010-8	1.2976	0.0163	159.2
TM010-9	1.2983	511.0652	176.1

Table G.2 Eigenmode frequencies used for circuit model of beam phase monitor in Chapter 3. The data is cited in page 30 of report [35].

Mode index	$\omega/2\pi$ (GHz)	R/Q (Ω)	Phase advance: ϕ (°)
TM011-1	2.3800	0.0010	159.9
TM011-2	2.3856	0.0196	139.9
TM011-3	2.3943	0.0329	119.9
TM011-4	2.4055	0.0547	100.1
TM011-5	2.4181	0.4943	80.6
TM011-6	2.4308	0.0075	61.4
TM011-7	2.4419	10.2352	43.0
TM011-8	2.4499	77.6533	25.9
TM011-9	2.4539	73.8717	11.5